Title
Interactions of Trivalent Lanthanides and Actinides with Solid-Phase Extractants

Author
Shusterman, Jennifer Anne

Publication Date
2015

Peer reviewed|Thesis/dissertation

Interactions of Trivalent Lanthanides and Actinides with Solid-Phase Extractants

by

Jennifer Anne Shusterman

A dissertation submitted in partial satisfaction of the
requirements for the degree of
Doctor of Philosophy

in

Chemistry

in the

Graduate Division
of the
University of California, Berkeley

Committee in charge:
Professor John Arnold, Chair
Professor Darleane Hoffman
Professor Joonhong Ahn

Summer 2015

Interactions of Trivalent Lanthanides and Actinides with Solid-Phase Extractants

Abstract

Interactions of Trivalent Lanthanides and Actinides with Solid-Phase Extractants

by

Jennifer Anne Shusterman

Doctor of Philosophy in Chemistry

University of California, Berkeley

Professor John Arnold, Chair

The ability to successfully sequester and separate trivalent lanthanides and actinides has applications to the nuclear fuel cycle, processing of irradiated target materials, and nuclear forensics. The challenge in separating the trivalent lanthanides and actinides is their similar size and charge. As a result of this, standard size exclusion or ion exchange techniques become much more challenging. Instead of focusing on size or charge for separation, their differences in interactions with complexing ligands can be utilized. Another challenge in trivalent lanthanide and actinide separations is that these metals are often dissolved in highly acidic matrices. Thus, the stability of the extractant ligand used to complex the metal is at risk of degradation.

The most common sequestration and separation routes based on complex formation for lanthanides and actinides use liquid-liquid separations, which can generate large volumes of hazardous organic waste. By moving to solid-liquid separations, in which the organic phase is replaced by a solid-phase extractant (SPE), the production of large volumes of waste can be minimized. The most common method of making SPEs for lanthanide and actinide separations is coating an organic extractant ligand on either a silica or polymer support. As a result of only coating the ligand rather than bonding it to the solid support, these materials can suffer from ligand degradation and detachment. Chapter 5 focuses on trivalent lanthanide and actinide interactions with a commercially available SPE. While those materials were found to have use for certain applications, their limitations motivated the organically-modified mesoporous silica (OMMS) development presented in Chapter 7.

The work presented here is a study on solid-phase extractants for lanthanide and actinide separations, particularly focused on OMMS. The OMMS materials are made by covalently binding the extractant ligand to the mesoporous silica, to increase the stability of these SPEs in the presence of acidic media. Chapters 6 and 7 discuss the synthesis and characterization of two types of OMMS materials as well as macroscopic and molecular level studies of these materials with trivalent lanthanides and actinides. Additionally, the stability of the OMMS materials in the presence of acid was probed using nuclear magnetic resonance (NMR) spectroscopy.

The first OMMS material discussed is a caprolactam (CA)-modified mesoporous silica. The behavior of Eu(III), Sc(III), and Al(III) was studied with the CA-modified mesoporous silica. Al and Sc were studied as comparative trivalent metals that had smaller ionic radii than Eu. The results of batch sorption experiments and mainly solid-state NMR spectroscopy studies are presented. The acid stability studies showed that the CA-modified mesoporous silica degraded in

two ways in the presence of acid: 1) the 7-membered ring of the ligand opened, and 2) a portion of the isolated ligands on the surface were cleaved at the silane anchor. It was determined that while the CA materials were not effective sorbents for Eu(III) from acidic matrices, they did bind Al(III) and Sc(III). Through the NMR studies, both Al and Sc were found to complex to the CA ligand and the surface silanols simultaneously. This work was the first time solid-state NMR had been used to study the surface, ligand, and metals directly of OMMS materials via their NMR active nuclei (^{29}Si, ^{13}C, ^{1}H, ^{27}Al, and ^{45}Sc).

The second OMMS material studied was a diglycolamide (DGA)-modified mesoporous silica. The main focus of this work was the interactions of the DGA-modified mesoporous silica with Eu(III) and Am(III), but also touched on other trivalent species such as La(III), Lu(III), and Y(III). Again, the stability of this material in the presence of acid was investigated using NMR spectroscopy and while the DGA ligand was found to withstand acid treatment, the isolated ligand cleavage at the silane anchor still occurred. The DGA-modified mesoporous silica was found to efficiently bind the trivalent species at high acid concentrations, particularly below pH 1. As a result of the mesoporous substrate and subsequently high ligand loading for the associated mass, the sorption capacity for Eu(III) (379 μmol g^{-1}) was found to be higher than other diglycolamide SPEs. Through infrared spectroscopy and NMR spectroscopy experiments, the trivalent metals were found to bind to the carbonyl and ether oxygens of the DGA ligand. Fluorescence spectroscopy of Eu(III) and X-ray absorption spectroscopy studies elucidated that the trivalent metals are complexing as three ligands per metal center. Proof-of-concept column experiments demonstrate the use of DGA-modified mesoporous silica as a stationary phase to which Eu was both sorbed and then eluted.

A major focus of this work was the interplay of macroscopic and molecular level studies to best characterize metal interactions with OMMS materials. While both the bulk and molecular level investigations can provide information about these systems, neither gives the full picture in itself. In designing materials for separations, knowledge of the complete picture is necessary in order to best optimize methodologies and predict separation behavior.

For my Mom and Dad for their endless love, support, and laughter!

Contents

List of Figures

List of Tables

Acknowledgments

The work presented here and getting to this point in graduate school would not have been possible without the help of many people.

First and foremost, I want to thank my family. Mom and Dad, you have always been my biggest supporters. You have listened to me complain on the hard days and ramble on in excitement on the good days. You have provided me valuable guidance throughout my entire life and have forever stood by me. I cannot ever thank you enough for that. Alex and Josh, you are the best brothers in the world and never stop making me laugh. Thank you for always believing in me. Bubby, thank you for all of your encouragement and advice. Our regular phone calls filled with hilarious stories continue to make me smile. Thank you to all of my relatives for their support over the years. Rita, you have always pushed me to do my best and also been there with insightful advice when I needed it the most. I love you all and thank you for everything you have done to make me the person that I am today.

Thank you to all of my friends, new and old, who have been here through the journey that is grad school and made it a memorable one. You have made my experience at Berkeley so much better and I thank you for that.

Thank you to the wonderful past and present members of the Nitsche group who have made the lab and graduate school enjoyable (Ken, Jackie, Greg, Julie, Dan, Anthony, Paul, Kestrel, Tashi, Oliver, Deborah, Erin, Nick, Philip, Eva, Adam, Jeff, Stephen, Roxana, and Jon). Thank you Ken for taking over the group in this last year and making sure that we would all be able to finish our degrees. Thank you Dan for patiently answering so very many questions and concerns about XAS, for being an excellent beamtime buddy, and for all of the jokes. Thank you Anthony for the work that you put into the mesoporous silica project that helped propel Eva and I forward. Thank you Kestrel for teaching me how to be a better analytical chemist. Tashi, you are one of the toughest, most graceful, and talented chemists that I know, and I am grateful to have been able to learn from you. Oliver, you were one of my first friends in graduate school and you are still the person who I can count on to mock me in the best way possible. Thank you Deborah for being the wonderful person that you are; your kindness and humor have made grad school so much better; reactor school and beamtimes would not have been the same without you. Thank you Nick for always being optimistic and positive and for being a great person to talk music with. Thank you Jeff for all of the adventures and silly times, and for being supportive through the tough moments. Julie, Philip, Erin, Carolina, and Eva- you have been some really fantastic people to work next to over the last five years and I am so grateful to have had you as officemates. Thank you Julie for training me in the lab and for teaching me Frenglish (lay-toos!) and some very select French words. Thank you Carolina for being level-headed, supportive, and generally hilarious. Erin, I think our polar opposite approaches to nearly everything have made graduate school that much better. Thank you for all of the parties and dinners, putting up with my hyperactivity, and making sure we did not end up at a discotheque. Thank you Philip for listening to me when I wanted to talk, bringing in delicious baked goods, and making me smile with a neverending stream of puppy pictures. To my mesostorm and NMR partner, Eva, thank you for all of the talks about science and life and for the many fun adventures we had in Karlsruhe, Strasbourg, and Albuquerque. Thank you Jon Bowers for being a great undergrad and for keeping stuff moving when things got really tough. Thank you to Erin, Philip, Deborah, Eva, and Dan for each editing portions of this dissertation. Nitsche group, I could not have asked for a better group of people to have as a mentors and friends throughout graduate school.

A significant portion of my dissertation work was performed at Lawrence Livermore Na-

tional Laboratory. Thank you to Annie and Mavrik for hosting me as a practicum student and allowing me to continue doing work at the lab. Annie, I greatly appreciate all of the advice you have given me and your continued support as I move forward from graduate school. Harris, I owe you so very many thank you's. Thank you for teaching me everything that I know about NMR, trusting me to use the spectrometers, and answering many questions over the last two years. Thank you for all of your guidance and helping me to become a better scientist.

Thank you to my dissertation committee, Professors John Arnold, Darleane Hoffman, and Joonhong Ahn for their helpful advice. John, thank you for agreeing to be my dissertation chair at a time of great uncertainty in the Nitsche group and for all of your input on my dissertation. Darleane, I have enjoyed very much our conversations over the years and I especially appreciate all of the additional help you have provided to the group and to me in this last year. Professor Ahn, you have always been very encouraging and supportive of my work and I thank you for that.

I would like to thank the College of Chemistry staff, especially Lynn and Doty for everything they have done to help me navigate the intricacies of the department and school. Much of this work was funded by the Department of Energy (DOE) National Nuclear Security Administration (NNSA) Stewardship Science Academic Programs (Contract No. DE-NA0001978). I would like to thank the DOE NNSA Stewardship Science Graduate Fellowship for funding me throughout graduate school (Contract No. DE-NA0002135). Thank you to the staff at the Krell Institute for everything you have done to make being a fellow stress free and enjoyable.

Getting work done at LBNL would not have been possible nor nearly as enjoyable without the help of a number of staff at LBNL. David, thank you for your advice as I prepared to apply for jobs. Thank you Wayne for being patient and helpful with the many questions I have had over the past 5 years. Thank you to all of the EH&S support, particularly from the radiation protection group, especially John, Jeff, Naomi, Paul, and Israel. You have gone above in beyond in helping me get science done (...and clean it up when it did not go so well).

I would have never made it to Berkeley if it were not for various mentors who guided me on my path to graduate school. From Friends' Central School, I have to thank Deb Maraziti, who saw in me greater abilities than I saw in myself at the time. Deb, I thank you not only for your friendship, but also for pushing me and encouraging me to think creatively. I would not have become a radiochemist had I not participated in the ACS Nuclear Chemistry Summer School at Brookhaven National Laboratory. Thank you Rich for making that program such a great experience both the year I was a student and the year I was a TA. From Tufts University, I thank Professors Kounaves, Sykes, and Utz and Dean Knox because without their advice I am not sure I would have become a Chemistry major nor considered graduate school. Thank you Professor Utz for being my chemistry advisor and suggesting I go to graduate school. Professor Sykes, your classes were two of my favorite courses at Tufts, and I thank you for meeting with me to discuss everything from science to life after college. Dean Knox, I will never forget sitting in your office when I decided I did not want to major in chemical engineering and you suggested the major path that turned out to be a great fit for me. I appreciated being your advisee and you pushing me to take classes and to participate in activities that I may not otherwise have. Professor Kounaves, joining your research group in my junior year was a pivotal part of my college experience and ultimately the reason I decided to go to graduate school and get my Ph.D. I appreciate that you always had an open door and never turned away the undergrad who liked to ask many questions. I also appreciate the freedom you gave me; it is not often that a Professor will allow an undergraduate student to drive their experiments and dismantle equipment to see how it works. Thank you for everything you taught me.

And finally, there is Heino. Heino was an amazing advisor, mentor, and friend to me. He understood the way that I work and think better than most people I have encountered along my academic path. Heino was always there to talk about anything ranging from science to how life was going. He truly cared about his students not just as scientist, but as people. I am thankful to Heino for everything that he did to make me the scientist that I am today and I will be forever grateful to him for his support and confidence in my abilities. Heino, I will always aim high.

Chapter 1

Introduction

The ability to separate lanthanides and actinides both from one another and other elements is important for a variety of reasons including 1) treatment of used nuclear fuel and legacy defense wastes, 2) processing irradiated target materials, and 3) analyzing forensic samples.

In this country, there is an abundance of legacy defense waste and used nuclear fuel (UNF) from over 60 years of power and research reactor usage. Safe storage of this high level waste (HLW), both in terms of proliferation and introduction to the biosphere, requires that radionuclides are separated based on both chemical and radiolytic properties. The Plutonium URanium Extraction (PUREX) process, is used to extract plutonium and uranium (Pu and U) from these wastes, however, the remaining actinide and fission product constituents are stored together. Developing a separation that can isolate the minor actinides, namely Np, Am, and Cm, from the fission products and then isolate each of the minor actinides from one another would allow for a smaller volume of long-lived radiotoxic waste.

One separation that is of particular interest is that of Am and Cm from the trivalent lanthanides and then from each other. This is a difficult separation because of their near-identical chemical behavior. The isotopes of Cm produced from neutron capture and successive beta decays from U and Pu fuels have half-lives ranging from days to tens of years. The radioactive lanthanide isotopes produced have similar half-lives to the Cm isotopes. The isotopes of Am, however, are longer lived with half-lives ranging from hundreds to thousands of years. By separating the Am and Cm (partitioning), they can each be treated appropriately, resulting in preparation of Am for transmutation and Cm for storage in a repository.

Challenges in separations done on legacy wastes and UNF are encountered mainly due to the large volumes that ultimately must be treated. Large volumes of highly radioactive materials tend to have elevated temperatures from decay energy which can potentially destroy materials used for separations. Additionally these materials are in acidic, oxidizing solutions, required to dissolve UNF, with high salt content which creates a very corrosive environment. Radioactive decay can also degrade materials via radiolysis and hydrolysis reactions. Thus, materials used for separations must be temperature, corrosion, radiolysis, and hydrolysis resistant.

Current separation techniques are primarily based on liquid-liquid extraction systems. However, large volumes of hazardous organic wastes are generated via these methods. Improved solid-liquid separation systems would allow for the minimization of radioactive organic waste. The solid phases utilized throughout this work are solid supports modified in some way by an extractant ligand. This ligand is intended to complex with lanthanides and actinides, particularly trivalent species. The goal of this work is to utilize organically modified supports, or solid-phase extractants,

as a means of sequestering and separating trivalent lanthanides and actinides.

1.1 Constituents of Nuclear Fuel

A pressurized-water reactor (PWR) is a common power reactor that is fueled with low-enriched uranium (LEU). LEU is uranium that has had the ^{235}U content enriched to 2-5%. After standard PWR burn-up of 33 GWd/t and allowing the fuel to cool for 10 years for decay of the short-lived products, the fuel is still primarily composed of uranium. At this point, the fuel contains about 1% lanthanide fission products and 0.1 % minor actinides (Np, Am, Cm). [4] If the burn-up of the fuel were higher, the minor actinide content would increase. Additionally, with different types of starting fuel, the irradiated fuel composition varies. Mixed Oxide (MOX) fuel is composed of 90-93% depleted U and 7-10% Pu. As MOX fuel starts with a Pu component, the post-irradiation composition has a larger percentage of minor actinides. Thus, minor actinide separation and treatment is of greater concern for reactors employing MOX fuel than those using LEU. [4]

1.2 Partitioning and Transmutation

Partitioning is the separation of components of a mixture including both stable, short-lived, and long-lived radionuclides for the purpose of separately treating the various groups. This concept was developed with UNF in mind, particularly the separation of Am and Cm from the lanthanide fission products and one another. Ideally, Am would be separated from a UNF mixture and set aside for transmutation. Transmutation is the process in which longer-lived radionuclides are fissioned, creating short-lived fission products that can be stored in short-term geologic storage.

In transmutation, the longer-lived radionuclides are included in the fuel for a fast reactor and fissioned into shorter-lived species. A fast reactor is a nuclear reactor that utilizes 'fast' or high-energy (1-20 MeV) neutrons to sustain a nuclear chain reaction. Typically, power reactors operate with thermal and epithermal neutrons (0.025 eV and 0.025-0.4 eV, respectively), however the radionuclides intended for transmutation in fast reactors do not fission at those neutron energies. These nuclides tend to have larger fast neutron cross sections (probability of reaction) compared to their thermal neutron cross sections.

1.3 Trivalent Lanthanide and Actinide Separations

1.3.1 Solvent Extraction

Over the last 20 years, there has been great progress in advancing large-scale trivalent lanthanide and actinide separations. Some of the separation processes that have been of interest for trivalent lanthanide and actinides separations include TALSPEAK, DIAMEX-SANEX, EXAm, and GANEX. These are all solvent extraction methodologies, but their choices of ligands provide a good guide for designing ligands for solid-phase extractants. Many of the ligands of interest for trivalent lanthanide and actinide separations are discussed in thorough review articles. [5, 6] It should be noted that the European processes (DIAMEX-SANEX, GANEX, EXAm) are all based on ligands containing C, H, O, and N, which are completely combustible. Complete combustion of waste has been an aim in their nuclear fuel reprocessing program for the minimization of waste

byproducts. The American processes (TALSPEAK and TRUEX) both utilize phosphorous-based extractants, which are not completely combustible.

TALSPEAK (Trivalent Actinide-Lanthanide Separation by Phosphorous reagent Extraction from Aqueous Komplexes)is a heavily studied process with the goal of separating the trivalent lanthanides from the trivalent actinides. This is done with a phosphorous-based ion exchanger such as using di(2-ethylhexyl) phosphoric acid (HDEHP, Figure 1.1) in the organic phase and a holdback reagent, such as polyaminopolyacetic acid, in the aqueous phase to retain the actinides. The progress on this process has been thoroughly discussed in review articles. [7, 8]

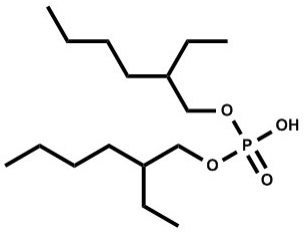

Figure 1.1: Structure of di(2-ethylhexyl) phosphoric acid (HDEHP)

DIAMEX(DIAMide EXtraction) and TRUEX (TRansUranic EXtraction) are both processed to remove the trivalent lanthanides and actinides from PUREX raffinate. SANEX (Selective ActiNide EXtraction)can then be employed to isolated the An(III) ions (DIAMEX-SANEX). [9] The DIAMEX process uses N,N'-dimethyl-N,N'-dioctylhexylethoxymalonamide (DMDOHEMA, Figure 1.2a) as the extractant. SANEX uses N-donor ligands such as $CyMe_4BTBP$ (6,6'-Bis(5,5,8,8-tetramethyl-5,6,7,8-tetrahydrobenzo(1,2,4)-triazin-3-yl)-[2,2']-bipyridine, Figure 1.2b) in conjunction with TODGA (Figure 1.2c). [9, 10] EXtraction of Americium (EXAm), is a separation process that evolved from the DIAMEX-SANEX systems. [11] The EXAm process is aimed at the extraction of Am and certain lighter lanthanides from a mixture of trivalent lanthanides and actinides, leaving behind the Cm and heavier lanthanides. In the EXAm system, the organic phase contains DMDOHEMA and the aqueous phase is nitric acid that contains tetraethyldiglycolamide (TEDGA).

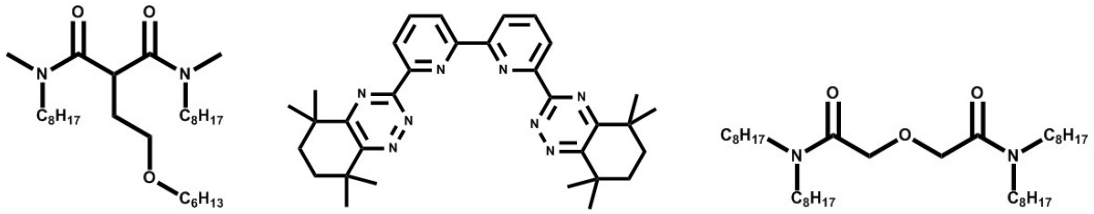

(a) DMDOHEMA (b) $CyMe_4-BTBP$ (c) TODGA

Figure 1.2: Structures of a) N,N'-dimethyl-N,N'-dioctylhexylethoxymalonamide (DMDOHEMA), b) 6,6'-Bis(5,5,8,8-tetramethyl-5,6,7,8-tetrahydrobenzo(1,2,4)-triazin-3-yl)-[2,2']-bipyridine, ($CyMe_4-BTBP$, and c) tetraocytyldiglycolamide (TODGA).

GANEX (Group ActiNide EXtraction) was developed to remove the actinides from the lanthanides and fission products directly from dissolved spent fuel or after only minimal processing. The extracts used in GANEX are BTBP and tributyl phosphate (TBP). [12, 13]

1.3.2 Resin-Based

Whether or not partitioning and transmutation is employed for UNF, advances in separations of the trivalent lanthanides and actinides are important for better isolating waste components as well as everyday tasks in a laboratory environment. One of the most famous methods of separating the trivalent lanthanides and actinides was pioneered by Choppin, Silva, Smith, and Hoffman in 1956. [14,15] These two important publications used cation exchange stationary phases (Dowex 50-X4 or Dowex 50-X12) and mobile phases of ammonium α-hydroxy-isobutyrate. Using this method, each of the lanthanides and the trivalent actinides can be separated from one another in succession. This method is still amongst a core set of separation techniques for trivalent f-block metals, however, it is a highly pH sensitive technique, requiring perfect execution to obtain sufficient separation factors.

Extraction chromatography resins are commercially available and have become the standard for many laboratory-scale separations. Eichrom Technologies has commercialized a number of resins that are intended for radiochemical separations. The DGA resin, in particular, is intended for the bulk extraction of trivalent lanthanides and actinides from acidic media. [3] This resin was an early focus of the work presented here and was the basis for the evolution of resin development. Additionally, there has been a great amount of work developing extraction chromatography resins utilizing the ligands that were found successful in solvent extraction systems for the nuclear fuel cycle. [3, 16–29] The transition from solvent extraction to solid-liquid systems is non-trivial; some of the important considerations are discussed in the Separations chapter.

The work presented here is aimed at contributing to the techniques available for sequestration and separation of trivalent lanthanides and actinides. A primary focus of this research has been to improve our understanding of how these materials interact with metals both on a macroscopic basis as well as on a molecular level. This detailed understanding of metal interactions with solid-phase extractants will allow for development of improved materials.

Chapter 2

Chemistry of the Rare Earth Elements, Lanthanides, Americium, and Curium

The lanthanide and actinide elements occupy the f-block of the periodic table, named as such because of the presence of f-orbitals in each of the atoms. There are seven f-orbitals that can contain up to 14 electrons. As a result of the changing energy of the f-orbitals across the lanthanide and actinide series, these elements can exhibit behavior ranging from being chemically similar to Group III metals, such as Sc and Y, to other transition metals with a wide range of oxidation states. Only a very brief synopsis of the chemistry of the f-block elements is given here.

2.1 Chemistry of Select Rare Earth Elements and the Lanthanides

The first lanthanide oxides were isolated between 1839 and 1843 by C.G. Mosander. [30,31] Throughout the discovery and isolation of the lanthanide elements, there was confusion as to how they fit with the rest of the periodic table as they mostly adopted the same +3 charge state. Most of the lanthanide elements were identified prior to 1907, however, promethium took longer to discover due to its lack of stable isotopes and difficulty in separating it from neighboring elements. [32]

An important characteristic of the lanthanide series is the lanthanide contraction. The lanthanide electron configuration is based on a xenon core with 4f, 5d, and 6s subshells available for electron filling. For La, the electron configuration is $[Xe]6\,s^2 5d^1$, as the 4f subshell is higher in energy than the 5d at this point. As electrons are added while progressing along the lanthanide series, the 4f shell contracts towards the Xe core and becomes lower in energy than the 5d shell. Therefore, as electrons are added, they go in the 4f shell, except for Gd, in which the configuration is $[Xe]6\,s^2 5d^1 4f^7$ instead of $[Xe]6\,s^2 4f^8$, because of the added stability of a half filled 4f shell. As a result of the contraction towards the Xe core, the 4f electrons are no longer able to participate in bonding and ions are formed through loss of the 6s and 5d electrons.

As a result of the extent of 4f contraction observed in the lanthanide elements, their bonds tend to be more ionic in character. This is compared to the actinide series, in which a contraction is still observed but to a lesser extent and bonds have more covalent character.

2.1.1 Measuring Select Rare Earth Elements and the Lanthanides

All of the lanthanide elements have stable isotopes except for promethium. Thus, they can be quantified via standard analytical techniques. For this work, inductively-coupled plasma optical emission spectroscopy and mass spectrometry were used to quantify Y, La, Nd, Eu, and Lu. The main atomic emission lines of each of these elements used for quantification on the ICP-OES are noted in Table 2.1 . ICP-OES, and especially ICP-MS, require very careful sample preparation.

Table 2.1: Atomic emission lines for select rare earth and lanthanide elements

Element	Line (nm)
Y	371.029
	361.105
La	398.852
	379.478
Nd	406.109
	401.225
Lu	261.542
	291.139

An alternate method that does not require any sample preparation is using a radioactive tracer. The main way that Eu was quantified in this work was via a radioactive tracer. A bulk of stable Eu was spiked with a ^{152}Eu tracer. ^{152}Eu has a half life of 13.2 y and decays via electron capture and beta minus decay. It emits a number of gamma rays with high intensities, detailed in Table 2.2. The bulk of the Eu quantification done using gamma spectroscopy in this work was focused on the 344 keV gamma ray as there were not interfering gamma emissions from either isotopic impurities in the Eu or the natural background.

Table 2.2: Primary Gamma and X-Rays of Select Radionuclides

Isotope	Gamma or X-Ray Energy (keV)	% Intensity
^{152}Eu	121.782	28.58
	344.279	26.5
	778.90	12.94
^{239}Np	106.13	27.2
	277.60	14.38
	228.18	10.76
^{241}Am	59.54	35.9
	17.75	5.7
	26.34	2.4
^{243}Am	74.664	68
	43.53	5.93
	13.946	7.3

2.1.2 Complexation Chemistry

The equilibrium associated with complex formation is described by the stability constant of a reaction (equation 2.2). The reaction being considered here is:

$$M^{n+} + L^{y-} \rightleftharpoons ML^{(n-y)+} \tag{2.1}$$

where M is the metal of interest and n is its charge state, and L is the complexing ion of interest and its respective charge state (y).

$$\beta_1 = \frac{[ML^{(n-y)+}]}{[M^{n+}][L^{y-}]} \tag{2.2}$$

In tables of stability constants, it is important to note the ionic strength and the temperature at which the values were measured. Additionally, verification of the definition of β for that particular table should be confirmed since there tends to be variation in this formalism. The values will often be listed as $\log(\beta)$, so small variations are significant.

As previously mentioned, the lanthanides, Sc, and Y are typically most stable in their trivalent state. Additionally they follow similar complexation trends with complexing ions. The complexation of these ions with some commonly encountered ions follows as:

$OH^- > F^- > NO_3^- > Cl^-$ [31]

This trend explains why precipitations with either hydroxide or fluoride are so successful. Moving across the lanthanide series, the stability constants increase. Other very strong complexants are EDTA and DTPA, however, these tend to complex all positively charged cations and thus are not selective but rather a bulk metal chelator.

Scandium and yttrium are unique in that they are part of the d-block, but tend to behave more like the later lanthanides, especially in the case of Sc. Unlike the early lanthanides, for instance, which form hydrolysis products starting around pH 4 or 5, Sc starts forming hydrolysis product under more acidic conditions. It most often adopts a coordination number of 6, followed by 8 in ordered crystals and aqueous solution. [33–36] However, in more disordered solid phases, Sc has been found to exist as the 7-coordinated species. [35–39] La, in the same group on the periodic table as Sc, adopts an average coordination number of 9, but will range from 7 to 12, due to its large ionic radius. [31, 40]

2.2 Chemistry of Americium and Curium

Americium was discovered by Glenn T. Seaborg, Ralph A. James, Albert Ghiorso, and Leon O. Morgan in 1945. [41] It was synthesized via neutron irradiation of plutonium and then sent to the Metallurgical Laboratory at the University of Chicago where it was chemically separated and isolated. Curium was discovered by Glenn T. Seaborg, Ralph A. James, and Albert Ghiorso in 1944. [42] The first curium isotope was synthesized at the 60-inch cyclotron at the University of California, Berkeley in 1944 and then sent to the Metallurgical Laboratory for chemical separation and isolation. Prior to 1944, the early actinides had been placed on the periodic table in the d-block due to their ability to exist in multiple oxidation states. Seaborg, however, determined that Cm could not exist in an oxidation state greater than (IV), causing him to develop the actinide hypothesis. The actinide hypothesis proposed that the Am and Cm be moved to the f-block below Eu and Gd and that the earlier actinides occupy that row in the f-block preceding Am.

In the earlier actinide elements, there is significant energetic overlap between the 6d and 5f orbitals, as the actinide contraction is not as pronounced as the lanthanide contraction. Thus, the

early actinides tend to exist in multiple oxidations states, often simultaneously, like the transition metals. The transition from Am to Cm is the point at which the actinides switch from transition metal behavior to more lanthanide-like behavior.

The electron configuration for Am is $[Rn]7s^25f^7$. Am readily exists in the trivalent state despite the breaking of the half-filled shell to transition from divalent to trivalent. This is likely due to the near degeneracy of the 6d and 5f orbitals in Am, making it easier to ionize electrons from the f-orbitals. While Am in aqueous systems is most stable as the trivalent cation, it has also been found to exist as Am^{4+}, AmO_2^{+}, and AmO_2^{2+}. The second most stable oxidation state for Am behind the trivalent is the pentavalent, [43] however, oxidation to this state typically requires either treatment with sodium bismuthate or ozonolysis. [44] The pentavalent state will disproportionate into the hexavalent and trivalent states, but the hexavalent will quickly reduce to the trivalent in solution. [43]

The electron configuration for the Cm atom is $[Rn]7s^26d^15f^7$. Thus for Cm, the most stable oxidation state is 3+, where the 7s and 6d electrons are removed from the atom to form the trivalent state. The half-filled f-shell is then stabilized and so forming the tetravalent Cm ion becomes more difficult as the f-orbitals have now contracted closer to the core. Cm in aqueous systems has only been found to exist in the trivalent or tetravalent state. [45]

2.2.1 Production and Decay Properties

For this work, the isotopes of Am used were 241 and 243. These are both produced in a nuclear reactor via the production pathway indicated in Figure 2.1. Both isotopes are formed from successive neutron captures and beta decays from a ^{238}U initial target. The ^{241}Am is produced by the beta decay of ^{241}Pu, whereas the ^{243}Am comes from two successive (n,γ) reactions on the ^{241}Pu, followed by beta decay of the resulting ^{243}Pu.

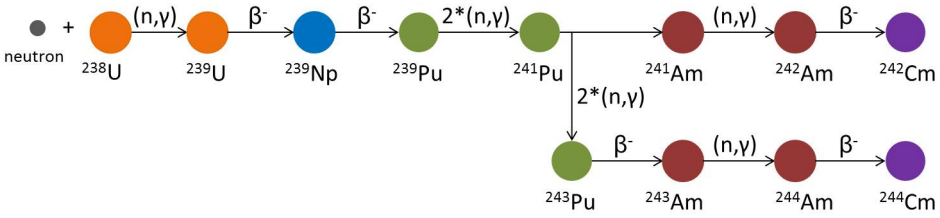

Figure 2.1: Production of americium and curium via neutron irradiation of a low-enriched uranium (LEU) in a reactor

^{248}Cm can also be produced in nuclear reactor from ^{238}U with multiple additional neutron capture and beta decay processes required. When ^{248}Cm is produced via this method, it is difficult to completely separate from the other isotopes of Cm with lower mass numbers, which are produced in greater quantity. As the ^{248}Cm half life is much longer ($t_{1/2}(^{248}Cm)=3.4\times10^{5}$ y compared to $t_{1/2}(^{246}Cm)=4730$ y and $t_{1/2}(^{244}Cm)=18.1$ y), even small impurities of the shorter lived isotopes can vastly alter the activity and thus must be well characterized via alpha spectroscopy. The ^{244}Cm, ^{246}Cm, and ^{248}Cm isotopes have associated alpha emissions with the energies listed in Table 2.3.

An alternate method of ^{248}Cm production is from the alpha decay of ^{252}Cf. ^{252}Cf can be produced from the irradiation of ^{238}U, however a more efficient means of production is by neutron bombardment on a mixed-isotope Cm target. ^{252}Cf has a short half life ($t_{1/2}(^{252}Cf)=2.645$y) and decays primarily by alpha decay to ^{248}Cm (branching ratio of 96.9%). This allows for the formation

Table 2.3: Primary Alpha Decays of Am and Cm

Isotope	Alpha Energy (keV)	% Alpha Decays
^{241}Am	5485.56	84.5
	5442.80	13.0
	5388.23	1.6
^{243}Am	5275.3	87.4
	5233.3	11.0
	5181	1.1
^{244}Cm	5804.82	76.4
	5762.7	23.6
^{246}Cm	5386.5	82.2
	5343.5	17.8
^{248}Cm	8078.45	81.9
	5034.93	18.03

of a pure ^{248}Cm stock without the co-production of other Cm isotopes. The disadvantage to this method is the added cost as it requires the additional steps of producing and isolating the Cf first.

It should also be noted that ^{248}Cm has a very high spontaneous fission branching ratio (8.4%). With each fission, an average of 2.5 neutron is released, resulting in the generation of a neutron field if there is a high enough activity of ^{248}Cm.

2.2.2 Measuring Am and Cm

The Am and Cm isotopes discussed above can all be measured by their alpha decay spectra. The alpha energies of each of these isotopes are detailed in Table 2.3. Each isotope will decay by a characteristic, well-known decay scheme. For example, the alpha spectrum of ^{248}Cm contains two primary peaks at 5078.45 and 5034.93 keV. The resolution of the peaks in the resulting alpha spectrum depends on the detector itself but the quality of the alpha plate can often make the biggest difference in resolution. When ^{248}Cm decays, however, it does not release any gamma or X-rays, which mean that the best way to measure it for bulk activity is either by alpha spectroscopy which can be slow, or liquid scintillation counting. Using liquid scintillation counting, the bulk alpha activity can be measured, however, it should be noted that alpha energy gating is not possible within these energies and so the isotopics of a particular sample must be well understood.

Both Am isotopes discussed above emit gamma and X-rays as they decay, making them easily measurable with gamma spectroscopy. The gamma energies of interest are included in Table 2.2.

Am can also be measured by alpha spectroscopy or liquid scintillation counting, again being sure to carefully quantify the isotopic composition of the radionuclide stocks in use.

When determining relative amounts of Am and Cm in a mixture, both gamma spectroscopy and liquid scintillation were used, where each sample was counted with both techniques. The Am concentration was determined from the gamma spectra and then subtracted from the bulk alpha activity measured via liquid scintillation counting (LSC).

2.2.3 Complexation Chemistry

In high concentrations, Am(III) is pink, whereas Cm(III) is colorless. In aqueous solution, metal ions can form hydroxide complexes as a function of pH as indicated in Equation 2.3.

$$M^{n+} + mH_2O \rightleftharpoons M(OH)_m{}^{(n-m)+} + mH^+ \tag{2.3}$$

The degree of hydrolysis for each metal is dependent on the pH of solution, the presence of CO_2, and the metal oxidation state. For Am, significant hydrolysis products begin to form at pH 5. [46] This is similar for Cm and other trivalent lanthanides and actinides. Plutonium, for instance, begins to form hydrolysis products around pH 3 when in the tetravalent state, however can exist as the bare cation (surrounded by water molecules) at higher pH when in the trivalent state. All of the actinide chemistry presented in this work was conducted below the pH at which hydrolysis products are expected to form for either Am or Cm.

Like the trivalent lanthanides, Am and Cm form insoluble precipitates with fluoride, phosphate, hydroxide, iodate, etc. Additionally, Am and Cm form complexes to varying degrees with nitrate and chloride, following the trend:

OH^->F^->$H_2PO_4{}^-$>SCN^->$NO_3{}^-$>Cl^->$ClO_4{}^-$ [46]

The similar complexation chemistry between the lanthanides, Am, and Cm with these counter ions are part of the reason their separation is challenging. With chelating ions, their stability constants are more varied, making separations based on these extractants potentially more promising.

Chapter 3

Separations Background

3.1 Solid-Phase Extractants

Solid-liquid separations often utilize solid-phase extractants (SPEs) in place of the organic phase used in a liquid-liquid separation. The aqueous phase from a traditional liquid-liquid separation becomes the mobile phase in a solid-liquid system. The overall purpose of a SPE is to extract the metal or molecule of interest from the mobile phase. The type of SPEs that will be introduced in this section have two components: 1) a solid support and 2) an extractant ligand. The two components of these materials that will be discussed in this chapter are the solid supports and the method of attaching the ligand to the solid support. The ligands themselves are discussed in later chapters.

3.1.1 Solid Supports

The purpose of the solid support in a SPE is to create a stable, uniform platform for the extractant ligand. Common solid supports are polymer or silica beads. The morphology of the support can vary substantially ranging from a mixture of shapes and sizes to uniform spherical particles. As the end use of SPEs is typically chromatography, it is important to have spherical particles. This will be discussed further in the chromatography section. In addition to particle shape and size, the porosity of the support is variable. SPEs with non-porous and completely porous supports have been presented in the literature in addition to supports with solid cores and porous outer layers for the extract of lanthanides and actinides. [23, 47–56] Porosity can offer the advantage of higher ligand loading on the support as a result of a higher surface area.

Polymer

One of the most common solid supports for SPEs are polymer beads. Polymers with styrene and divinylbenzene backbones have become especially prominent in chromatographic materials. [57] One particular advantage to using polymeric supports is their stability at a wide range of pH values. This can be more problematic with silica, as silica dissolves in base typically above pH 9. [58]

Silica

The bulk of the work present in this dissertation is focused on silica based solid supports because of their chemical stability in acidic environments, amenability to ligand grafting, and potential for direct vitrification at end of use. The ability to covalently bond ligands to the silica support is an especially important quality in generating stable, reusable SPEs. Silica is particularly interesting because of the large amount of investigation into various morphologies and porosities available in the literature. While non-porous silica beads have been used in developing solid-phase extractants in many instances, porous materials offer the advantage of larger surface area.

Of particular interest for this work was mesoporous silica, which has pores with diameters in the range of 2-50 nm. Ordered mesoporous materials were first proposed by Beck, et al, in 1992 regarding mesoporous aluminosilicates. [59, 60] They coated a micelle template with an aluminate-silicate mixture prior to removing the template via calcination. This was the development of MCM-41 (Mobil Composition of Matter), which has a 2D hexagonal pore stucture. An alternative 2D hexagonal mesoporous silica was soon discovered by the Stucky group at UC Santa Barbara. [61] They developed a series of materials denoted SBA-# (Santa Barbara Amorphous) where # is a number associated with that particular material. SBA-15 is an especially well known 2D hexagonal mesoporous silica developed by the Stucky Group. The Stucky group also developed mesocellular foam (MCF) materials, which are mesoporous silica substrates that have a 3D cubic structure. [62, 63] The pores in this case are on the larger scale of mesoporous ($\sim$30 nm) and spherical. This compares to SBA-15 which has cylindrical pores with a diameter typically less than 10 nm.

Ordered mesoporous materials are unique and appealing as a substrate for solid-phase extracts for a number of reasons. First, they have very high surface areas, typically greater than 700 m^2g^{-1}. High surface area means that a greater number of ligands can be grafted on the material compared to a lower surface area analog. Second, these are well ordered materials which allow for an understanding of how the ligands may be filling the pores of the material. Third, they can be synthesized with a number of different pore sizes and shapes which makes it possible to tailor the material to the application of interest. Last, the particles can be made spherical, which is ideal for chromatographic applications. Spherical particles allow for well-ordered, homogenous packing in a column, and minimize the potential for void spaces.

3.1.2 Attachments

The way in which the extractant ligands are immobilized on the solid support can greatly impact the efficacy of a SPE. Variables such as the stability and reusability, extraction efficiency, and variety of available ligands are all dependent on the attachment method that is selected. The three ways in which ligands are commonly immobilized when synthesizing SPEs for lanthanide and actinide extractions that will be focused on here are coating, impregnating, and grafting.

Coated

The attachment method that is often used for SPEs, especially those used for radiochemical separations, is coating the solid support with the extractant ligand. This is done by dissolving the ligand in a volatile solvent and combining this mixture with the solid support. The support particles and ligand solution are agitated continuously until the solvent is evaporated completely using a rotary evaporator. The particles are then rinsed to ensure that excess trapped solvent or ligand is removed. The main advantage to this method is the ease of synthesis and large number of

ligands available for use because they do not need any modifications to make them more reactive towards functionalization.

It is important to note that in the case of coated materials, the ligand is not covalently bound to the support, but rather associated with it via electrostatic interactions. The ligands can be oriented in any direction, therefore the ligand densities provided for such materials may not be an accurate assessment of ligands that are actually available for binding. The ligands are able to hold on to the solid support during a separation because of the relative polarity of the stationary phase compared to the mobile phase. In most solid-liquid separations the mobile phase is aqueous which will not dissolve the organic ligands coating the solid-supports. However, time, pressure and/or acid-catalyzed hydrolysis of the ligands can cause decomposition of this organic layer. The result is resin that decomposes over time and may not have consistently predictable behavior.

Impregnated

Impregnated resins contain an extra component compared to coated and grafted materials to immobilize the ligand. These materials are made by mixing the ligand of interest into a polymeric matrix. The polymer-immobilized ligands are then coated on a porous support (typically silica or carbon), which allows the polymer to fill the pore vacancies of the support. By immobilizing the ligands in this fashion, the material should be more robust. [16, 18, 21, 52] However, the ligand orientation is still unpredictable and the random ordering of the ligands in the polymer matrix can result in inaccessible ligand configuration for complexing metals.

Grafted

In a grafted SPE, the ligand is covalently bound to the solid support. This can be done in a number of ways depending on the support material and desired ligand. One method is to build the extractant up from the surface by creating anchor groups on the surface that would react with the ligand. Another method, and the one that was used for the work presented in chapters 6 and 7, is to use ligands that have an anchor group reactive towards the support material, in this case, silica. An advantage of grafting the ligand to the support is that the material should be more stable over time and in the presence of acidic matrices, because the ligand should not easily wash off. [16, 18, 21] Another advantage is that covalently binding the ligand to the surface avoids the ligand becoming inaccessible as a result of being trapped in the solid support. [64] However, a disadvantage that has been challenging to overcome is the limitation in ligands that can be bound to the solid supports. The difficulty arises because the ligands already have reactive binding sites that are required to complex a metal and these sites can also be reactive during the grafting reaction. Additionally, a number of the ligands that are of interest for trivalent lanthanide and actinide extractions decompose in the presence of air or water which makes them degrade during the process of attaching an anchor group.

The idea of covalently binding organic ligands to mesoporous silica for sequestration of heavy metals including the lanthanides and actinides was originally developed by Glen Fryxell and co-workers at Pacific Northwest National Lab. They published a number of papers on this topic, [54, 65–72] however creating a more fundamental understanding of the behavior of these materials was not a focus of these manuscripts. Further work on these materials was also performed by Bourg, et al. [17]

3.2 Solid-Liquid Separations

3.2.1 Batch Experiments

In liquid-liquid separations, the degree of extraction of a component from the aqueous phase into the organic phase is quantified by the distribution ratio, D. The distribution coefficient is the ratio of the concentration of component 'A' in the organic phase relative to the aqueous phase (equation 3.1).

$$\mathrm{D} = \frac{A_{org}}{A_{aq}} \tag{3.1}$$

When attempting to separate two components, A and B, the extent of separation is quantified by the separation factor, SF. The separation factor is the ratio of the distribution coefficients of components A and B (equation 3.2).

$$\mathrm{SF} = \frac{D_A}{D_B} \tag{3.2}$$

In considering solid-liquid separations, the quantification of distribution ratios and separation factors is similar but not exactly the same as in liquid-liquid systems. The analogous term to a distribution ratio in solid-liquid systems relates the amount of component 'A' bound to the solid phase to that remaining in the solution phase.

$$\mathrm{K_{d,A}} = \frac{C_{A,sol}}{C_{A,soln}} = \frac{\frac{n_{A,sol}}{m_{sol}}}{\frac{n_{A,soln}}{V_{soln}}} \tag{3.3}$$

In equation 3.3, $\mathrm{C_{A,sol}}$ and $\mathrm{C_{A,soln}}$ are the concentration of A on the solid phase and in the solution phase, respectively. It is important to note that $\mathrm{C_{A,sol}}$ is measured in moles of A ($\mathrm{n_{A,sol}}$) per gram of the solid phase ($\mathrm{m_{sol}}$) and $\mathrm{C_{A,soln}}$ in moles of A ($\mathrm{n_{A,soln}}$) per mL ($\mathrm{V_{soln}}$) of solution phase. The units of the $\mathrm{K_d}$ value are $\frac{mL}{g}$.

Another way to present the amount of metal sorption to the solid phase is by considering the percent sorption. Percent sorption is calculated according to equation 3.4.

$$\%\mathrm{Sorption} = \frac{A_0 - A_{soln}}{A_0} \times 100 \tag{3.4}$$

The limitation of considering percent sorption is that it does not account for variations in solution volume or mass of solid between samples. Thus, when comparing samples using percent sorption, it is important that they all have the same mass of solid and volume of solution and that slight deviations are accounted for in the error.

When comparing the degree of separation of two components, A and B, the analogous term in a solid-liquid system to a separation factor in a liquid-liquid system is the selectivity factor, α. The selectivity factor is the ratio of the distribution coefficients for components B to A (equation 3.5). Unfortunately, there is ambiguity with naming this ratio 'selectivity' and it is often still referred to as the separation factor, thus one should always be careful to verify how variables are defined in specific scenarios.

$$\alpha = \frac{K_{d,B}}{K_{d,A}} \tag{3.5}$$

When α is equal to 1, there is no separation of A and B. In the case were $K_{d,B}$ is greater than $K_{d,A}$, a larger α value indicates greater separation. For chromatographic purposes, an α value that is too large indicates an inefficient separation, so optimization of this ratio is important to obtain both efficient and complete separations.

3.2.2 Chromatography

The solid phase in a chromatographic column is called the stationary phase, and will be referred to interchangeably from here on in. Various components of a chromatographic separation can affect its efficiency.

In chromatographic separations, the separation factor is defined differently than in batch experiments. The separation factor, γ, is the ratio of the retention volume (V_r) of two components (equation 3.6).

$$\gamma = \frac{V_{r,B}}{V_{r,A}} \times (\gamma - 1) \tag{3.6}$$

The γ value only accounts for the difference between the peak maximums for each component A and B, but does not address the width of each peak. To truly quantify the degree of separation, the width must be considered. Ideally, baseline separation of two components is obtained, which is defined as having a resolution, R, greater than 1.5. Resolution is defined in equation 3.7 as the ratio of the difference in retention volumes (ΔV_r) between the two components to the average peak width(w_{avg}).

$$\mathrm{R} = \frac{\Delta V_r}{w_{avg}} = \frac{\sqrt{N}}{4} \times (\gamma - 1) \tag{3.7}$$

As evident in equation 3.7, resolution can also be expressed in terms of the separation factor and the number of theoretical plates, N. The number of theoretical plates is defined in equation 3.8.

$$\mathrm{N} = \frac{L}{H} \tag{3.8}$$

In equation 3.8, L is the length of the column bed, and H is the height of a theoretical plate. The height of a theoretical plate is the measure of length of the column bed that is required for equilibrium to be established for a component between the stationary and mobile phases. The number of theoretical plates is the number of these 'equilibration regions' that exist in the column bed. The more equilibration regions a component encounters, the better the overall separation. To maximize separation efficiency, the number of theoretical plates should be maximized and the plate height minimized. Of these values, the one that is tangible and can be controlled in experimental design is the length of the column. As N is directly related to L, increasing the length of the column, should increase peak resolution.

When designing a chromatographic separation, a number of factors must be considered. Column length was already mentioned as being important to increasing resolution. Another important factor is flow rate. Increased flow rate minimizes the longitudinal diffusion, or band diffusion

along the column axis. However, if flow rate is increased too much, the solute (e.g. component A), may not have time to equilibrate between the mobile and stationary phases. Lastly, there is the impact of the width of the column. Comparing two columns packed with the same stationary phase, a wider column would offer a larger number of possible diffusion pathways. This can lead to band broadening and wider peaks in a final chromatogram. Ideally long, narrow columns with an optimized flow rate will lead to the best separations.

One last factor that is important when designing a stationary phase material, is the particle shape. Flow through a column is the most predictable and reproducible when uniformly-sized spherical particles are used. Uniformly-sized spherical particles can densely pack a column, whereas irregularly shaped particles lead to void spaces and potential channels in the resin bed. When the particles do not exhibit an average spherical shape, the separations may not be reproducible as flow patterns and back pressure can vary substantially. For the work presented in Chapters 6 and 7, the mesoporous silica was synthesized such that spherical particle shapes were obtained. There is a trade-off, however between particle shape and pore-diameter and that was a large challenge encountered during the initial material development stage of the project.

Chapter 4

Experimental Methods

4.1 Preparation of Stock Solutions

4.1.1 Non-radioactive stock solutions

Stock solutions of La, Nd, Y, Al, and Lu were all prepared from either the $M(NO_3)_3$ or MCl_3 hydrous salts, and the Sc stock was prepared from anhydrous $Sc(NO_3)_3$. The salt was then dissolved in the desired volume of either HCl or HNO_3 depending on the end use. For stock solutions needed for ICP-OES analysis, a dilution was made by weighing the stock and 2% HNO_3 to make a stock dilution that was less than 10 ppm. This allowed for the stock solution to be dilute enough to measure into the samples.

4.1.2 Europium stock

Depending on the end purpose, one of three different types of Eu stock was prepared. The three types were: 1) stable $Eu(NO_3)_3$, 2) $^{152}Eu(NO_3)_3$ or $^{152}EuCl_3$ with no carrier, or 3) $^{152}Eu(NO_3)_3$ or $^{152}EuCl_3$ with carrier. For the stable Eu stock (1) or the carrier solution for (3), either $Eu(NO_3)_3$ or $EuCl_3$ salts were weighed and dissolved in either HNO_3 or HCl at an acid concentration ≥ 0.001 M. For stocks (2) and (3), an aliquot of $^{152}EuCl_3$ was evaporated to dryness under a heat lamp and redissolved multiple times in either dilute HCl or HNO_3. Upon the final evaporation, the residue was either dissolved in HCl or HNO_3 with an acid concentration ≥ 0.001 M for (2) or in the previously prepared carrier solution of interest for (3).

4.1.3 Americium stock

For the Eichrom DGA column experiments, ^{241}Am was used at trace concentrations. The preparation of this stock involved boiling an aliquot of ^{241}Am stock to dryness, redissolving, and repeating those steps multiple times. Final dissolution was in 3 M HNO_3. To measure isotopic purity of the stock, an aliquot of the stock was diluted and used to make an alpha plate. Alpha spectra confirmed ^{241}Am purity with minimal in growth of the ^{237}Np daughter (Figure 4.1).

All other Am experiments were done with ^{243}Am to minimize radiation dose when working at greater concentrations of Am. Therefore, from now on in this thesis, when Am is discussed it is referring to ^{243}Am unless explicitly noted as ^{241}Am. The ^{243}Am stock was made after purifying a collection of ^{243}Am in a matrix that include $HClO_4$, HNO_3, and HCl amongst other components. The Am was precipitated with a LaF_3 co-precipitation, adapted from the classical techniques noted

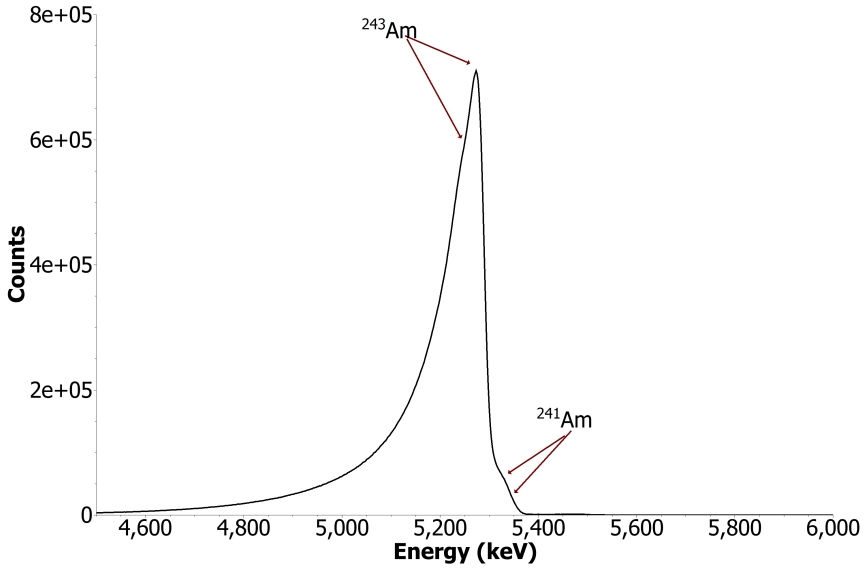

Figure 4.1: Alpha spectrum of ^{243}Am stock

for precipitating Pu(III), Am(III), and Cm(III). [73,74] For the LaF_3 co-precipitation, an aliquot of 5 mg mL^{-1} $La(NO_3)_3$ solution was added directly to the Am solution in centrifuge tubes such that approximately 1 mg of La was added to each sample. Each sample was brought to 2 M in HF using concentrated HF (extra caution must be used when handling HF). Samples were allowed to react for at least 30 min, preferably rocking. The samples were then centrifuged, and the supernatant was set aside for analysis. The precipitate was dissolved in 2 mL of a solution 1 M in each HNO_3 and HF. Samples were allowed to rock for another 30 min prior to centrifuging and removing the supernatant. The dissolution, rocking, centrifuging, and separating procedure was a repeated a total of 3 times. The final $La(Am)F_3$ precipitate was dissolved in 1.5 mL of 3 M HNO_3 saturated with H_3BO_3.

To separate the La from the Am, a procedure was adapted from Maxwell, et al. [75] The dissolved precipitate was loaded onto a Normal DGA resin cartridge (Eichrom Technologies, Inc) that had been conditioned with 3 M HNO_3. The column was rinsed with 5 column volumes (CVs) of 3 M HNO_3, then La was eluted in 0.1 M HNO_3, prior to elution of Am in 0.25 M HCl. To verify that La eluted in the proper matrix, a non-radioactive test using La only with no Am was done and the La concentration was measured using ICP-OES. The final purified container of ^{243}Am was in 0.25 M HCl. The isotopic composition of this was determined using alpha spectroscopy (Figure 4.1). To summarize, the ^{243}Am has ^{239}Np in secular equilibrium. Additionally, there is a small amount (0.2%) of ^{241}Am present, however, at these concentrations, the ^{241}Am is not expected to influence the nuclear counting, especially since most of the measurements are relative to one another. After purifying the main container of ^{243}Am, the stock preparation was quite similar to that for the ^{241}Am stock. Multiple boilings and dissolutions in the appropriate acidic matrices were done to change between HCl and HNO_3 matrices. For the $AmCl_3$ stock, the Am residue was dissolved in 0.001 M HCl. For the $Am(NO_3)_3$ stock, the Am residue was dissolved in 0.001 M HNO_3.

4.1.4 Curium stock

Cm was recovered from large volumes of old collection solutions that contained $HClO_4$, HNO_3, HCl, and polypropionic acids. Due to the presence of both organic matter and perchlorate, the solutions could not simply be boiled to reduce volume as this would result in a potentially explosive mixture. With the same co-precipitation with LaF_3 that was used for Am (Section 4.1.3), Cm was precipitated and that solid was dissolved in 3 M HNO_3 saturated in H_3BO_3. The procedure developed for the curium separation from La was based on that used by Maxwell for the DGA resin separation. [75] The dissolved precipitate was loaded onto a pre-packed Normal DGA resin cartridge (Eichrom Technologies, Inc; 2 mL bed volume) that had been conditioned with 3 M HNO_3. After loading the La(Cm)F_3, the column was washed with approximately 5 CVs of 3 M HNO_3. The La was eluted with 20 CVs of 0.05 M HNO_3, prior to eluting the Cm in 10 CVs of 0.25 M HCl. The Cm was analyzed by alpha spectroscopy and was found to be primarily ^{248}Cm, however, there is a small percentage of ^{244}Cm and ^{246}Cm, likely due to the production method (Figure 4.2).

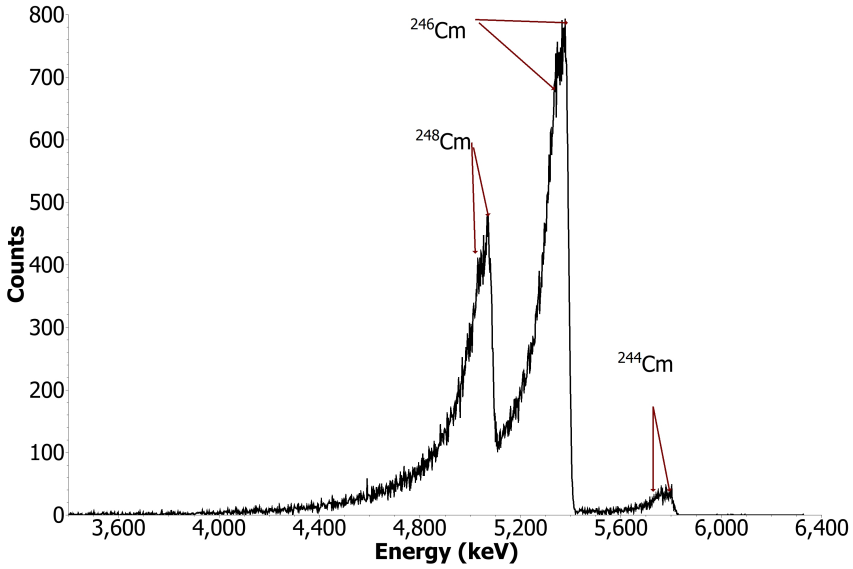

Figure 4.2: Alpha spectrum of ^{248}Cm stock

To determine if the presence of 244 and 246 required corrections to activity measurements, the ^{248}Cm was calculated both with and without activity corrections. These two numbers were very close and thus, it was determined that subsequent corrections were not required due to the very small amounts of 244 and 246. The Cm stock was prepared by evaporating the Cm recovery solution to dryness under a heat lamp and dissolving multiple times in HNO_3 to drive off excess HCl. The final residue was dissolved in 3 M HNO_3.

4.2 Preparation of Mesoporous Silica

The mesoporous silica synthesized in this work was SBA-15 type, which has a 2D hexagonal pore structure. Pores can be varied in diameter from about 0.5 to 10 nm. To obtain larger pore diameter, swelling agents are used. Too much of the swelling agent, however, can cause the cylindrical pore to close in at regular points forming nodes which results in a 3D cubic structure

with spherical pores. The SBA-15 was synthesized such that the particles would be spherical, which as explained earlier, is required for reproducible chromatography. The procedure optimized by Dr. Anthony Bruchet for spherical SBA-15 particles was based on the work of Katiyar, et al. [76]

Cetyltrimethyl ammonium bromide (CTAB, 0.45 g), 18.75 mL of Milli Q water (18.2 MΩ • cm), and 0.68 g of trimethylbenzene were combined (Mixture 1). Pluronic P123 ($PEO_{20}PPO_{70}PEO_{20}$, 2.25 g) was dissolved in 45 mL of 1.5 M HCl (Mixture 2). Mixture 2 was particularly difficult to dissolve, and benefits from allowing to rock (on a rotoshake) overnight. In this case, Solution 1 should also be rocked overnight. The P123 and CTAB mixtures were then combined in a PTFE bottle and stirred at 250 rpm for 10 min before adding 15 mL of ethanol dropwise. The solution was then allowed to thermalize at 35 °C for 3 h stirring at 500 rpm. It was important that after addition of each reagent to the reaction that the PTFE bottle was tightly capped to prevent evaporation of the reagents. Tetraethyl orthosilicate (TEOS, 7.5 mL) was then added dropwise to the surfactant solution, and the mixture was stirred at 500 rpm for another 45 min. The PTFE bottle was then transferred to a thermostated ethylene glycol bath and stored under static condition at 80 °C for 6 h before moving to a ventilated oven and stored for another 14 h at 130 °C. When opening the bottle after completely cooling, caution must be used in case any pressure has built up during the reaction. After allowing to cool completely, the solid was recovered by vacuum filtration. Filtration can be challenging as a result of unreacted surfactant bubbling in the filtration setup. To minimize this, after wetting the filter paper, all of the silica mixture was quickly added at once with the vacuum pulling at a moderate level of suction. The solid was washed with deionized water, and dried overnight. To remove the organic template, the as-synthesized materials were calcined in one of the Yang Group (UC Berkeley) muffle furnaces (Thermolyne Muffle Furnace, Thermo Scientific, USA) at 550 °C for 6 h with a heating rate of 1 °C/min.

When the P123 did not completely dissolve in the HCl, the particles synthesized were still mesoporous, but the pore diameter was only about 4.5 nm. It is believed that the low pore diameter of some materials was due to poor dissolution of the P123, which is also necessary for reproducibilty.

4.3 Functionalization of Mesoporous Silica

There are three types of functionalization methods discussed in this work: 1) monomeric, 2) surface polymerized, and 3) solution polymerized. For the CA-SBA material, all three materials were studied, however, for the DGA-SBA, only the solution polymerized method was used. Functionalizations of the CA-SBA and DGA-SBA materials were done by Anthony Bruchet and myself, respectively. The difference between these three methods is the extent of polymerization possible for the ligands which is controlled by the amount of water added to the reaction. [77]

Monomeric functionalization is the most common functionalization method for silica materials used for chromatography resins. [78] This method does not use any water in the reaction and thus should result in the most homogeneous ligand dispersal on the surface of the silica substrate, and in turn, the least polymerization. A benefit of this method is that it allows for each ligand to form multiple anchors to the substrate. With two or three linkages to the surface, the stability of the material in the presence of highly acidic matrices and radiation dose should be enhanced. A potential disadvantage of this type of functionalization is the distance between each ligand. With distant, evenly dispersed ligands, it can be difficult to form complexes with multiple ligands per metal center, which are often required for lanthanide and actinide binding.

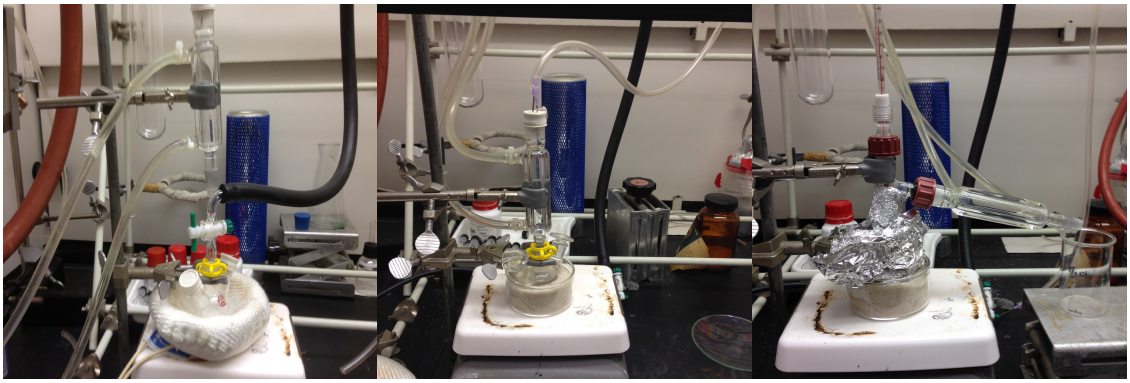

(a) Evacuating and Drying (b) Refluxing (c) Distillation

Figure 4.3: Setup for functionalization of mesoporous silica with organic ligand. The silica is first evacuated and dried (a), there is a 6 hour refluxing step after the ligand is added (b), and finally the methanol, water, and some toluene are distilled (c).

Surface and solution polymerization techniques are both intended to allow the ligands to polymerize with one another. Surface polymerization uses minimal water, only that present in the atmosphere and nitrogen gas that has not been dried. Ideally, this would result in ligands polymerizing once they have started to graft to the surface. Solution polymerization, the method utilized by Fryxell, [79] is used to form monolayers on the surface by adding a stoichiometric amount of water to the reaction. This allows the ligands to condense and form polymer chains before binding to the surface. One caveat with this method is that monolayers are not possible with all ligands; if the ligands are bulky, steric hindrance will prevent the formation of long polymer chains. A discussion on monolayer formation on silica surfaces is provided in the review article by Onclin, et al. [80]

For solution polymerization, the desired amount of calcined silica and a small stir bar were added to a three-necked round bottom flask that had been dried overnight in a 120°C oven. The canula and syringe used for the toluene were dried in the same oven overnight. The round bottom flask was set on top of a heating mantle and then connected to a Schlenk line through the middle neck. The two other necks were capped with syringe ports. The valve to the flask was closed at this point, in addition to the valves to all other lines except vacuum. Slowly, the vacuum was opened and the Schlenk line was allowed to evacuate for at least 10 minutes. Once evacuated, the valve to the flask was opened very slowly, to avoid pulling the silica from the flask into the line. At this point, the heating mantle, controlled by a variac, was set to 120°C and the stir plate turned on to allow even heat dispersion. The particles were allowed to dry under vacuum overnight (Figure 4.3a). After drying, the vacuum valve was closed slowly and the flask gently lifted off of the heating mantle and allowed to cool to room temperature. The vacuum was shut off and the schlenk line flushed with nitrogen.

Slowly the nitrogen port was opened to the flask and the flask was flushed with nitrogen for a few minutes. The required amount of toluene, a monolayer worth of ligand (Equation 4.1), and the stoichiometric equivalent of water (Equation 4.2) were added through the syringe ports if possible, avoiding opening the flask to atmosphere. The required amount of toluene is determined based on the mass of silica in use. The ratio of silica mass to toluene volume for this work was 15 mg/mL. The syringe ports were quickly removed and exchanged with glass caps held on with keck clamps. The flask was set in a sand bath on top of a hot plate-stirrer with the stirring turned on

(Figure 4.3b). The heat was set such that the toluene heated and condensed gently during reflux. Wrapping the flask in foil helped to maintain a more even heat gradient throughout the flask. The reaction was allowed to run for 6 hours. After six hours, the nitrogen to the flask and Schlenk line was shut off. The flask was detached from the Schlenk line and a distillation head was quickly attached to the center neck of the flask. A thermometer was inserted in the top of the distillation head to monitor the distillation temperature Figure 4.3c). Heating the mixture allows first for the distillation of methanol, followed by water, both of which should be collected in beakers. There is a water/methanol azeotrope at 80 °C. At 110 °C toluene starts to distill. Typically about 50% of the toluene was distilled off for volume reduction purposes. Once toluene distillation was completed, the flask was removed from the heat and allowed to cool. Once cool, the particles were filtered via vacuum filtration over a 0.22 μm filter. They were rinsed with toluene followed by acetone then isopropanol, and allowed to air-dry in the hood overnight. The particles were then collected and stored in a desiccator.

$$\mathrm{mL}_{\mathrm{silane}} = \frac{(silane/nm^2)_{used} \times 10^{18}}{N_A} \frac{SA_{silica} \times m_{silica} \times MW_{silane}}{\rho_{silane}} \tag{4.1}$$

$$\mathrm{mL}_{\mathrm{H_2O}} = \frac{(waters/nm^2)_{used} \times 10^{18}}{N_A} \frac{SA_{silica} \times m_{silica} \times MW_{water}}{\rho_{water}} \tag{4.2}$$

In Equations 4.1 and 4.2, SA_{silica} is the surface area of the silica in $m^2\ g^{-1}$, m_{silica} is the silica mass in g, MW and ρ are the molecular weight and density, respectively, of either the silane or water, and N_A is Avogadro's number.

4.4 Characterization Techniques

A number of different characterization techniques were necessary for various components of this project. These included characterization of the mesoporous silica after synthesis, the organically-modified mesoporous silica, and the metal contacted organically-modified mesoporous silica. To do this, a variety of methods were utilized including scanning electron microscopy, nitrogen adsorption isotherms, thermogravimetric analysis, infrared spectroscopy, and nuclear magnetic resonance spectroscopy.

4.4.1 Scanning Electron Microscopy

In scanning electron microscopy (SEM), an electron beam (1-30 keV) is rastered across a sample and the scattering of the electrons off the sample are used to create an image. [81, 82] A scanning electron microscope is composed of an electron gun that ejects electrons through a number of condenser lenses and focusing optics prior to hitting the sample. Back scatter detectors are located above the sample, adjacent to the electron beam entrance window. The secondary electron detector is typically next to the sample at about 90 ° to the electron beam path. There are often also x-ray detectors at a known trajectory angle from the sample. While SEM can be conducted in various levels of pressure, all measurements done of the mesoporous silica in this work were performed under high vacuum. The benefit of operating under high vacuum is the ability to measure lower energy emissions.

There are a number of different ways that the electrons from the beam can interact with the sample: 1) elastic scattering (back scattering), 2) ejection of a secondary electron (SE),

and 3) ejection of an auger electron. Each of these processes have different energies associated with them and thus require different means of detection. The most common form of detection measures the SE, which are generated from atoms on the surface of the sample. Thus, measuring SEs elucidates surface features and morphology. The energies of back-scattered (BS) electrons, however, are dependent on the Z of the material and thus can inform about the elemental mapping in the sample. When a core level electron vacancy is formed, it is filled by an electron from a higher energy level, which subsequently releases energy either in the form of a photon or an electron, known as an Auger electron. Measurement of Auger electrons required operating the SEM under high vacuum.

SEM was used to examine the particle shape and estimate particle size of the mesoporous silica. Dr. Anthony Bruchet conducted the microscopy of the mesoporous silica particles on the Yang Group (UC Berkeley) SEM. The SEM micrographs were collected on a JEOL JSM-6340F (JEOL, USA). The silica sample was prepared by suspending the silica in ethanol and depositing it on a glass slide. Double-sided copper adhesive tape was then used to remove a thin layer of silica from the glass slide. The silica on copper tape was then coated with 5 nm of gold using a Desk IV cathodic sputterer (Denton Vacuum, USA) before each analysis. Gold deposition helped improve the image quality by creating a more conductive surface. The silica particles alone have low conductivity (typically on the order of 1.4 W/mK) which can result in electron charging on the surface from the electron beam. Thus, by applying a thin, inert, and conductive surface, the electrons do not build up to the same extent and better resolution can be obtained.

4.4.2 Nitrogen Adsorption/Desorption

Nitrogen adsorption measurements were used to measure the surface area and pore diameter of the mesoporous silica before and after functionalization. Nitrogen adsorption measurements were conducted by the Long Group at UC Berkeley on a Micrometrics ASAP2420 instrument. To perform these measurements, the dry solids (either bare mesoporous silica or functionalized mesoporous silcia) are first outgassed by heating them to 333 K while under vacuum for 12 h then heating to 393 K for 4 h. The temperature to which the sample is heated is determined by the maximum temperature the sample can withstand before potential degradation. After degassing,the sample mass is recorded (m_s). Nitrogen adsorption is then determined by measuring the relative pressure decrease of nitrogen gas as it is released onto the evacuated sample. As the gas adsorbs to the surface of the solid, the pressure of the primary container of gas will decrease and the pressure in the container with the solid will increase. Both physisorption and chemisorption processes can occur between the N_2(g) and the surface of the solid. Physisorption is adsorption based on weak intermolecular forces like hydrogen bonding and van der Waals interactions. Chemisorption involves the formation of a chemical bond between the two components, in this case, the N_2(g) and the surface. As no chemical bond is being formed, physisorption is the process occurring with these samples, and thus the surface area measurement used is the Brunauer-Emmett-Teller (BET) method. [83]

BET Surface Area

BET is based on van der Waals interactions, which occur between permanent dipoles, induced dipoles, and non-polar dispersion forces. The main assumption made with the BET equation is that during the interaction of the neutral gas molecules and the surface, no electrons are shared, but rather associate through weak intermolecular forces. [84] The BET equation (Equation 4.3)

Table 4.1: Nitrogen Adsorption Variables

Variable	Definition
P	pressure
P_0	saturation pressure of adsorbate
V	volume of adsorbate
V_m	volume of adsorbate required for a single monolayer
E_1	average heat of desorption, first monolayer
E_L	heat of liquefaction
R	gas constant
T	temperature
N_A	Avogadro's number
SA_{BET}	BET surface area
a	surface coverage of single adsorbate molecule
V_i	molar volume of an ideal gas
m_s	mass of solid after degassing

relates the measures nitrogen pressure to the volume it is occupying, which will in turn allow the calculation of surface area.

A straight line should be formed by plotting $\frac{1}{[V(P/P_0-1)]}$ against $\frac{P}{P_0}$, with a slope of $\frac{C-1}{V_mC}$ and an intercept of $\frac{1}{V_mC}$. From the slope and intercept, the value of V_m can be calculated and then used to calculate the BET surface area (Equation 4.3). Variables are defined in Table 4.1)

$$V=\frac{V_mCP}{(P_0-P)[1+(C-1)P/P_0]} \tag{4.3}$$

$$C=e^{(E_1-E_L)/RT} \tag{4.4}$$

$$SA_{BET}=aN\times\frac{V_m}{V_i} \tag{4.5}$$

The molar volume of an ideal gas (V_i), is 22414 cm^3/mol.The SA_{BET} is then divided by m_s to calculate the specific surface area of the material. Adsorption isotherms are generated by plotting the amount of gas adsorbed versus the relative pressure. Depending on the type of material, particularly the porosity, the isotherm will exhibit one of six characteristic shapes defined by IUPAC (Figure 4.4).

Type I isotherms are formed from the analysis of microporous solids with low external surface area. With these materials, the nitrogen adsorption is limited by the ability to diffuse through the micropore volume as opposed to the actual surface area.

Type II isotherms are the result of a material that can have unlimited adsorption as a result of having macropores or being non-porous.

Type III isotherms do not exhibit an inflection point, indicative of adsorbate-adsorbate interactions.

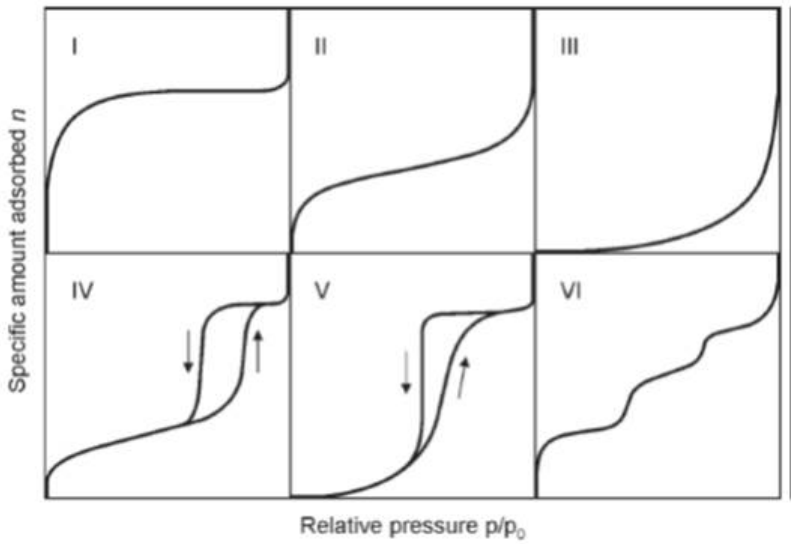

Figure 4.4: Nitrogen adsorption/desorption isotherm classifications (Klobes 2006 [1] adapted from Sing 1985, [2] © 1985 IUPAC)

Type IV isotherms are of main concern for this work. Type IV isotherms are characteristic of mesoporous materials and can exhibit four types of hysteresis (Figure 4.5). The hysteresis loop is caused by capillary condensation occuring in the mesopores.

The shape and closure points of the hysteresis loop can be indicative of the type of mesoporous material. Ideally, an ordered mesoporous material intended for organic modification for this work should be H1 in type. This is because a material with a H1 type hysteresis loop has a narrow pore size distribution. This is contrasted by an H2 type hysteresis loop, which is caused by materials with non-uniform pore size and shape. Both H3 and H4 type loops are from materials with slit-like pores, however with H4, the cause is slit-like micropores, whereas with H3, it is caused by aggregation of plate-like particles.

Type V isotherms are similar to Type III but for porous adsorbents.

Last, *Type VI* isotherms exhibit a step-like pattern caused by individual adsorption layers in multilayer adsorption to a non-porous surface.

Pore Diameter

The nitrogen adsorption measurements can be used to estimate the pore size distribution and volumes. For this work, the Barrett, Joyner, and Halenda (BJH) method was used to determine the pore diameter from the nitrogen adsorption. [85] The BJH method is based on the Kelvin equation, which comes with a number of assumptions: 1) cylindrical or slit-like pores, 2)the curvature of liquid meniscus in a pore is actually directly related to the pore diameter, 3) pores are rigid and of uniform shape, 4) only mesopores are present, not micro- or macropores.

When conducting pore diameter measurements, the software outputs pore width ranges, the average width within each range, and the corresponding incremental pore volume. The pore size distribution is depicted by plotting the derivative of the cumulative pore volume with respect to the logarithm (base 10) of the pore diameter versus the pore diameter. Ideally the pore size distribution will be narrow and centered around the intended pore diameter. Typically for the work in the project, 8 nm pore diameter was desired.

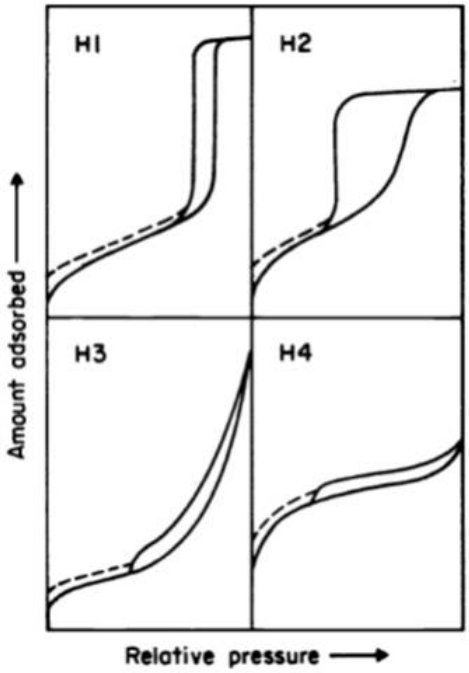

Figure 4.5: Nitrogen adsoprtion/desorption isotherm hysteresis loop characterization (Sing 1985, [2] © 1985 IUPAC)

There are limitations in both the BET and BJH methods for surface area and pore size determination, respectively. The BET calculation does not account for potential damage to the material from the high vacuum and temperature used during degassing. The vacuum could cause collapse of microstructures in the porous material. The temperatures required for full degassing of the solid could result in degradation of the material, especially when already functionalized with organic ligands. Thus, if the material is not completely degassed, the nitrogen uptake may be lower and thus make the surface area seem inadvertently low. In terms of determining the pore diameter, the BJH method tends to underestimate this value because of the inability to account for curvature of the pores. [86]

4.4.3 Thermogravimetric Analysis

Thermogravimetric analysis (TGA) is a method used to measure the extent of thermal degradation of a material. In the case of the organically-modified silica materials used in this work, it was used to estimate the ligand density on the surface of the material. To do this, a solid sample is heated under controlled atmosphere at a constant heating rate and the mass is recorded over time. From this, the mass loss as a function of temperature can be plotted.

The TGA measurements in this work were conducted by Ying-Jen Wanglee in the Katz Group at UC Berkeley. On a TA Instruments TGA 2950 with standard platinum crucibles, approximately 8 mg of sample were heated under 50/50 v/v Ar/O_2 flow. The temperature program consisted of 1) heating at 4 °C/min from room temperature to 120 °C, 2) holding at 120 °C for 45 min, and 3) heating at 10 °C/min to a final temperature of 800 °C.

There are a number of assumptions made with TGA, especially when it is not tandem with a mass spectrometer (TGA-MS). First, the decomposition of the materials must be predicted. For the TGA measurements presented in this work, full volatilization of the ligands has been assumed in the calculations of ligand density. In the case that the ligand does not completely volatilize, it could either remain attached to the surface of the solid, or it could decompose to non-combustible solids. In either case, if the ligand does not completely volatilize, then the estimate of ligand density will be low. For better ligand density estimates, a TGA-MS could be used and the actual volatilized mass fragments characterized.

4.4.4 Infrared Spectroscopy

Infrared (IR) spectroscopy is used to examine components of chemical systems that are active to photons with wavelengths in the infrared. While there are three regions of the infrared spectrum, near-, mid-, and far-, typically mid-infrared light is used in IR spectroscopy. Mid-infrared light is within the wavenumber range of 4000 to 400 cm^{-1}, where wavenumber is inverse wavelength. Chemical bond vibrations are most active to this energy of light, as well as some rotational motions. IR spectroscopy is used to probe the bonds in the OMMS materials by exciting bonds with infrared energy and collecting an absorbance or transmission spectrum. Different molecular bonds will absorb different energies depending on the type of bond and elements that are present. For an IR spectroscopy experiment, IR light is focused on a sample and the absorption or transmittance spectrum is recorded. Based on the energy of the absorbed light, information about the chemical bonds can be collected. Each chemical bond has unique bond energy and motions which can be assigned in the IR spectrum. A molecule can have more than one vibrational mode, and this can be determined by the number of atoms (N) and the linearity of the molecule. Linear molecules have 3N-5 and non-linear molecules have 3N-6 vibrational degrees of freedom. Possible modes of vibrational motion are symmetrical and asymmetrical stretching, and multiple bending modes including scissoring and twisting. Changes in the symmetric versus asymmetric components of a particular stretch can be indicative of changes in a bulk lattice structure, especially for materials like silica.

In order to study a sample with IR spectroscopy, the IR light must be able to pass through the sample. However, solids can be highly absorbing and thus must be prepared for measurement when using transmission IR spectroscopy. To do this, the solid can either be dissolved in solvent, suspended in nujol mull (mineral oil), or pressed into a KBr pellet with high clarity. This sample preparation can be particularly challenging, especially with solids that can aggregate like silica. Thus, an IR spectrometer equipped with attenuated total reflection (ATR) can be used, which avoids sample preparation.

ATR, or attenuated total reflection, is a useful technique as it allows samples to be measured directly without the requirement of a KBr pellet or nujol mull. ATR takes advantage of the formation of an evanescent wave as a result of total internal reflection of the infrared beam in the ATR crystal, made of optical grade material with a high refractive index. [82] Common materials for ATR crystals are Ge, diamond, and ZnSe. The evanescent wave that forms in the crystal can only travel about 0.5 to 2.0 μm into the sample, which means that the solid samples must be pressed against the crystal, eliminating air bubbles and void spaces.

The IR spectra collected for this work were done on the Long Group (UC Berkeley) IR spectrometer with ATR. The instrument was a Perkin-Elmer Spectrum 400 equipped with a GladiATR Single Reflection Attenuated Total Reflectance (ATR) module (Pike Technologies, USA) and a deuterated triglycine sulfate (DTGS) detector. Sixteen interferograms were acquired in the

450 to 3950 cm-1 spectral range with a resolution of 4 cm-1. Background spectra were collected without covering the ATR crystal. Background corrected spectra were normalized using the band showing maximum absorption.

4.4.5 Nuclear Magnetic Resonance Spectroscopy

Nuclear magnetic resonance (NMR) spectroscopy manipulates nuclear spins to study small changes in chemical environments for the nuclei of interest. For introductions to NMR spectroscopy and solid-state NMR spectroscopy, one should refer to Levitt, [87] Duer, [88] and MacKenzie and Smith, [89] respectively. For a nucleus with a non-zero azimuthal quantum number, M_J, M_J=2J+1. With no applied magnetic field, all M_J value with the same total angular momentum, J, are degenerate. However, when a static magnetic field is applied (B_0), these energy levels are split. This is effect is called Zeeman splitting. The energy difference between these split levels is dependent on B_0 and the gyromagnetic ratio of the nucleus (γ). This relationship is shown in Equation 4.6.

$$\Delta E = \gamma \hbar B_0 = \hbar \omega \tag{4.6}$$

The gyromagnetic ratio is the proportionality constant for the magnetic moment operator to the spin angular moment operator. This value is nucleus specific and is measured in rad $s^{-1}T^{-1}$. B_0 is measured in Tesla (T), and $\hbar$ is Planck's constant divided by 2π. From Equation 4.6, the Larmor frequency(ω_0) can be extracted.

$$\omega_0 = -\gamma B_0 \tag{4.7}$$

The Larmor frequency is the spin precession rate of a nucleus, typically measured in MHz or in rad s^{-1} when considering the angular frequency. Equation 4.7 is the angular representation, so to convert ω_0 to Hz, it must be divided by 2π. With respect to B_0 pointing along the positive z-axis, a positive value of γ indicates clockwise precession around B_0 when looking directly onto the positive z-axis and a negative value of γ indicates counterclockwise precession.

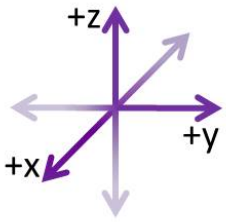

Figure 4.6: XYZ ordinates

In NMR spectroscopy, the frame of reference (lab or rotating) is important to keep in mind. In the lab frame, B_0 is along the z-axis and the nuclear spins precess around B_0 a their Larmor frequency. In the lab frame, the orientation of the magnetic moments for each spin can take on any number value in the xy-plane. In the rotating frame, however, the xy-plane rotates at the Larmor frequency. As the applied radiofrequency (rf) pulses (B_1) in an NMR experiment are applied at approximately the Larmor frequency, in the rotating frame they are static. Thus for simplicity, the rotating frame is commonly considered when discussing an NMR experiment.

If non-zero nuclear spins are placed in a static field B_0, they will have bulk magnetization along the z-axis, aligned with the field. In a single pulse (SP) experiment, rf pulses tuned to the

Larmor frequency of the nucleus of interest are applied. This causes the bulk magnetization to transfer to the xy plane along the y-axis (rf applied along the y-axis), and is called the transverse magnetization. Thus the spins now are rotating with an angular frequency ω_1 defined by equation 4.8.

$$\omega_1 = \gamma B_1 \tag{4.8}$$

To determine the length of time the rf pulse is applied, a number of spectra of a standard are collected with varying rf pulse lengths (measured in μs). The Fourier transforms of the free induction decay (FID) are plotted and the intensity as a function of rf-pulse length should be in the shape of a sinusoid. The point at which the curve crosses zero is called a 180 °, or π pulse, and correlates to transferring the spin population to the -z axis. Therefore, transferring the spins to the -y axis is done by applying a 90-degree or $\frac{\pi}{2}$ pulse (t_P). Mathematically, this is represented in equation 4.9.

$$\omega_1 t_P = \frac{\pi}{2} \tag{4.9}$$

After t_P, the rf-pulse stops and two simultaneous relaxations occur: 1) the precession of the transverse magnetization back to the direction of the applied field, along the z-axis, occurring with the relaxation time T_1 and 2)the magnetic moments of the individual spins dephase with the relaxation time T_2. As the transverse magnetization precesses, it induces an oscillating current as a function of time that is called the FID. The FID is plotted as intensity versus decay time. Taking the Fourier transform of the FID will result in a spectrum of intensity as a function of frequency in Hz. To convert between frequency and chemical shift (δ), the most common frame of reference used in analyzing NMR spectra, equation 4.10 is used.

$$\delta = \frac{\nu_{meas} - \nu_0}{\nu_0} \tag{4.10}$$

In equation 4.10, $\nu_{meas}$is the measured frequency and ν_0 is the Larmor frequency. The chemical shift describes slight deviations from the nuclei resonating at the Larmor frequency as a result of the electrons present in the system, which is why it is the measured frequency relative to the Larmor frequency. Depending on the shielding provided by those electrons, the chemical shift will vary, but only a very small amount which is why chemical shift is measured in parts per million (ppm). Experimentally, the chemical shift is measured with respect to a reference compound, such as tetramethylsilane (TMS) for ^{1}H, ^{13}C, and ^{29}Si.

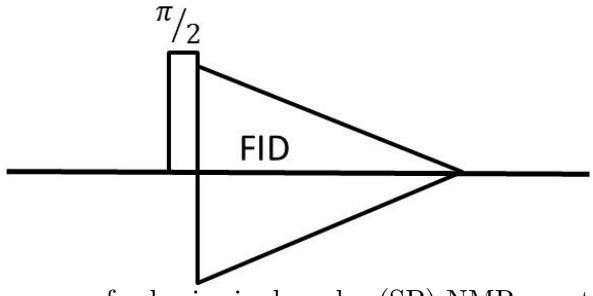

Figure 4.7: Pulse sequence for basic single pulse (SP) NMR spectroscopy experiment

Cross-Polarization/Magic Angle Spinning NMR Spectroscopy

Magic Angle Spinning As solid-state NMR spectroscopy was the focus of the NMR spectroscopy done in this work, this section is devoted to solid-state specific techniques. When measuring a solid sample by NMR spectroscopy, the peaks tend to be very broad as a result of dipole-dipole coupling. This is not the case in solution systems because in a liquid the molecular motions average out this coupling. The broadening of the peaks is due to the fixed orientation of chemical bonds in the system relative to B_0, and is called chemical shift anisotropy (CSA). The angle formed based on the bond orientation relative to B_0 is denoted θ. The dipole-dipole coupling of the dipole-dipole spin Hamiltonian can go to zero depending on θ and this dependence is indicated in equation 4.11.

$$3\cos^2\theta - 1 = 0 \tag{4.11}$$

Thus, for this equation to be met, θ equals $54.74\,^\circ$, and this angle is referred to as the magic angle. [90–92] Spinning a sample at this angle is called magic angle spinning (MAS), and is used to drive the dipole-dipole coupling to zero and thus increase the peak resolution in an NMR spectrum of a solid sample. MAS spinning is typically conducted at <15 kHz spinning rate, however spinning rates up to around 70 kHz can be achieved. Above 40 kHz is considered very fast-MAS and above 60 kHz is considered ultrafast-MAS. [93]

For the purposes of this discussion, very fast-MAS and ultrafast-MAS will be grouped together and referred to as fast-MAS. Fast-MAS requires special probes and the use of smaller rotors. In this work, a 1.3 mm rotor was used for fast-MAS experiments. There are a number of applications of fast-MAS NMR spectroscopy, including measuring compounds that contain paramagnetic species and high-sensitivity and high-resolution proton detection. Proton detection will be the focus of this discussion. As a result of the strong dipolar interactions between protons, even with MAS, linewidths can be quite broad for solid samples. This makes interpretation quite difficult. Thus, to better resolve proton resonances, the samples can be spun at fast-MAS rates which can be fast enough to better average out the dipole-dipole interactions. [94, 95] All ^{1}H solid-state NMR spectra collected in this work were done at fast-MAS rates of 50 kHz.

One of the main artifacts that can occur as a result of MAS are called spinning side bands. Spinning side bands occur in an NMR spectrum at frequency intervals from the isotropic chemical shift (or main peak) equal to that of the spinning frequency. Depending on the spinning rate relative to the CSA, the intensity of spinning side bands will vary. To minimize the presence of spinning side bands, the spinning rate needs to be greater than the frequency of the CSA. In many cases, spinning side bands will not interfere with the actual data analysis, however they can be mistaken for actual resonances or overlap with other resonances in the spectrum resulting in misinterpretation. By increasing the spinning rate or varying it throughout an experiment, side bands can be reduced. All solid-state NMR spectra collected in this work, except for the ^{1}H fast-MAS spectra previously mentioned were collected with an MAS rate of 10 kHz.

Cross-Polarization Cross-polarization (CP) is used in conjunction with MAS as a technique to measure nuclei with low abundance (e.g. ^{29}Si *or* ^{13}C) by transferring magnetization from nuclei with high abundance (e.g. ^{1}H). [96] The low abundance nuclei are denoted 'S′ and the highly abundant nuclei are denoted 'I′. The general pulse sequence is depicted in Figure 4.8. First a $\frac{\pi}{2}$ pulse is applied to the I channel, then an rf pulse is applied during which magnetization transfer by dipole coupling occurs from I to S. Magnetization transfer only occurs if the applied rf satisfies the Hartmann-Hahn

match condition (Equation 4.12). This match condition is equating their precession rates which, as shown in equation 4.7, depends on the field strength and the gyromagnetic ratio for the nuclei.

$$\gamma_{\mathrm{I}}\mathrm{B}_{1,\mathrm{I}} = \gamma_{\mathrm{S}}\mathrm{B}_{1,\mathrm{S}} \tag{4.12}$$

Experimentally, the match is determined by collecting a series of spectra at varying power levels which, when plotted against power level, will generate a bi-modal distribution. The maximum of the lower power distribution is taken as the match condition.

Another important parameter to a CP experiment is the duration of the spin locking pulse, referred to as the contact time (CT). The CT can be used to study the CP kinetics as the intensity of each resonance in a spectrum will respond to CTs differently. Typically, resonances that are more strongly influenced by the I spins will have maximum peak intensities at shorter CTs while those less strongly influenced by the I spins will have maximum peak intensities at longer CTs. The classic CP kinetics equation [97] describes the dependence of intensity on relaxation time for the I and S spins and CT (equation 4.13):

$$I(t) = I_0 \left(1 - \frac{T_{IS}}{T^I_{1,\rho}}\right)^{-1} \left[\exp\left(-\frac{CT}{T^I_{1,\rho}}\right) - \exp\left(-\frac{CT}{T_{IS}}\right)\right] \tag{4.13}$$

in which I_0 is the initial intensity and T_{IS} is the time constant for magnetization exchange. $\mathrm{T}_{1,\rho}{}^{\mathrm{S}}$ and $\mathrm{T}_{1,\rho}{}^{\mathrm{I}}$ are the time constants for magnetization decay for the 'S′ and 'I′ systems, respectively. In applying this equation it is important to note the assumptions: 1) the abundance of I spins is significantly greater than S spins, and 2) $\mathrm{T}_{1,\rho}{}^{\mathrm{S}}$ is much greater than $\mathrm{T}_{1,\rho}{}^{\mathrm{I}}$, T_{IS}. In the case of the CP experiments done in this work where the I spins were protons and the S spins were either ^{29}Si or ^{13}C, both of these conditions were met.

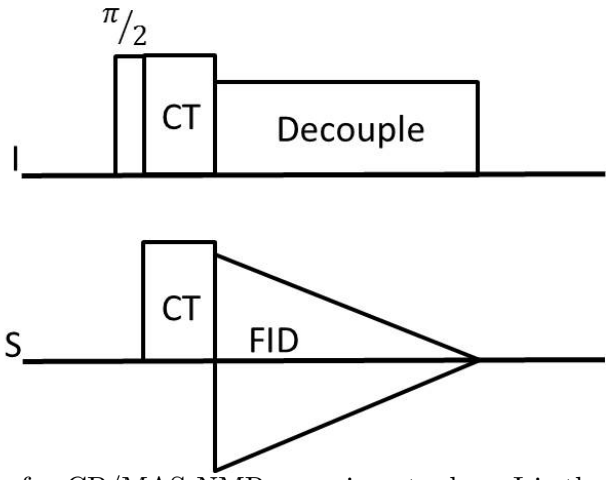

Figure 4.8: Pulse sequence for CP/MAS NMR experiment where I is the abundant nucleus (such as ^1H) and S is the less abundant nucleus (such as ^{13}C or ^{29}Si)

.

CP is not directly quantitative in the way that a SP experiment is because of the effect of CP kinetics on peak intensity. [97] As indicated in equation 4.13, the dependence on magnetization decay of the protons can also vary the intensity. In certain systems, this variation can be significant.

This is discussed further in the section on $T_{1,\rho}$ measurements. Experimentally, the selection of a CT can be a bit subjective depending on a number of factors associated with the system of interest. In general, however, a set of spectra are collected at various CTs. The CT that allows for the best signal-to-noise (S/N) of the resonances of interest should be selected.

All CP/MAS NMR spectra were collected on a 300 MHz (7.5 T) Tecmag Apollo using a Bruker HX CP/MAS probe configured for 4 mm (o.d.) rotors at Lawrence Livermore National Laboratory.

^{29}Si NMR Spectroscopy ^{29}Si is a spin-1/2 nucleus with a natural abundance of 4.7%. As a result of the very low γ of ^{29}Si and long relaxation time of these nuclei, SP experiments can take quite long to acquire. The long pulse delays in Si solids are due to minimal homonuclear dipolar coupling in such materials resulting in long relaxation times for the ^{29}Si nuclei. For instance, in silica, pulse delays on the order of two minutes are required. Thus, if trying to measure minor species in a ^{29}Si spectrum, a SP experiment may not be informative. This was the case with the organically-modified mesoporous silica (OMMS) materials. To enhance the signal from the surface species, particularly those ^{29}Si nuclei that were directly bound to the ligands, CP was used for the OMMS materials.

A ^{29}Si SP/MAS spectrum was collected at a spinning rate of 10 kHz with a pulse day of 120 s. ^{29}Si$\{^{1}$H$\}$ CP/MAS NMR spectra were collected on solid samples at a MAS rate of 10 kHz using a 3 ms continuous wave (CW) polarization transfer and 2 s pulse day. The operating frequencies for ^{29}Si and ^{1}H were 59.82 and 301.13 MHz, respectively, and spectra were referenced to TMS via an external kaolinite standard. In the ^{29}Si$\{^{1}$H$\}$ CP/MAS NMR spectra collected on the OMMS materials, two groups of peaks should be present if functionalized properly: Q and T peaks. The Q^n species are defined as $\mathrm{Si(OSi)_n(OH)_{4\text{-}n}}$ and the T^m species are similarly defined as $\mathrm{SiR(OSi)_m(OH)_{3\text{-}m}}$. The expected chemical shift ranges for these two groups of peaks are between $\delta_{Si} = 92$ and 112 ppm for Q peaks and $\delta_{Si} = 50$ and 70 ppm for T peaks. [89]

It is important to consider the effects of CP kinetics on a particular system especially when trying to compare spectra. In this work, ^{29}Si$\{^{1}$H$\}$ CP/MAS NMR spectra were compared to study relative ratios of the each of the T peaks. To compare spectra in such a way, the spectra must have been collected under identical conditions. Additionally, only peak ratios can be compared since the absolute values do not have physical meaning in CP NMR spectra. To confirm that the T peak ratios being compared between spectra were indeed indicative of changes to the material structure and not artifacts of changes in the proton environment, $T_{1,\rho}$ measurements were done.

The spin-lattice relaxation time constant along B_1 in the rotating frame is denoted $T_{1\rho,H}$. $T_{1\rho,H}$ is analogous to T_1 which is measured along B_0, but measured along B_1. To measure $T_{1\rho,H}$, a 90 ° pulse is applied, followed by a spin-locking pulse, and then the FID is collected. Multiple spectra are collected with increasing spin-locking time duration. The decrease in signal intensity as a function of the spin-locking time, τ, is then plotted and can be fit to the exponential equation 4.14.

$$I(\tau) = I_0 \exp(-\tau/T_{1,\rho}) \tag{4.14}$$

$T_{1\rho,H}$ variations can result in changes in relative peak intensities between samples. Reasons for $T_{1\rho,H}$variations would be significant changes in the proton populations in a given sample. In this work, $T_{1\rho,H}$ was measured for the pristine DGA-SBA and the acid-contacted DGA-SBA to ensure that the values were similar and that changes in T-peak intensity was due to solely to changes in the material rather than an artifact of the spin relaxation.

^{13}C NMR Spectroscopy ^{13}C is a spin-1/2 nucleus with a natural abundance of 1.108%. As a result of its very low γ, like ^{29}Si, CP/MAS is required to collect spectra with enough signal to discern anything about the molecular structure. ^{13}C{^{1}H} CP/MAS NMR spectra were collected at a spinning rate of 10 kHZ and used a 1 ms ramped amplitude polarization transfer on the ^{13}C channel, CW decoupling on the proton channel during acquisition, and a 2 s pulse delay. The operating frequency for ^{1}H was the same as in the ^{29}Si CP measurements and was 75.73 MHz for ^{13}C, referenced to TMS via an external glycine standard.

A ^{13}C{^{1}H} CP/MAS spectrum was collected on an organically-modified mesoporous silica sample with sorbed Eu. Europium has a unique effect on the spectrum because at room temperature it behaves as a paramagnet, due to van Vlack paramagnetism. A paramagnet, in contrast to a diamagnet, forms an induced magnetic field in the direction of B_0 when in an applied magnetic field, whereas a diamagnet forms an induced magnetic field in the opposite direction of B_0. The effect that this has on a spectrum is that the paramagnet can cause major changes in chemical shifts, broadening of peaks, and potentially the appearance that the peaks have actually disappeared. The nuclei that would be most strongly affected are those nearest to the paramagnetic species. In the case of the ^{13}C{^{1}H} CP/MAS spectrum of the Eu sample, the C atoms closest to the Eu atoms would be expected to show signs of a paramagnetic effect.

Double Quantum Correlation

The double quantum (DQ) correlation experiment allows associations between nearby protons to be probed by taking advantage of the homonuclear dipole-dipole coupling between them. The general homonuclear DQ-MAS pulse sequence consists of double-quantum coherence excitation, evolution over time t_1, then reconversion to the single-quantum (SQ) coherence, and its subsequent decay over t_2. [98] From this experiment, a plot of the DQ dimension versus the SQ dimension is generated. Consider resonances that occur at ω_1 and ω_2 in the SQ dimension. If there are multiple protons at ω_1, then a cross-peak at $2\omega_1$ will exist. These species generate the diagonal of the plot. An example of when this might occur is the two protons on a -CH_2 moiety. When the DQ coherence of spins from different populations (e.g.ω_1 and ω_2) are excited, they generate a resonance at the sum frequency $\omega_1 + \omega_2$ in the DQ dimension. Thus when reading a DQ plot, a correlation between protons at chemical shifts of ω_1 and ω_2 in the SQ dimension, should have correlations in the DQ dimension at $\omega_1 + \omega_2$. These correlations should only exist for protons in close association with one another (< 3.5 Å). ^{1}H spectra were all referenced to an external standard of hydroxylapatite by setting by setting the hydroxyl resonance to δ_H=0.2 ppm.

The DQ spectra were collected with a MAS rate of 50 kHz on a 600 MHz Avance III spectrometer equipped with a Bruker Very Fast MAS probe configured for 1.3 mm rotors. The ^{1}H DQ correlation experiment was collected using the Back to Back (BaBa) sequence. [99,100] A total of 128 spectra were collected in t_1 using the States-TPPI method [101] for 64 acquisitions each at a 20 s increment corresponding to a spectral width of 50 kHz in the indirect dimension.

Quadrupolar Nuclei

A quadrupolar nucleus has a quantum spin greater than 1/2, resulting in not only a magnetic dipole moment but also an electric quadrupole moment. [89] This electric quadrupole moment interacts with the electric field gradient (EFG) that is generated by the electrons in the system. In an NMR spectrum, the effect of interactions of the electric quadrupole moment with the EFG is loss of sensitivity and resolution.

In solid-state NMR, quadrupolar nuclei introduce frequency anisotropies that can cause peak broadening larger than the spectral width of the spectrometer in some cases. [89] Quadrupolar nuclei have more energy levels due to increased splitting that goes as 2n+1, where n is the spin. Thus, this splitting will be evident in the spectra, however, peak broadening and asymmetry can make discerning these resonances challenging. Additionally, the asymmetry and broadening can make determination of their isotropic chemical shift challenging.

To improve resolution in an NMR spectrum of a quadrupolar nucleus, a higher field can be used. At lower external magnetic field, second-order quadrupolar interactions can have increased broadening effects. Using a higher field can improve the resolution by minimizing those effects.

^{27}Al and ^{45}Sc SP/MAS Studies The two quadrupolar nuclei examined in this work were ^{27}Al and ^{45}Sc. Al and Sc were chosen because they both exist primarily in their trivalent oxidation state and have smaller ionic radii than the lanthanides studied. Al and Sc were also interesting because they could be probed directly via NMR spectroscopy as quadrupolar nuclei. ^{27}Al is spin- 5/2 and 100% naturally abundant.^{45}Sc is spin- 7/2 and is also 100% naturally abundant. Thus, based on their relative spin states, ^{27}Al and ^{45}Sc should have 6 and 8 split energy levels. The higher the spin, however, the more complex the NMR spectrum can appear and can result in very large broadening in solids. This was in fact observed with the ^{45}Sc spectra which were measured at two different magnetic field to better inform the fitting of the spectra.

^{27}Al and ^{45}Sc NMR were performed at operating frequencies of 78.46 and 73.15 MHz for ^{27}Al and ^{45}Sc, respectively. For aliquots of supernatant solutions, 14.5 and 15.5 μs pulse widths (corresponding to a 90 $^\circ$ tip angle) with recycle delays of 0.5 and 0.2 s were used for ^{27}Al and ^{45}Sc, respectively. To maintain consistency between measurements, the same volume (65 μL) of solution was added to the 4 mm (o.d.) ZrO_2 rotor for each sample. The integrated peak intensity for each sample was compared to that of a blank. The blank was prepared by combining 1 mL of the 70 mM metal nitrate stock solution with 11 mL of ultrapure water and acidifying to pH 3 with 0.1 M nitric acid. The ^{27}Al and ^{45}Sc single pulse MAS spectra of solid samples were performed with same probe head using a spinning rate of 10 kHz, and a pulse delay of 0.5 and 0.2 s for ^{27}Al and ^{45}Sc, respectively. Additionally, ^{45}Sc single pulse MAS spectra of the solid samples were collected on a 500 MHz Bruker Avance spectrometer with a DOTY probe. These were collected while spinning at 10 kHz with a pulse delay of 0.2 s. In each case, short 1 μs pulses were used to ensure that quantitative results could be obtained and correspond to 6.2 $^\circ$ and 5.8 $^\circ$ tip angles for ^{27}Al and ^{45}Sc, respectively. The ^{27}Al and ^{45}Sc spectra were referenced to their respective 70 mM metal nitrate stock solution (δ_{Al} = 0.0 ppm and δ_{Sc} = 0.0 ppm). All spectra were analyzed by fitting the peaks to pseudo-Voigt functions to obtain integrated intensity and the chemical shift.

Collection of ^{139}La, a spin-7/2 nucleus with 99.91% abundance, spectra were also attempted however no signal was detected using the 300 MHz spectrometer. While no rigorous troubleshooting was performed, the likely issue is that a higher field spectrometer was required to measure that nucleus due to the very large peak broadening as a result of the large spin state and quadrupole moment. Additionally, on that spectrometer the operating frequency for ^{139}La is 45.1 MHz which is at the low end of accessible frequencies for that probe. The range of the probe was also a problem when attempting to measure ^{89}Y (spin-1/2) which has an operating frequency on the 300 MHz spectrometer of 15.6 MHz. This frequency was completely inaccessible with that spectrometer and thus ^{89}Y could not be directly probed for this work via NMR spectroscopy.

TRAPDOR The Transfer of Population in Double Resonance (TRAPDOR) sequence was developed by Grey, et al, to probe interactions between quadrupole (S) and spin- 1/2 (I) nuclei by taking advantage of their heteronuclear dipolar coupling. [102, 103] In this experiment, two spectra of the spin- 1/2 nuclei are collected: 1)the spin echo 'control' and 2) the TRAPDOR. In the control experiment, the I nuclei are unmodified by the S nuclei, so they are decoupled. In the TRAPDOR spectrum, the I and S nuclei are coupled in the pulse sequence (Figure 4.9). If there are interactions between the I and S nuclei, the TRAPDOR spectrum should show a decrease in signal intensity for the I resonances associated with the S nuclei compared to the control spectrum.

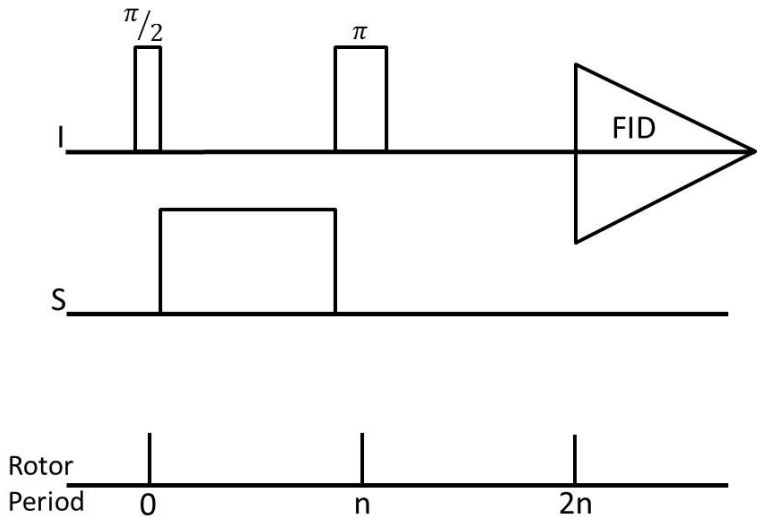

Figure 4.9: Pulse sequence for TRAPDOR NMR experiment where I is the spin-1/2 nucleus (such as ^{1}H) and S is the quadrupolar nucleus (such as ^{45}Sc). The sequence is rotor synchronized. The control experiment for S is not presented, as S is not irradiated for this measurement.

In this work, TRAPDOR was used on an organically modified silica material with sorbed scandium. Thus the quadrupolar nucleus, S, was ^{45}Sc and the spin-1/2 nucleus, I, was ^{1}H. The TRAPDOR spectra were collected on the same spectrometer and probe with the same MAS rate as was used for the DQ experiment. The ^{1}H{^{45}Sc} TRAPDOR experiment was collected as a set of two spectra where a spin-echo control spectrum (S_0) was collected in the absence of ^{45}Sc irradiation, and a TRAPDOR spectrum (S) was collected where the ^{45}Sc channel was irradiated with a 100 kHz dephasing pulse for 16 acquisitions each and a 10 s pulse delay using a 4.6 ms dephasing period (230 rotor cycles).

4.5 Chromatography

For chromatography experiments that did not use pre-packed columns, the resin material was first mixed with an appropriate acid solution for conditioning and allowed to wet until the particles sunk to the bottom of the mixture. A small amount of glass wool was added to the bottom of the column prior to slowly filling with the resin slurry using either air or argon flow and topping with a small amount of glass wool to keep the resin in place. Once packed, the column was not allowed to dry at all to prevent the formation of channels. Pre-packed DGA cartridges

were conditioned by flushing with 3 M HNO_3 and allowing to sit capped with parafilm with this same matrix. All resin beds were then rinsed with approximately 10 column volumes of solution that was the same matrix as the loading solution. The solution containing the metals of interest (loading solution) was added to the resin bed in as small a volume as possible to minimize band broadening. When eluting, eluent was slowly added to avoid coating the reservoir with metal at the top of the column. Pressure was applied using either air or argon flow, or for the cartridges, syringe pressure.

4.6 Inductively-Coupled Plasma Mass Spectrometry/ Inductively-Coupled Plasma Optical Emission Spectroscopy

Inductively coupled plasma- optical emission spectroscopy (ICP-OES) and inductively coupled plasma-mass spectrometry (ICP-MS) are two similar instruments that were used for the measurement of stable metals including La, Lu, Y, and Nd. These instruments have two components, one for ionization and one for detection. In both instruments, inductively coupled plasma is used for ionization. ICP is considered one of the best ionization techniques for low concentration metal samples due to its high efficiency. In ICP, the sample is taken up through a straw and nebulized into the ICP torch. The torch is a plasma that ranges in temperature at different points in the flame. When the metal ions enter the plasma, they are heated to very high temperatures at which point their matrix elements are burned off and they become ionized. These ions then travel to the detector. Depending on how the torch is oriented relative to the detector the limit of detection is different. For high concentration samples, the detector is oriented radially relative to the torch which allows for it to only collect a portion of the signal, thus preventing saturation of the detector. For lower concentration samples, the detector sits in an axial position relative to the torch which allows for the collection of a larger percentage of the overall signal. [82]

In ICP-OES, the detector measures the atomic emission of the metals. Each metal emits at characteristic wavelengths. The output is in intensity versus wavelength allowing the total concentration of metal to be determined. Potential detector interferences occur when multiple metals in a single sample emit photons of the same wavelength. A way to avoid this issue is to find wavelengths that are unique to each metal in the sample, even if they are not the most intense emissions. The ICP-OES used for this work was a Perkin Elmer Optima 7000 DV. Its sensitivity varied based on the emission intensity for each metal, but typical was on the order of ppb. In ICP-MS, a mass spectrometer is the detector. The MS used for this work was a quadrupole-MS. A quadrupole is a set of 4 poles that are set at alternating positive and negative potentials. Based on the electric and magnetic field generated by the quadrupole, the ions are separated based on their mass divided by their charge. The MS outputs signal versus mass/charge ratio. Each ion should have a distinct mass-to-charge ratio and can thus be differentiated. Potential interferences occur when other ions have the same mass/charge or when the ions are compounds that can form from the flow gas. Thus, all potential interfering ions must be identified prior to determining the metal concentration. The ICP-MS used for this work was a Perkin Elmer Elan DRC II and its limits of detection were on the order of ppt.

For ICP-AOES and ICP-MS, standards were made for the metals of interest to create a calibration curve. They were typically made in the range of 0.5 ppb to 1 ppm in metal concentration. Additionally, for the ICP-MS measurements, a Ho internal standard was added to each sample and each standard. Samples were diluted such that the metal concentration was expected to be within the range of the calibration curve. HNO_3 was adjusted in each sample such that they were in a

2% HNO_3 matrix. All sample and standard preparation was done by mass. Standards were run on either the ICP-MS or ICP-OES prior to the samples to ensure that a suitable calibration curve was obtained.

4.7 Nuclear Counting Methods

4.7.1 Liquid Scintillation Counting

Liquid scintillation counting (LSC) is a nuclear counting technique commonly used in hospitals to measure beta emitters used for medical tests. LSC can also be used to measure alpha emitters. It is typically considered 100% efficient for alpha particle detection. To prepare a sample for detection in an LSC, an aliquot of the desired solution must be added to liquid scintillation cocktail. Liquid scintillation cocktail is an organic mixture that contains a number of components that ultimately allow for the conversion of alpha or beta-particle to photon emission that is within the detectable range of a photomultiplier tube (PMT). The core components of the cocktail are solvent, scintillator or fluor, and wave shifters. The solvent is typically an aromatic molecule. The scintillator or fluor, is a molecule that upon excitation from the solvent emits a photon. The emitted photons often do not have a wavelength that corresponds to the ideal detection range of the photomultiplier tubes. Thus, a wave shifter is present in the cocktail which is optimized to absorb at the wavelength of the emitted photons from the fluor and then subsequently emit a photon at a different wavelength in the detectable range of the PMTs.

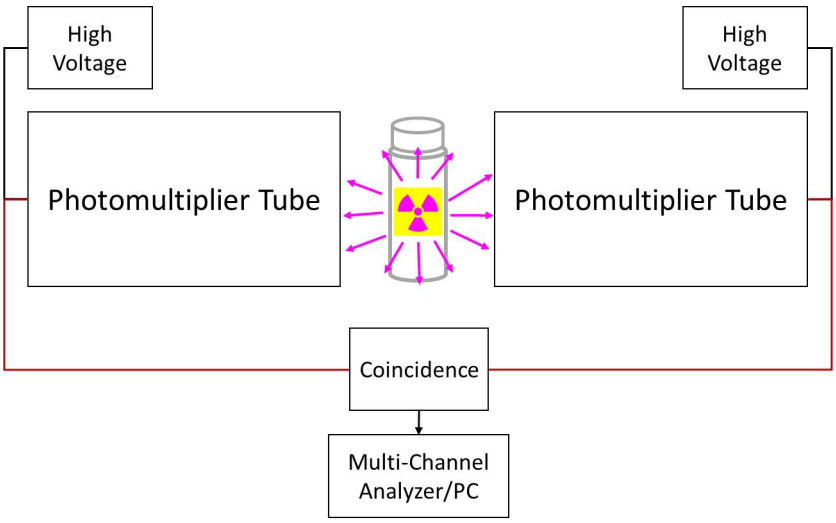

Figure 4.10: Schematic of a liquid scintillation counter

A schematic of an LSC is presented in Figure 4.10. The samples are double-contained to control the radiological hazard. The inner vial contains 5 mL of Ecolume^{TM} liquid scintillation cocktail and then an aliquot of the sample of interest typically in a volume of less than 100 μL. The inner vial, prepared in a glove box or hood, is then passed out into an outer 20 mL polyethylene terephthalate (PET) scintillation vial. The LSC vials sit in racks in the counter and when it is time for the sample to count, it is mechanically picked up into a shielded counting area. This counting area contains two photomultiplier tubes at 180 ° to one another. The purpose of this is to measure the coincidence of the emitted photons. When the radioactive species in the sample emits an alpha or beta particle, that particle interacts with the solvent to excite those molecules. Those molecules

then de-excite by passing their energy to the fluor molecules. The fluor molecules emit photons that then interact with the waveshifters to emit photons that are then detected by the PMTs.

There are a few things that can lead to inaccurate measurements via LSC if they are not accounted for, primarily chemical and color quenching. Quenching occurs when the emitted radiative particles or photons can de-excite via alternate mechanisms besides the aforementioned path. Chemical quenching happens when a reagent present in the sample acts as an alternative mode of interaction with either the alpha or beta particles themselves, or the energy from the solvent, fluors, or even wave shifters. Color quenching occurs when the sample is colored in the visible range which can result in absorption of the photons emitted from either the fluors or waveshifters. This would result in an anomalously low measured radioactivity. Chemical and color quenching are rarely issues when detecting alpha particles due to their very high average particle energy relative to that of beta particles.

To differentiate between alpha and beta particles in LSC, pulse shape analysis (PSA) is used. [104, 105] While energy discrimination alone can be employed, issues can occur when high energy betas are detected as alpha particles. In LSC, when an alpha or beta particle is detected, there are two components to the pulse: 1) prompt and 2) delayed. Depending on the particle type, the relative duration of each of these components varies and can thus be binned based on the pulse duration. For beta emissions, the prompt component lasts about 2-8 ns, and the delayed can last up to 900 ns. [106] Alpha particles, however, have a longer delayed component that can allow the two types of particles to be differentiated. Additionally, PSA can be employed to discriminate between actual signal as opposed to background from cosmogenic sources interacting with the vials, however it is far more effective for alpha discrimination.

All LSC was done on a Wallac 1414 liquid scintillation counter utilizing PSA. Samples were prepared by adding an aliquot of the solution to be analyzed to 5 mL of Ecolume^{TM} LSC cocktail. Aliquots were typically in the range of 5 to 50 μL, but were most commonly 25 μL. The ecolume and solution mixture was contained in a 5 mL inner vial that was enclosed in a secondary 20 mL polypropylene LSC vial. Samples were shaken vigorously prior to counting. Blanks that contained 5 mL of ecolume and an equal volume compared to the samples of the background matrix for the samples (e.g. HNO_3 or NaCl) with no added radioactivity were measured as well. Sample were typically counted for 5 minutes, however, longer count times were used as required for improved counting statistics. Determination of moles (n) of the nuclide of interest were determined from the counts per minute (cpm) output from the liquid scintillation counter using equation 4.15.

$$n = \frac{cpm}{60 N_A \varepsilon \lambda} \tag{4.15}$$

$$\lambda = \frac{ln(2)}{t_{1/2}} \tag{4.16}$$

where λ is the decay constant (equation 4.16) for the radionuclide of interest, N_A is Avogadro's numbers, and ε is detection efficiency. When counting alpha activity with LSC, the efficiency is typically approximated as 100%. [104]

4.7.2 Gamma Spectroscopy

Radioactive nuclei have numerous nuclear energy levels and transitions between these levels often results in the emission of a photon in the energy range of about 10 keV to 10 MeV. Each radionuclide will have a distinct gamma ray energy spectrum where the peaks correspond to

discrete energy level transitions. Knoll provides a detailed explanations of gamma spectroscopy and the various types of gamma detectors. [104]

Gamma rays are detected based on their interactions with detector materials. Gamma rays can interact with matter via three main mechanisms. These three mechanisms are the photoelectric effect, Compton scattering, and pair production. These interaction are dependent on the energy of the incoming gamma ray, however they can coexist in a single spectrum.

The photoelectric effect is the deposition of the full energy of the incoming gamma ray into the detector material. Thus, the peak that results from this interaction for a given gamma ray is referred to as the photopeak. When this occurs, the deposition of the gamma ray energy causes an electron from the detector material to be ejected. The ejected electron travels with kinetic energy (E_{kin}) equal to the energy of the incoming gamma ray (E_{γ}) minus the binding energy (B_e) of that electron (equation 4.17).

$$E_{kin} = E_{\gamma} - B_e \tag{4.17}$$

If, however, not all of the energy from the incoming gamma ray is deposited in the detector and only some of it is transferred, the effect known as Compton scattering will occur. When the gamma ray elastically scatters off of an electron, it transfers a portion of its energy to the electron. After collision, the recoil electron and scattered photon proceed in different directions such that momentum is conserved in the system. The energy loss to the electron during scattering is described by the Compton scattering equation (equation 4.18).

$$\lambda' - \lambda = \frac{h}{m_e c}(1 - \cos\theta) \tag{4.18}$$

where λ and λ' the wavelengths of the photon initially and after scattering, h is Planck's constant, m_e is the rest mass of an electron, c is the speed of light, and θ is the scattering angle of the photon. Based on the scattering angle of the photon, the wavelength shift ($\lambda' - \lambda$) can vary between 0 and $\frac{h}{m_e c}$, which is known as the Compton wavelength. The wavelength shift maximum occurs when there θ equals 180 ° and thus is when the photon directly backscatters off of the electron. This maximum value is denoted E_{max} and is defined by:

$$E_{max} = \frac{2E^2}{m_e c^2 + 2E} \tag{4.19}$$

where E is the energy of the incoming gamma ray. As this is the maximum energy that can be transferred, an edge occurs in the spectrum called the Compton edge. As a result of the variety of scattering angles, photons with a range of energies are scattered and can subsequently interact with the detector material. The range of potential energies results in a continuum that exists at energies below that of the Compton edge. The Compton continuum can interfere with the quantification of additional photopeaks that occur on top of the continuum.

When a gamma ray has sufficient energy, it can interact with the detector material to produce an electron/positron pair in process called pair production. To produce an electron/positron pair, the incoming gamma ray must have at least the energy of $2m_e$. As there are an abundance of electrons in any given system, the positron will annihilate quickly, resulting in the release of two 511 keV gamma rays at 180 ° to one another. Thus, any time gamma rays with energies greater than or equal to 1022 keV are measured, one could expect to find a peak at 511 keV. These 511 keV gamma rays caused by electron/positron annihilation can either both be detected, one can escape

the detector, or both can escape the detector. When a single 511 keV peak escapes, a single escape peak will appear at the energy of the photopeak minus 511 keV, and similarly when both escape, a double escape peak will appear at the energy of the photopeak minus 1022 keV. In addition to the peaks present from the nuclide of interest and the subsequent backscatter and escape peaks, additional peaks may occur from the background. When quantifying a nuclide based on its gamma spectrum, the photopeak is used.

Gamma Ray Detectors There are a number of different types of gamma ray spectrometers, but they can be grouped into two main categories: 1) scintillation and 2) semiconductor-based detectors. When considering which detector to choose for an application, the importance of efficiency and resolution must be weighted as it is difficult to have both a highly efficient and high resolution detector. Efficiency is mainly dependent on the detector crystal size and atomic number (Z). The crystal size is important because with a larger crystal there are a greater number of chances of the gamma ray interacting with the detector material. The atomic number of the crystal material influence the efficiency because the probability of a gamma ray interacting with matter scales with Z. Efficiency also scales with energy because very high energy gamma rays are less likely to interact with the detector material. Resolution is primarily dependent upon the type of detector, scintillator or semiconductor and the particular properties of those crystal materials.

The most common scintillation based detectors for gamma spectroscopy are NaI detectors. When a gamma ray interacts with a NaI crystal, the NaI scintillates, emitting photons which are collected and multiplied by a photomultiplier tube. NaI detectors are among the more inexpensive and robust detector options as they do not need to be held at cryogenic temperatures. Additionally, they are among the most efficient gamma ray detectors due to the ability to make large NaI crystals and the high Z of iodine (Z=53). However, the main disadvantage with these detectors is their poor energy resolution ($\sim$ 7% for 661 keV gamma ray). For improved resolution, a semiconductor detector, such as high-purity germanium (HPGe), is typically employed.

In a semiconductor detector, the main detector crystal is a semiconductor material. In a semiconductor, the gap between the valence band and the conduction band is smaller than in an insulator but larger than in a conductor. For Ge, the band gap is 0.7 eV. Because of the smaller band gap in a semiconductor compared to an insulator, electrons can be excited to the conduction band and subsequently produce an equal number of holes in the the valence band. In a semiconductor, electron rich (n-type) and electron poor (p-type) regions build up. The junction of the p and n regions is where the positive and negative charges cancel and is thus called the depletion region. The depletion region is the active area of the detector and thus should be maximized for better efficiency. By applying a potential across the semiconductor, the width of the depletion region increases. When a gamma ray or X-ray passes through the depletion region, an electron/hole pair is generated. Electrons are attracted to the positively charged side (p-type) and holes to the negatively charged side of the junction (n-type), respectively. The applied bias sweeps these charges from the crystal to the pre-amplifier. The energy of the incoming ionizing radiation is determined based on the amplitude of the pulse registered in the pre-amplifier. The charges collected are proportional to the energy deposited in the detector from the incoming photon, and thus the pulse amplitude depends on this as well.

As a result of the small band gap in Ge, the Ge crystal must always be held near 77 K (the temperature of liquid nitrogen) when bias is applied. This is because thermal generation of electron/hole pairs can be detected as erroneous signals. Additionally, formation of charge carriers as a result of temperature (leakage current), can permanently destroy the resolution of

the detector. A HPGe detector has very high resolution (approximately 0.2% at 661 keV) which makes it a standard in nuclear counting equipment, especially when measuring samples that contain multiple gamma ray peaks. However, growing HPGe crystals is challenging and expensive and thus only smaller Ge crystals are in a standard HPGe detector. The problem with the small Ge crystal is that there is less detector material for a gamma ray to interact with, which becomes especially problematic with high energy gamma rays because they are less likely to lose energy to the Ge crystal. Compared to NaI, Ge is also lower in Z (Z=32), which decreases the probability of gamma ray interaction. As a result of these two factors, the efficiency of these detectors is much lower than in NaI detectors (typically less than 5% in standard HPGe detectors compared to much greater than 10% efficient in NaI detectors).

For the work presented here, HPGe detectors were used to quantify radionuclides including ^{152}Eu, ^{241}Am, and ^{243}Am. The HPGe detectors used for Eu measurements were standard energy range of about 40 keV to 2000 keV. For the Am samples, the low-energy HPGe detectors with a range of about 10 keV to 100 keV were used. One of the main differences with a lower energy HPGe detector is the detector window. For lower energy, a beryllium window is used. Additionally, because of high background typically encountered in the low energy regime, additionally shielding is used. To calculate the moles of the nuclide of interest, a similar equation to equation 4.15 used for LSC is followed (4.20).

$$n = \frac{cps}{fN_A\varepsilon\lambda} \tag{4.20}$$

where f is the fractional intensity of the peak being analyzed, and ε is the detector efficiency. This equation does not account for geometric efficiency, which can significantly impact gamma spectra. The reason it is not accounted for in this equation is because it was controlled for by maintaining identical detector geometry for all samples. If, however, the geometry of the sample relative to the detector varies, the geometric efficiency must be thoroughly characterized.

4.7.3 Alpha Spectroscopy

Alpha spectrometers typically use a silicon surface barrier diode detector. In this detector, the silicon semiconductor (band gap of 1.1 eV) is doped to form a p-n junction and coated with gold as an electrical contact. A reverse bias is applied to the p-n junction which causes the formation of a depletion region of a few millimeters, the active volume of the detector. As alpha particles cannot travel far in air, the detectors are held under vacuum to maximize the detection efficiency. In addition to increasing efficiency, measuring the alpha spectrum under vacuum improves resolution by minimizing pathways for the alpha particles to lose energy on the way to the detector.

To measure an alpha spectrum, an alpha plate of the desired sample is prepared. An ideal alpha plate is one where the sample is an infinitely thin point source. To get as close to this scenario as possible, small volumes of low ionic strength solutions with low acid content are used. Two different preparation methods of alpha plates were used for the work presented in this thesis. The first is an evaporation method in which a platinum plate is cleaned with acetone and then heated on a hot plate prior to pipetting a small volume (2-10 μL) of the sample solution onto the center of the plate. The solution is allowed to evaporate and then heated on the hot plate for an additional few minutes to burn off other constituents in the sample or quickly drawn through the flame of a Bunsen burner. The other preparation method is electrodeposition which was done on stainless steel plates. [107] For this, the sample was dissolved in 5% $NaHSO_4$ and evaporated to dryness. Water was then added to slowly dissolve the $NaHSO_4$ solid. Once the solid

was dissolved, 15% Na_2SO_4 was added and the mixture was poured into the electrodeposition cell. In the electrodeposition cell, a stainless steel plate was the cathode and a Pt wire acted as the anode. The deposition was conducted in constant current mode (1.0 A) for approximately 30 min or until the voltage plateaued. The reaction was neutralized with KOH and deposition continued for another couple minutes prior to pouring off the solution and removing the plate. The plate was rinsed with NH_4OH, then ethanol, and last acetone before drying on a hot plate.

4.8 X-ray based techniques

X-ray based spectroscopic methods are based on photons with X-ray energies impinging upon a sample and the resulting emitted or transmitted photons being measured. The X-ray techniques that will be discussed here are X-ray absorption spectroscopy (XAS) and X-ray fluorescence (XRF) spectroscopy. A thorough discussion of the theory and experimental results of XAS are in the dissertation of Yung-Jin Hu, [73] but will be more briefly summarized here. The XAS review articles by Yano and Yachandra [108] and Lee, et al, [109] also provide more detailed pictures of these techniques.

4.8.1 X-ray absorption spectroscopy

To do XAS studies, the X-ray source is usually a synchrotron radiation lightsource because of the requirement of a high intensity beam with narrow energy dispersion . XAS is based on each element having unique absorption characteristics that are determined by their electronic structure and physical configuration. An increase in absorption, or edge, occurs when the incoming photons have energies necessary to excite core-level electrons to either the lowest unoccupied molecular orbital (LUMO) or, in the case of a photoelectron, into the continuum. The name of the edge is defined by the core level from which the electon is excited. Thus, the K, L, and M edges are from 1s, 2(s or p), 3(s, p, or d) orbitals, respectively. There are three L edges, L_1, L_2, and L_3, that correspond to the 2s, $2\,p_{1/2}$, and $2\,p_{3/2}$ orbital electrons, respectively.

During an XAS experiment, the X-rays are passed through a monochromater before striking the sample. When the X-ray strikes the sample, if it has enough energy, it will excite a core level electron into the LUMO or the continuum. When this occurs, an electron from a higher energy level will drop into the core hole, resulting in the emission of a photon, or fluorescence. There are multiple ways to measure the interactions of the incoming X-rays with the sample, but two of the most common are monitoring the X-ray transmittance or the fluorescence from the ejected photons. There are typically three ionization detectors in an XAS setup, located between the monochromator and the sample (I_0), directly after the sample (I_1), and between a reference sample and the beamstop (I_2). For transmittance measurements, the ratio of I_1 to I_0 is measured and absorbance is calculated by a simple Beer's law relationship (Equation 4.21, where μ is the absorption coefficient and x is the sample thickness.

$$\mu x = \ln\left(\frac{I_0}{I_1}\right) \tag{4.21}$$

An X-ray absorption spectrum is composed of two main regions: 1) X-ray absorption near-edge structure (XANES), and 2) extended X-ray absorption fine structure (EXAFS). Both of these regions are contained within a single XAS spectrum however exist at different energies with respect to the edge of interest. The XANES region is between about 5 eV below and 150

eV above the absorption edge. The XANES region provides information about the formal charge of the element of interest and the general coordination geometry. This can be particularly useful when examining metals with multiple possible oxidation states that can readily reduce or oxidize. The EXAFS region extends from about 20 eV to 2000 eV above the edge. This region can be more difficult to interpret correctly, but also includes information about interatomic distances and species. Additionally in the EXAFS region, scattering between two of the same target elements can be observed which can indicate formation of localized clusters of the element of interest.

The XAS experiments presented in this work were all performed at either beamline (BL) 2-3 or 11-2 at the Stanford Synchrotron Radiation Lightsource which is part of the SLAC National Accelerator Laboratory. BL 2-3 is a micro-focus beamline, which means that there are additional optics used to shrink the beam spot. For this work, the beam spots were typically on the order of 2 x 2 μm^2. This compares to BL 11-2, which is intended for bulk analysis, where the area of sample analyzed was determined by the slit size set to match a uniform area of the sample. On the micro-focus beamline, the target area was determined based on the microfluorescence map generated of the sample. A sample spot with a high concentration of the metal of interest (either La, Eu, or Lu) was selected and then X-ray absorption spectra were collected at that location. On 11-2, the Am samples were measured at cryogenic temperatures (approximately 30 K) to minimize any beam induced chemistry on the samples.

Data analysis of XAS spectra can be complicated especially when determining the appropriate fit. An approximation for E_0 can be taken as the energy associated with the absorption at halfway up the edge step. Another method, and the one used in this work, is to set E_0 to the energy associated with the maximum of the derivative of the energy spectrum. The EXAFS oscillations (χ(E)) are the difference in the measured XAS absorption ($\mu(E)$) and the background ($\mu_0(E)$), described in equation 4.22.

$$\chi(\mathrm{E}) = \frac{\mu(E) - \mu_0(E)}{\mu_0(E)} \tag{4.22}$$

During data analysis, normalizing the data such that the absorption edge is set to one, is done after the background from the pre-edge region is subtracted. After this, the post-edge region background must be subtracted to leave behind only the EXAFS oscillations. There are three different spaces in which EXAFS spectra are typically viewed: 1) energy space in units of eV, 2) k-space in units of $Å^{-1}$, and 3) R-space which is the Fourier transform of the k-space with units of Å. In converting from energy space to k-space, the perspective of considering the photoelectron energy is changed to now looking at the wavevector of the ejected photoelectron (Equation 4.23).

$$\mathrm{k} = \sqrt{\frac{2m_e}{\hbar^2}(E - E_0)} \approx \sqrt{0.2628(E - E_0)} \tag{4.23}$$

In equation 4.23, E and E_0 are the energy of the outgoing photoelectron and the ionization energy of the core-level electron being ejected, respectively, and m_e is the rest mass of an electron. The second part of equation 4.23 simplifies the constants and converts them to units such that k is in inverse angstroms if energies are in eV, which is a more appropriate unit for the analysis scale. To convert to r-space, the Fourier transform of the EXAFS spectrum in k-space is taken. To perform data analysis of the XAS spectra, the software packages SIXPACK, [110] ATHENA, [111] and ARTEMIS [111] were used. SIXPACK was used for pre-processing of XAS spectra and deadtime corrections. ATHENA was used for the background subtraction, normalization, and overall data reduction. ARTEMIS was used to fit models using FEFF9 [112–114] to the the reduced data

from ATHENA. While full fitting of the EXAFS spectra has not been performed yet on the data presented in this document, analysis of the number of nearby oxygen atoms and the metal-oxygen distances were approximated.

4.8.2 micro-X-ray Fluorescence Spectroscopy

The micro-X-ray fluorescence (μXRF) spectroscopy was done on BL 2-3 at SSRL. The setup for BL 2-3 is similar to that of BL 11-2, except on BL 2-3, there are additional focusing mirrors after the monochromator to narrow the beam spot. The energy range for BL 2-3 is between about 5,000 and 23,000 eV allowing us to measure the L_{III} edge of La, Eu, and Lu. For these measurements, a 4-element VORTEX Si-drift XRF detector was used. The absorption edge energies for La, Eu, Lu, and Cl are presented in the following table.

μXRF spectroscopy mapping was used for six diglycolamide-modified mesoporous silica samples. The six samples were two each of La, Eu, and Lu bound to the DGA-SBA in pH 2 HCl, where one of the two was in 3 M Cl^- (controlled with NaCl), and the other had no added NaCl. Similar to the batch sorption experiments, the DGA-SBA solid was pre-equilibrated with HCl/NaCl solution of interest for 14-17 h prior to addition of the lanthanide of interest. After 24 h of metal-DGA-SBA contact, the supernatant was removed and the solid was allowed to dry. To mount the samples for measurement at the beamline, the solid was pressed between two pieces of thin Kapton tape, which did not contain X-ray absorbing impurities. Thicker Kapton was found to contain more impurities which absorbed the Cl fluorescence and thus completely quenched the signal.

X-ray fluorescence is analyzed as a function of energy. The fluorescence lines on the spectra correlate to the energies of the emitted photons and can be binned such that certain regions of interest (ROIs) are selected. For a given element, a single ROI can be selected and used to generate an XRF map. The XRF map is a map of the intensity of that particular ROI for many XRF spectra generated by rastering the beam over the sample. The elemental XRF maps were analyzed using Sam's Microprobe Analysis Kit (SMAK). [115] Using SMAK, background and dead time corrections were performed, as well as normalization of the data to time and monochromator settings. Using this program, multi-element plots were generated which allows for visualization of elemental correlation. The work here was focused on correlations between chloride and the lanthanide elements of interest: La, Eu, and Lu.

4.9 Fluorescence spectroscopy

Fluorescence spectroscopy was utilized to probe the coordination of the highly fluorescent Eu(III) ions. Fluorescence spectroscopy relies upon the measurement of fluorescence emission both at a single time point as a function of wavelength and at a single wavelength as a function of time for a fluorescent compound or element. Fluorescence occurs when an electron is excited to a singlet state from the ground state, and due to it remaining paired to another electron in the ground state, is able to de-excite by a spin-allowed emission of a photon. Typically fluorescence lifetimes are on the order of 10 ns. The difference between phosphorescence and fluorescence, is that in phosphorescence the excited electron is in a triplet state and oriented in the same direction as the ground state electron causing the emission of a photon to deexcite to be a forbidden transition. [116]

The average amount of time an element or molecule spends in the excited state is defined as the lifetime of that state. When a molecule de-excites, it can do so through radiative and

non-radiative means. The natural lifetime (τ_{n}) is the inverse of the radiative decay rate (Γ) and exists only when there is no non-radiative decay (equation 4.24). However, when non-radiative decay occurs, the observed lifetime (τ) is related to the natural lifetime by the relative quantities of radiative and non-radiative decay ($\mathrm{k_{nr}}$), equation 4.26.

$$\tau_{\mathrm{n}} = \frac{1}{\Gamma} \tag{4.24}$$

$$\tau = \frac{1}{\Gamma + \mathrm{k_{nr}}} \tag{4.25}$$

$$\tau_{\mathrm{n}} = \tau \times \left(1 + \frac{\mathrm{k_{nr}}}{\Gamma}\right) \tag{4.26}$$

For the Eu fluorescence under consideration here, the most significant route of non-radiative relaxation is through energy loss to waters in the inner coordination sphere of the metal. The observed decay constant (k) as a function of waters in the inner coordination sphere was measured by Horrocks and Sudnick. [117] Equation 4.27 related these two parameters based on his experiments.

$$\mathrm{n_{H2O}} = 1.07k - 0.62 \tag{4.27}$$

The observed decay constant can be determined from the measured lifetimes. The fluorescence lifetime of a species should decay as a first-order exponential function. However, the observed lifetime may not be well described by such a function if there are multiple species present. In this case, the lifetime decay curve must be fit by multiple exponential decays verifying the fits with statistical analysis. From the k values determined from the fitting of the lifetime decay curves, the number of waters present in the inner coordination sphere was calculated. Based on the coordination number and the number of waters, the number of inner sphere spots occupied by other species can be calculated assuming these species do not offer de-excitation pathways on the order of a coordinated water molecule.

For Eu, there are four main transitions that are present in the fluorescence emission spectrum. The energy transitions are depicted in the Jablonski diagram for Eu^{3+} (Figure 4.11), where S_0, S_1, and T_1 ground and excited singlet states, and triplet states, respectively. They each originate in the $^5\mathrm{D}_0$ excited state and then emit photons of various energies to relax to the $^7\mathrm{F}_1$, $^7\mathrm{F}_2$, $^7\mathrm{F}_3$, and $^7\mathrm{F}_4$ states. The two transitions most often considered are $^5\mathrm{D}_0 \rightarrow {}^7\mathrm{F}_1$ and $^5\mathrm{D}_0 \rightarrow {}^7\mathrm{F}_2$. The $^5\mathrm{D}_0 \rightarrow {}^7\mathrm{F}_1$ allowed magnetic dipole transition is not sensitive to ligand coordination making it a useful normalization peak. The $^5\mathrm{D}_0 \rightarrow {}^7\mathrm{F}_2$ allowed electric dipole transition is hypersensitive to the coordination of the Eu center to ligands. This is the transition that is observed to gain insight about the Eu-ligand coordination.

The fluorescence spectroscopy samples were prepared in a similar manner to the lanthanide XAS samples. The DGA-SBA solid was preconditioned with the solution of interest (conditions tested listed in Table 4.2) for 14-17 hours. The europium spike was then added and the samples were allowed to rock constantly for 24 hours. After that time, the samples were centrifuged for 10 minutes at 5000 rpm prior to removing all but between 20 and 50 μL of solution. This small amount of remaining solution was used to form a suspension with the DGA-SBA solid in the sample when it was vortexed. Depending on the experiment, either 2, 5, or 10 μL of the suspension was deposited on an acetone-cleaned glass microscope slide (Figure 4.12). With a gentle stream of air, the droplet on the slide was dried. The sample was then covered with a second acetone-cleaned

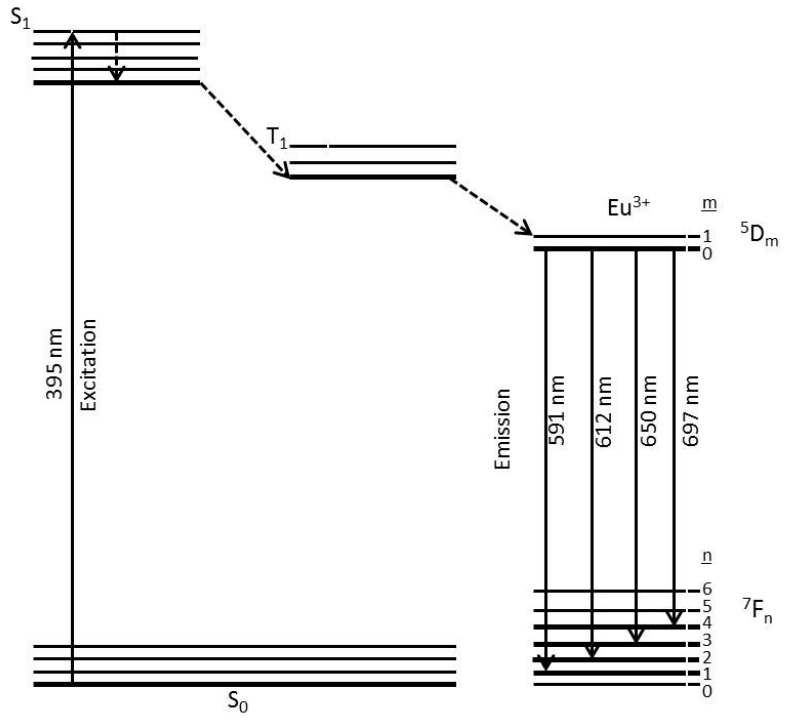

Figure 4.11: Jablonski diagram for Eu^{3+}

glass microscope slide and taped together with black electrical tape . Control samples were made that included two slides taped together with no sample, DGA-SBA between two slides with no metal, and $Eu(NO_3)_3$ and $EuCl_3$ salts in the same assembly.

Fluorescence samples were measured on a HORIBA Jobin Yvon IBH FluoroLog-3 spectrofluorimeter. They were mounted at 45 ° to the incoming beam and the detector. Fluorescence emission spectra were collected with the parameters listed in Table 4.3. For emission spectra, slit width for excitation was minimized to reduced glare from the glass slides. For the emission slits, the width was minimized to avoid saturating the detector. Lifetime measurements were done using a Jobin Yvon 5000XeF sub-μs Xe flashlamp. For these measurements, the spectrometer was set for time-correlated single photon counting and multichannel scaling measurements. Again slit width was reduced to avoid glare from the glass and minimization of exciting other materials in the sample chamber.

The lifetime data were fit on IgorPro (Version 5) and both single and double exponential decay functions were tested as well as the impact of an offset. The double exponential with offset was found to describe the data with the best fit and residual analysis. From this fit, the lifetime values associated with the two exponential decays for each sample were extracted. From the lifetimes, the number of water molecules in the inner sphere were calculated using equation 4.27.

Acid/Salt	**Acid Concentration or pH**	**Ionic Strength**
HCl/none	pH 3	0.001 M
HCl/NaCl	pH 3	0.01 M
HCl/NaCl	pH 3	0.1 M
HCl/NaCl	pH 3	1 M
HCl/NaCl	pH 3	3 M
HNO_3/none	pH 3	0.001 M
HNO_3/$NaNO_3$	pH 3	0.01 M
HNO_3/$NaNO_3$	pH 3	0.1 M
HNO_3/$NaNO_3$	pH 3	1 M
HNO_3/$NaNO_3$	pH 3	3 M
HNO_3/none	1 M	1 M

Table 4.2: Sorption matrices for Eu-DGA-SBA samples prepared for fluorescence spectroscopy

Figure 4.12: Set of Eu-DGA-SBA fluorescence samples with 2, 5, and 10 μL deposition of Eu-DGA-SBA in HNO_3 suspension

Parameter	**Value**
Excitation wavelength	395 nm
Integration time	0.5 s
Emission wavelength range	450-750 nm
Emission spectra excitation slit width	5 nm
Emission spectra emission slit width	1 nm
Lifetime emission wavelength	612 nm
Time per channel	5 μs
Channels per sweep	2000
Sweep number	50000
Counts per peak preset	20000

Table 4.3: Fluorescence emission spectra and lifetime decay measurement parameters

Chapter 5

Separations using Commercial DGA Resin

5.1 Eichrom DGA column

The DGA resin (Eichrom Technologies, Inc.) is a commercially available extraction chromatography resin. The resin was originally developed by Horwitz, et al. [3] The are two forms of the DGA resin available, that differ in the R-group on the DGA molecules. The two forms are 1) normal and 2) branched. The normal form has linear C_8 alkyl chains in each of the four R-group positions. The branched form has ethylhexyl groups in each of the four R-group positions. It consists of a porous polymer bead (Amberchrom®-CG71) support that has been coated in either the tetraoctyldiglycolamide (TODGA) or the tetraethylhexyldiglycolamide (TEHDGA).The TODGA resin with a particle size of 50-100 μm was used for this work.

Horwitz presented the synthesis and characterization of the DGA resin as well as its behavior with a number of lanthanides, actinides, and main group metals. [3] However, there were gaps in the manuscript on this work often times including such things as metal ion concentration, isotopic composition, and oxidation state purity. Additionally, stability of the resin was only addressed in terms of its reusability not in terms of its degradation with thorough analytical characterization. Reusability of a resin can vary substantially depending on acid type and concentration, radioactivity, type of radioactive emission, flow pressure, turbulence, and temperature. Additionally, testing a resin for reusability does not necessarily inform of changes in its chemical structure as the bulk behavior may remain the same despite breakdown.

In the characterization of the DGA resin, the k′ values were compared for various metals at different acid concentrations. These values are related to K_d values defined in equation 5.1 by a parameter that accounts for ligand density and loading, and volumes of the stationary and mobile phases for the packed DGA column. To relate these back to K_d values that are discussed throughout this work, k′ is divide by that parameter, defined as being equal to 0.57 (equation 5.1). [3]

$$\mathrm{k'} = 0.57\mathrm{K_d} \tag{5.1}$$

The DGA resin is supposed to have high uptake for trivalent lanthanide and actinide species. The separation goals using this resin were to 1) isolate trace amounts of Am or Cm from milligram quantities of La, and 2) separate Am from Eu, both in acidic matrices. The first goal

was important for the isolation of Am or Cm after a LaF_3 co-precipitation, which is a standard precipitation technique for recovering trace amounts of trivalent lanthanides and actinides from large volumes of solution. The second goal was intended to test the limits of the equilibrium behavior presented for this resin and determine if any selectivity of Am over Eu could be attained. Table 5.1 presents a selections of K_d values that were extracted from the DGA resin characterization manuscript. [3] Based on these values, separation schemes were developed and tested for La, Eu, Am, and Cm on the DGA resin.

Matrix	K_d for La (mL g^{-1})	K_d for Eu (mL g^{-1})	K_d for Am (mL g^{-1})
3 M HNO_3		2.6×10^4	5.8×10^4
0.5 M HNO_3	280	7.0×10^3	5.3×10^3
0.05 M HNO_3	2.6	280	61
0.01 M HNO_3		14	4
0.25 M HCl		3.5	2.6
0.1 M HCl		1.8	3.5
0.01 M HCl		2.5	44

Table 5.1: Selection of K_d values for La, Eu, and Am on TODGA resin (Eichrom Technologies, Inc.). These values were approximated from the plots presented by Horwitz, et al. for the TODGA resin after contacting the resin with the metal of interest for 1 hour. [3]

5.2 Eu, Am, and Cm Interactions with DGA Resin

The characterization of the DGA resin in the literature was done primarily using batch experiments. [3] The batch sorption data that are presented as part of this characterization are equilibrium values. In using batch sorption data to predict chromatographic behavior, it is important to keep in mind that chromatographic separations often do not allow for equilibrium to be established. Additionally, in a column compared to a batch experiments, the resin:metal ratio is usually much greater.

5.3 Separations of La, Eu, Am, and Cm with DGA Resin

5.3.1 Separation of La and Eu

Based on the batch experiments presented by Horwitz [3] and the chromatography presented by Maxwell, [75] a protocol for separating Eu and Cm from La was developed. To ensure that the La and Eu were being eluted in the expected fractions prior to using Cm, a non-radioactive separation with La and Eu was tested and the metal concentrations were quantified with ICP-MS. The flow diagram for this separation is presented in Figure 5.1a. Prior to analysis with ICP-MS, samples were carefully diluted such that they were all in approximately 2% HNO_3.

Results from this separation are presented in Figure 5.2. As predicted, both the La and Eu were retained on the resin in 3 M HNO_3 with no breakthrough. The first elution with 0.05 M HNO_3 stripped 99% of the La and none of the Eu. The final elution with 0.25 M HCl stripped the remaining 1% of the La and all of the Eu. As a result of the small amount of tailing observed for the La, future separations were done with 10 column volumes (CVs) of 0.05 M HNO_3 instead of 7.5 CVs.

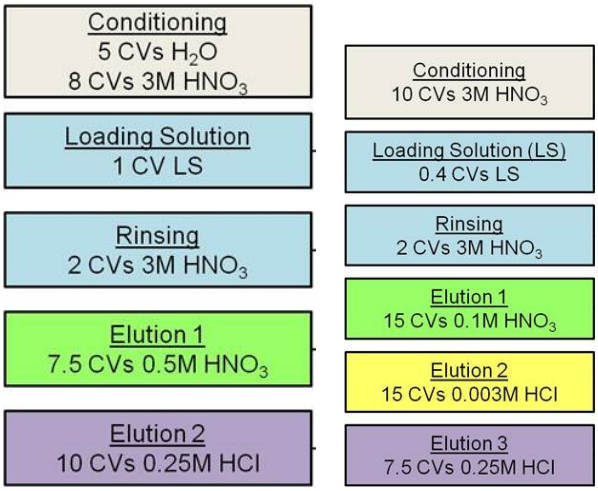

(a) La/Eu separation flow diagram

(b) Am/Eu separation flow diagram

Figure 5.1: Elution flow diagrams for a) La/Eu separation measured using ICP-MS, and b) attempted Am/Eu separation using Eichrom DGA resin

5.3.2 Separation of La and Cm

The same separation protocol tested for La and Eu was used on La and Cm. It was confirmed that the Cm behaved like the Eu in that it was retained on the column during loading in 3 M HNO_3 and La elution in 0.05 M HNO_3, and then was fully stripped from the resin in 0.25 M HCl.The separation scheme adapted from that depicted in Figure 5.1a (10 CVs of 0.05 M HNO_3 instead of 7.5 CVs) was used for all post-LaF_3 separations of Cm to prepare ^{248}Cm stock solutions.

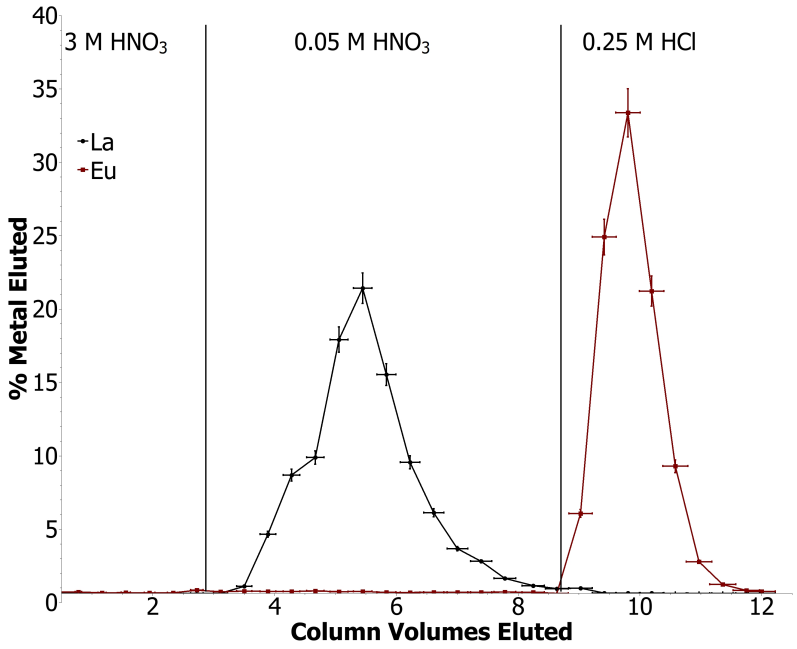

Figure 5.2: Elution profile from La/Eu separation measured using ICP-MS

5.3.3 Separations of Eu, Am, and Cm

Based on the batch experiment characterization data for the normal DGA resin, the difference in distribution coefficients appeared to be great enough between Eu and Am to obtain a separation in very low HCl concentrations. The distribution coefficients for Eu and Am in 0.003 M HCl are approximately 3.6 and 100, respectively. [3] Therefore, in 0.003 M HCl, Eu should be eluted from the column before Am. However, when the elution profile shown in Figure 5.1b was tested, only 15% of the Am was removed in 0.003 M HCl occurring in small amounts in all 21 fractions, and the remaining 85% was eluted with the Eu in 0.25 M HCl. Not only were Eu and Am not separated under these conditions, but they were eluted in the reverse order expected based on the batch sorption curves (Figure 5.3). While it is not clear from this work alone why the elution was in the opposite order compared to the predicted behavior, but different sorption kinetics could explain such differences. The predicted behaviors were based on equilibrium sorption values, however, these were after a full hour of equilibration, [3] compared to the sub-one hour chromatography column.

To further examine the elution of each of these species in HCl, HCl concentration gradients were tested. The gradient was such that the HCl concentration was increased over time. Again, as the HCl concentration in the eluent increased, the Am was first to elute from the column, followed by the Eu. The Eu/Am peak resolution was still only 0.5. An Am/Cm separation was studied independently under the same elution conditions and the Am and Cm elution occurred simultaneously, however the bulk of the Cm was stripped after the bulk of the Am (Figure 5.4). This same separation was repeated using a long, thin glass column packed with the normal DGA resin to attempt to increase the number of theoretical plates. The separation was definitely an improvement compared to using the pre-packed cartridges, however due to issues with the germanium detectors, the quantification of Am was not good enough for comparison to the Cm. Additionally, while running the column, tiny bubbles were observed along the glass edges as well as slight discoloration of the resin. This could be due to degradation of the resin that was not visible in the cartridges because the cartridges have opaque walls.

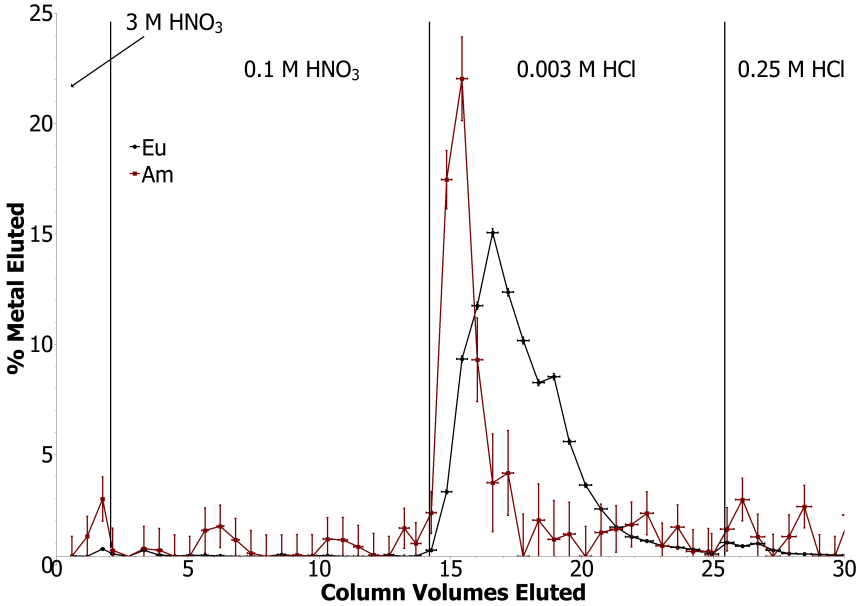

Figure 5.3: Elution profile from attempted Am/Eu separation using Eichrom DGA resin

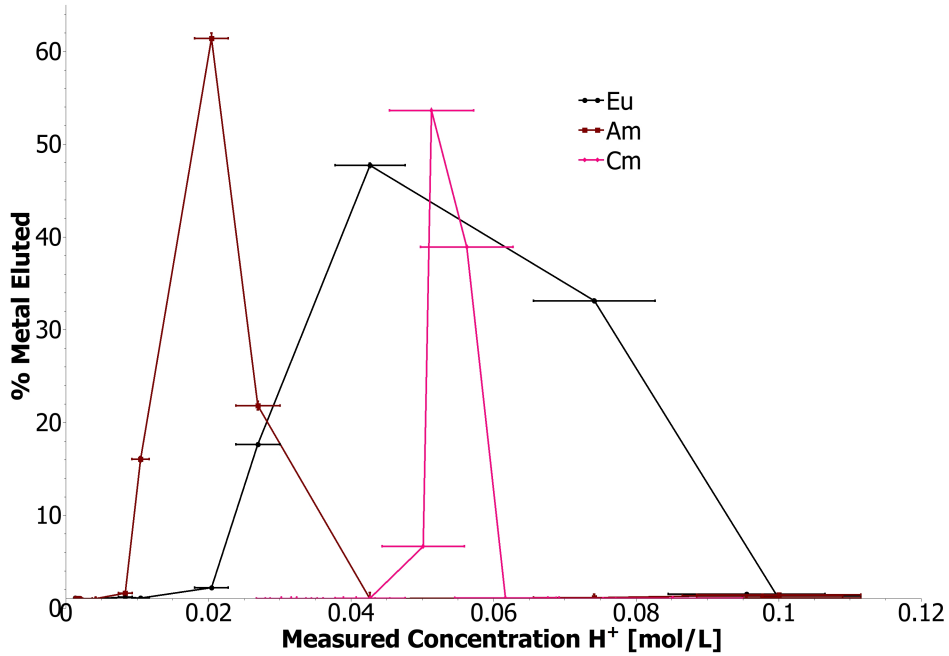

Figure 5.4: Elution profiles of Am/Eu/Cm as a function of measured H^+ concentration. The Am and Eu were measured in the same chromatography experiment, however, the Cm was from a separate chromatography experiment and is overlaid on the Am/Eu data

5.4 Summary, Conclusions, and Outlook

The commercial DGA resin was useful for separations of Eu or Am from an excess of La. High separation factors were observed and this methodology is now in use for separations following LaF_3 co-precipitations. The attempt to separate Eu, Am, and Cm from one another, however, was much less successful. The elution trend that should have existed based on the batch experiment results in the literature was not observed. Additionally, discoloration and bubbling in the resin seemed to point to some sort of degradation of the material during experiments. Degradation of a coated-support solid-phase extractant is not surprising as the ligand is not actually bound to the solid support. If a small gap is created in the ligand coating, the entire organic layer could become more susceptible to being removed from the solid support. Thus, in an effort to develop more stable solid-phase extractants, materials with the ligand covalently bound to the solid support are the subject of the rest of this work.

Chapter 6

Interactions of Trivalent Al, Sc, and Eu with Carbamoyl Acetamide Functionalized Mesoporous Silica

Earlier work on functionalized mesoporous silica focused mainly on the metal sorption experiments as opposed to the binding mechanisms that allow for selectivity. [54, 65, 79, 118–120] Additionally, the extent of degradation of functionalized mesoporous silica was not thoroughly studied, which raises the question of whether the ligands decomposed after acid contact. One of the goals of the work presented here is to elucidate the fundamental interactions of two trivalent cations with a CA-functionalized mesoporous silica using NMR spectroscopy. By using various NMR spectroscopic techniques, a more thorough understanding of these interactions is possible. In this work, the metal, surface, and ligand nuclei were all probed to create a detailed picture of the chemistry involved with this system. Despite the relatively large number of publications studying metal uptake on functionalized silica, NMR has not been used to probe these metals directly. NMR has been used to probe metals in organometallic crystals and in mineral environments of these same metals, [33, 37, 38, 121–124] but the work presented here is the first to examine the binding mechanism of the metal to functionalized mesoporous silica using NMR of the metal nuclei. While ligands have been grafted to silica for catalytic applications in the past, there has been minimal characterization of the metal complexes formed. [125–127] There has been one X-ray absorption spectroscopy study of the metal [128] and nuclear magnetic resonance (NMR) spectroscopy studies characterizing the ligands bound to metals [129, 130], but no direct NMR characterization of the metals had been reported. The manuscript published from the Al and Sc work presented in this chapter was the first to directly characterize the metal ions bound to an organically-modified mesoporous silica material using NMR spectroscopy. [131] Additional studies not included in the manuscript, particularly focused on different silica morphologies and Eu uptake are included in the this chapter as well.

6.1 CA Functionalized Mesoporous Silica

This work was focused on a set of materials that were made by grafting N-[5-(trimethoxysilyl)-2-aza-1-oxopentyl]caprolactam (Gelest) to various types of mesoporous silcia via different functionalization pathways. N-[5-(trimethoxysilyl)-2-aza-1-oxopentyl]caprolactam (Figure 6.2), denoted as

the CA ligand from here on, was chosen because the binding site is similar to that of a malonamide (Figure 6.1). Malonamides have been shown to successfully complex trivalent lanthanides for nuclear fuel cycle application. [17, 26, 132–138]

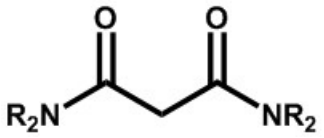

Figure 6.1: General structure for a malonamide

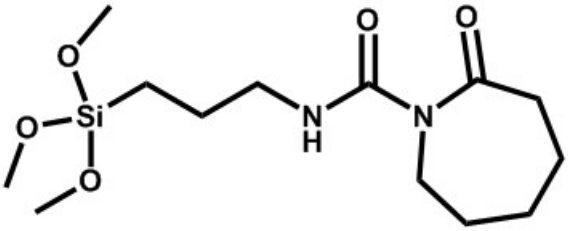

Figure 6.2: N-[5-(trimethoxysilyl)-2-aza-1-oxopentyl]caprolactam, 'CA'

The first part of this work focused on Eu(III) uptake on CA-modified mesoporous silica. Based on the similarity to a malonamide, it was expected that this ligand would complex Eu(III) and that it would be an ideal test ion to probe various characteristics about the substrates themselves. A variety of silica materials were tested to better understand the impact of pore diameter and shape. Additionally, materials synthesized via three different mechanisms to anchor the ligand to the silica were studied to determine whether this would impact metal ion uptake.

It was determined that testing other trivalent cations with smaller ionic radii could help explain the unexpected Eu sorption results on the CA-silica materials. Two cations, Al (0.39-0.535 $\AA$) and Sc (0.745-0.870 $\AA$), [139] with smaller ionic radii were studied to determine if their ionic radius would impact how they bind to the functionalized mesoporous silica.

6.2 Synthesis and Characterization

The mesoporous silica was synthesized and functionalized via the methodologies discussed in sections 4.2 and 4.3. The CA ligand, N-[5-(trimethoxysilyl)-2-aza-1-oxopentyl]caprolactam (Figure 6.2), was commercially available from Gelest. The synthesis of the CA-modified silica materials was carried out by Anthony Bruchet. Characterization of the various materials primarily consisted of nitrogen adsorption isotherms. However, for the 8 nm SBA-15 modified with the CA ligand using solution polymerization, full characterization was performed, as this material was used for all of the Al and Sc experiments.

The solution-polymerized CA-modified silica material (CA-SBA) was characterized with NMR spectroscopy, nitrogen adsorption isotherms, and TGA. Final ligand density on the surface was 0.59 molecules per nm^2 as measured by TGA. The TGA ligand density is a minimum of that value because it assumes that the mass loss is attributed to complete ligand volatilization. Partial ligand volatilization would result in a higher ligand density. Both single-pulse (SP) and CP ^{29}Si NMR spectroscopy were used to study the ligand grafting to the surface. The ^{29}Si{^{1}H} CP/MAS NMR spectrum of the pristine material (Figure 6.4a) has two groups of peaks: Q (δ_{Si}= -92 to -112

ppm) and T (δ_{Si}= -50 to -70 ppm) peaks, the latter being silicon atoms bound to the ligand. Q^n and T^m peaks are defined as $Si(OSi)_n(OH)_{4-n}$ and $SiR(OSi)_m(OH)_{3-m}$, respectively, where R is a carbon chain. A $^{13}C\{^1H\}$ CP/MAS NMR spectrum confirmed that the CA ligand was intact on the surface and did not break down during the functionalization process (Figure 6.5a). The SP spectrum, however, could not be used for T peak quantification as there was not enough signal from the T peaks as a result of their low abundance. The spectrum presented in Figure 6.3 was collected for 5 days and so a spectrum that had better signal-to-noise would take prohibitively longer to collect.

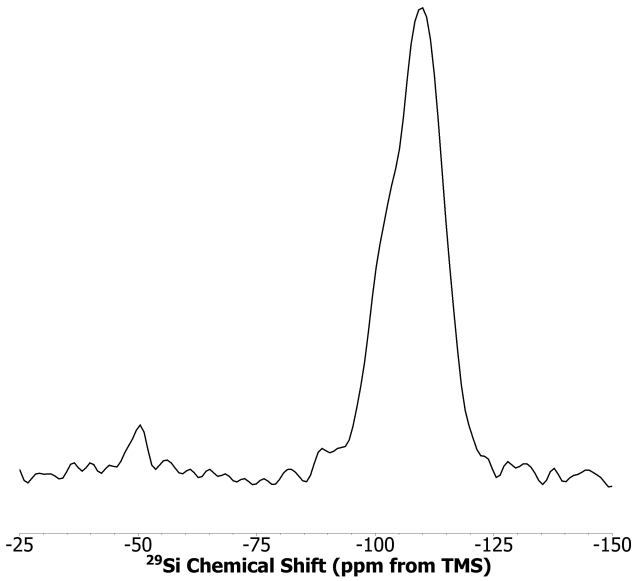

Figure 6.3: ^{29}Si SP/MAS NMR spectra for pristine CA-SBA. The resonances for the bulk silicon atoms are the Q peaks (Q^2, Q^3, and Q^4 have shifts of δ_{Si}= -93, -97, and -107 ppm, respectively) and for the surface silicon atoms are the T peaks (T^1, T^2, and T^3 have shifts of δ_{Si}= -51, -58, -66 ppm, respectively.

6.3 Acid Catalyzed Hydrolysis

Very few studies have examined the degradation of organically modified silica in the presence of acid. The state of the functional layer of the silica after contact with acid is important, as it impacts the binding mechanism with metals of interest as well as the lifetime of the material. A previous study on organically modified silica has indicated slight degradation of these materials at the silane anchor in the presence of acid. The results from ^{29}Si and ^{13}C NMR spectroscopy were used to investigate the mechanism of degradation for CA functionalized SBA-15 in the presence of nitric acid. The$^{29}Si\{^1H\}$ CP/MAS NMR (Figure 6.4b) and $^{13}C\{^1H\}$ CP/MAS NMR (Figure 6.5b) were performed on the solid recovered after 24 hours of contact with pH 3 nitric acid (preconditioned solid) and compared to the pristine functionalized material (Figures 6.4a and 6.5a, respectively). This experiment was done to determine the extent of ligand degradation from pH 3 nitric acid prior to metal contact.

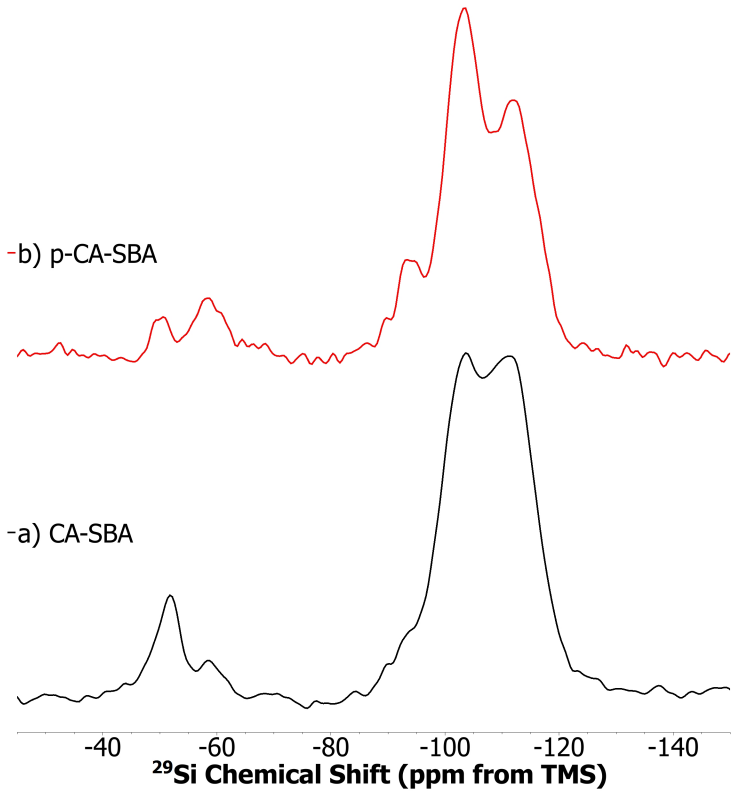

Figure 6.4: ^{29}Si{^{1}H} CP/MAS NMR spectra for CA functionalized SBA-15 a) pristine solid (CA-SBA) and b) pre-conditioned solid (p-CA-SBA). The resonances for the bulk silicon atoms are the Q peaks (Q^2, Q^3, and Q^4 have shifts of δ_{Si}= -93, -97, and -107 ppm, respectively) and for the surface silicon atoms are the T peaks (T^1, T^2, and T^3 have shifts of δ_{Si}= -51, -58, -66 ppm, respectively.

In the ^{29}Si{^{1}H} CP/MAS NMR spectrum of the pre-conditioned sample, some T peaks remain indicating that the acid treatment did not completely degrade the ligand-silane anchor (Figure 6.4b). As the CP/MAS NMR spectra for the pristine and pre-conditioned samples were collected under identical condition, the relative ratios of T^1 and T^2 can be compared to determine the relative change in concentration of each of these species. This method was used as opposed to quantifying the T peaks of a single-pulse (SP) experiment due to the minimal ligand surface coverage, resulting in very low T peak intensity even after multiple days of collection (Figure 6.3). The ratio of T^1 (δ_{Si} = -51 ppm) to T^2 (δ_{Si} = -58 ppm) [140] is lower (T^1:T^2 is 4.1 and 0.36 for pristine and preconditioned, respectively) than the pristine solid prior to contact with acid. The decrease in T^1 is not surprising as a T^1 linkage to the surface is the most hydrolyzable of T^1, T^2, and T^3. However the extent of hydrolysis was more than expected at approximately 90% loss of T^1 peak intensity, correlating to approximately the same loss in T^1 species on the surface under the aforementioned identical collection conditions. Specifically, the T^1 species that hydrolyze are converted to Q^3 species. The ^{13}C{^{1}H} CP/MAS NMR spectra look similar before and after contact with the pH 3 nitric acid, however, the peak at 48 ppm decreases significantly after acid contact causing corresponding changes in peak intensities for the other CH_2 groups. This peak is assigned

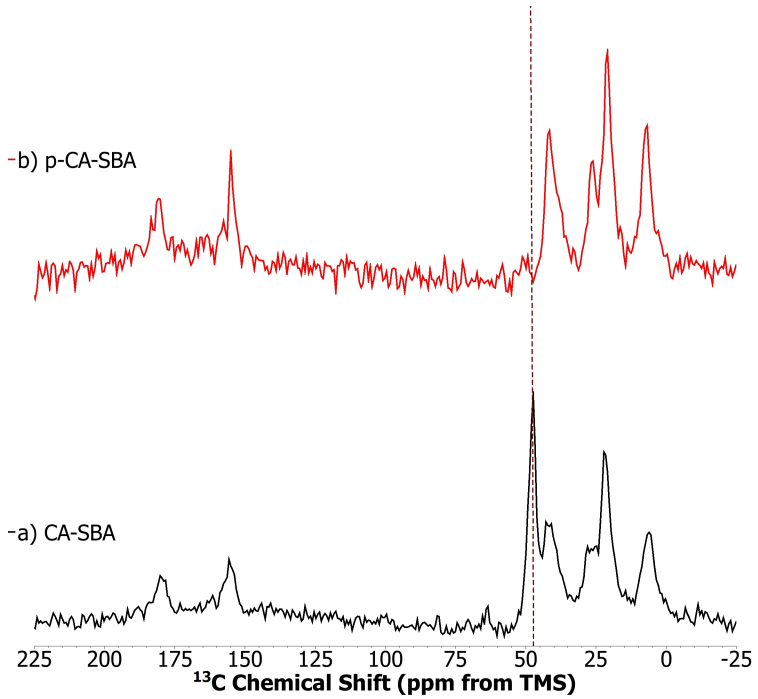

Figure 6.5: $^{13}C\{^{1}H\}$ CP/MAS NMR spectra for CA functionalized SBA-15 a) pristine solid (CA-SBA) and b) pre-conditioned solid (p-CA-SBA). Dashed line highlights the 48 ppm resonance in the CA-SBA spectrum that is nearly absent in the p-CA-SBA spectrum, indicating ring-opening.

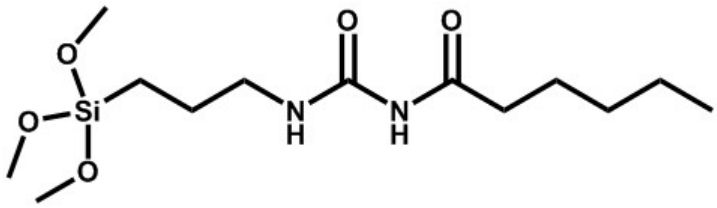

Figure 6.6: Ring-opened structure of N-[5-(trimethoxysilyl)-2-aza-1-oxopentyl]caprolactam grafted to silica after contact with pH 3 nitric acid

to the carbon directly bound to the nitrogen in the seven-membered ring. The decrease in the peak indicates that the ring opened in the presence of acid (Figure 6.6). There is an increase in intensity at 7 ppm resonance, which is indicative of the terminal CH_3 produced by the opening of the ring.

6.4 Batch Sorption Experiments

Batch sorption experiments with Eu were conducted with solid-to-liquid ratios of 1 mg mL^{-1}. The only exceptions to this were when samples were prepared for NMR spectroscopy. The solid of interest was weighed into a polypropylene 15 mL centrifuge tube. The appropriate amount of solution required to obtain the aforementioned solid-to-liquid ratio was added and the pH adjusted if necessary. Samples were shaken well and then allowed to rock for 14-17 hours such that the solid could pre-equilibrate with the solution. After this time, the metal spike solution was added, samples shaken well, and the pH adjusted. Aliquots were taken at various time points throughout

each experiment. Prior to aliquot removal, samples were typically centrifuged for 5 minutes at 5000 rpm.

Stock solutions of 70 mM were prepared from the aluminum and scandium nitrate salts. Stock solutions had pH values between 2.5 and 3.8. In polypropylene centrifuge cones, 40 mg of solid (either bare SBA-15 with 8 nm pores or SBA-15 functionalized with the CA ligand) was combined with 11 mL of ultrapure water (18.0 MΩ•cm) and , if necessary, acidified with 0.1 M nitric acid until the pH was less than 5.5. Samples were shaken and left to pre-equilibrate for approximately 24 hours. After 24 hours, 1 mL of the appropriate metal nitrate stock solution was added to the pre-equilibrated samples and acidified to pH 3.0 with 0.1 M nitric acid. The total metal ion concentration was approximately 6 mM. Aliquots were removed from the supernatant of the samples every few hours for solution-state NMR spectroscopy analysis. After 24 hours from the time of metal addition, the solid was collected from the sample via suction filtration through a 0.22 μm filter, washed with ethanol, and allowed to air dry overnight. A control sample was made by combining 40 mg of the CA functionalized silica with 12 mL of pH 3 nitric acid, contacting for 24 hours, and collecting the solid via suction filtration. An additional desorption on the Al-CA-SBA and Sc-CA-SBA samples was performed by contacting the solid with Milli-Q water for 10 minutes prior to collecting the solid via suction filtration, washing with water then ethanol, and drying overnight.

6.4.1 Eu(III) uptake

In solvent extraction systems, 2-3 malonamide ligands have been found to complex with each Eu(III) center. In a nitrate system, however, Eu(III) complexed by two malonamide ligands and three nitrate ions is most prevalent. [136, 141–144] In systems where malonamides were immobilized on surfaces, it became less clear how many ligands were complexing the metal, however it seemed to be more than one. [132] Ideal malonamide-Eu complexation occurred at moderately acidic pH values and high nitrate concentration. [143] As such, initial batch sorption experiments were conducted in the acid range of 1 M to pH 3 HNO_3 with nitrate concentration (3 M). The pH was only raised as far as pH 3 to avoid any deprotonation of the silica surface.

Effect of acidity, pore diameter, and ionic strength

Batch sorption experiments with Eu(III) were conducted using CA-SBA to measure uptake a variety of acidities. The Eu(III) stock was 1.2 mM in Eu(III) with ^{152}Eu tracer in 0.001 M HNO_3. At this concentration, a 50 μL spike in a 6 mL sample resulted in a Eu concentration in the sample of 10 μM. For these studies, materials with four different pore diameters created with three separate functionalization methods were studied, resulting in 12 materials in total. These materials are detailed in Table 6.1. Eu sorption to the monomeric and surface-polymerized materials was studied at four different HNO_3 concentrations ranging from 1 M to 0.001 M. The solution-polymerized material was not tested as it was expected to exhibit similar binding to the surface-polymerized material. For each of these sorption experiments, the total NO_3^- concentration was held at 3 M using $NaNO_3$. Nitrate concentration was kept so high because malonamides had been shown in the literature to most effectively complex lanthanides and actinides at high nitrate concentrations required to form the nitrate complex of the metal. [143] Acidity was found not to affect uptake and this is presented in Figure 6.7.

Additionally, blanks with only solution and Eu were tested to establish a baseline amount of activity added, and determine whether sorption to the polypropylene tubes was occurring. Sorp-

Mesoporous Silica Types	Pore Diameters (nm)	Grafting Methods
SBA-15	5	Monomeric
	6.4	Surface-Polymerized
	8	Solution-Polymerized
MCF	30	

Table 6.1: CA modified mesoporous silica materials tested

tion to the tubes was not occurring and sorption to the bare silica was less than 10% of the Eu in all cases. CA-SBA that had been grafted on SBA-15 with 5, 6.4, and 8 nm pores and MCF with 30 nm pores were examined to determine if Eu(III) was sorbing to the CA-SBA differently depending on pore diameter. If this was the case, then diffusion limitations or clogging of narrow pores could be an issue. No major differences were observed between the pore sizes (Figure 6.7), however the 5 nm material did have slightly higher uptake. This could be a result of the ligands getting clustered in clogged pores, forcing them to be closer together. This would support the hypothesis that multiple ligands are required to bind each Eu(III) center.

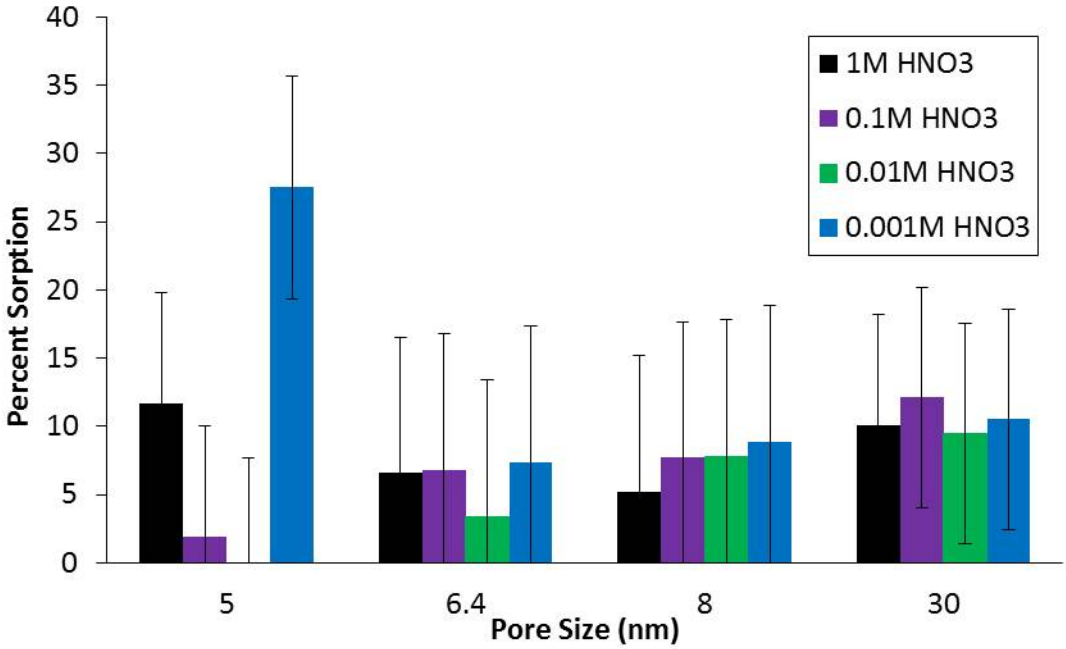

Figure 6.7: Sorption of Eu on CA-SBA as a function of pore diameter and acidity. CA-SBA was functionalized via the surface polymerization method.

The results showed very little to no sorption on the materials. There was a small amount of sorption, 25%, on the surface-polymerized 5 nm material at 0.001 M HNO_3, but this was only after 24 hours and was not seen in any of the other samples. Sorption tended to increase to 10% in all samples after 24 hours. As larger pore sizes did not show improved sorption, and different functionalization methods did not improve sorption, it is expected that the primary issue is the silane itself. To verify that low uptake was not due to occupying all the binding sites with sodium from the high $NaNO_3$ concentration, Eu sorption from a 0.001 M HNO_3 solution that had no added salt was tested. There was still no Eu sorption above 10% for any of the CA-SBA materials.

There are two potential reasons behind the low Eu uptake. First, the conformation of this ligand that is most energetically stable is not the conformation necessary for binding. The more stable conformation has the oxygens in a trans conformation as opposed to cis. The second problem, is that more than one ligand is probably needed to bind the Eu(III) because it has a fairly large ionic radius for single diamide ligand binding.

To probe the first issue, the impact of increasing the temperature of the solution during the batch experiment was explored. One of the hypotheses regarding why CA-SBA had a negligible amount of Eu(III) uptake was that the thermodynamically stable conformation of the CA ligand was not the conformation required for complexation. To complex with a metal, the carbonyls would have to be pointing in the same direction, towards the metal. Based on a quick calculation on Chem 3d, the trans-conformation was more thermodynamically stable (Figure 6.8). To potentially give the ligand enough energy to rotate and align the carbonyls, Eu(III) uptake at a slightly elevated temperature was studied.

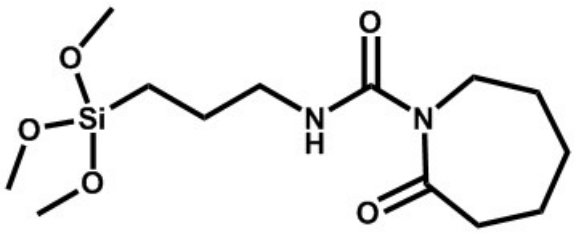

Figure 6.8: N-[5-(trimethoxysilyl)-2-aza-1-oxopentyl]caprolactam ligand rotated in potentially thermodynamically more stable conformation

For the temperature study, samples were heated to $40 - 50°$C. The materials tested were bare 8 nm SBA-15, and CA-SBA functionalized with monomeric and surface polyermerization methods. The solution matrix was 0.001 M HNO_3 with total NO_3^- concentration of 3 M. Five aliquots over a total time period of 8 hours were taken, however due to limitations on the heating setup, continuous shaking of the samples during this time was not possible. There was not significantly increased sorption, but compared to the room temperature sample, it seems that there was a very slight improvement; The surface polymerized sample at room temperature after approximately 3.5 hours showed approximately 4% sorption, whereas the heated sample after this same amount of time had 14% sorption (Figure 6.9). Note, however, that the error bars on these % sorption values are 8-10%.

Based on the slight increase in sorption, thermodynamics seems to have played a small role in causing the ligand to not complex the Eu(III). Maintaining a conformation that was suitable for complexation is unlikely due to the non-planar 7-membered ring. However, the acid hydrolysis studies did indicate opening of the 7-membered ring, which would make free rotation about the bonds less hindered. Thus, the main issue still seems to be ligand density on the surface, particularly in the case of the monomeric functionalized material where there is a more homogenous coating of ligand on the surface. As this ligand is bulky, a densely packed monolayer cannot be formed. The lack of a monolayer is supported by the presence of a T^1 peak in the $^{29}Si\{^1H\}$ CP/MAS NMR spectrum of the pristine CA-SBA sample. With too low ligand density, multiple ligands may not be close enough together to form multi-ligand:metal complexes.

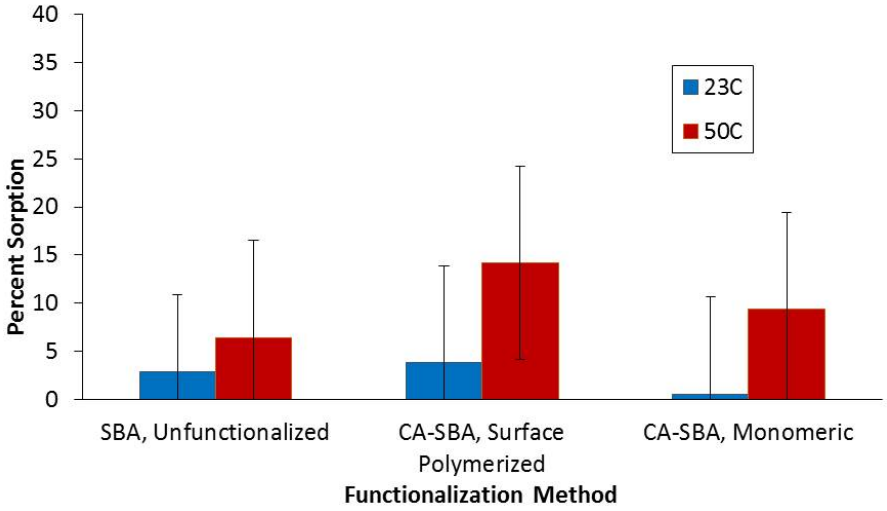

Figure 6.9: Sorption of Eu on CA-SBA and bare SBA as a function of temperature and surface modification method

6.4.2 Al(III) and Sc(III) uptake

As Eu(III) has a large ionic radius, the necessary number of ligands required for complexation may be too high for the CA-SBA material to bind the Eu. On average, Eu(III) complexes with 3-4 malonamide ligands in a solvent extraction system. If the CA ligands are too far from one another to form 3-4:1 ligand:metal complexes, 1:1 or 2:1 complexes may be the only possibility. These complexes may not be strong enough to extract the Eu(III) from solution. Trivalent cations with smaller ionic radii, however, could potentially bind to the CA ligand with only one or two ligands per metal center. To that end, Al(III) and Sc(III) interactions with the CA-SBA material were tested. The ionic radii for Al(III) and Sc(III) are in the range of 0.39-0.535 Åand 0.745-0.870 Å, respectively, compared to Eu(III) at 0.947-1.120 Å. [139]

The solution ^{27}Al NMR measurements of the aqueous aliquots removed during the Al sorption experiments indicated that approximately 35% of the Al is bound to the functionalized silica surface after one day of metal contact time (Figure 6.10a). An analogous measurement of ^{45}Sc on the solution phase from the Sc sorption experiment indicated that approximately 49% of the Sc in solution sorbed to the solid (Figure 6.10b). While the resonance in the solution phase of the Sc sorption experiment was shifted by -1 ppm relative to the Sc blank, the sorption can still be determined from the integrated peak intensity, as the shift only indicates a change in local environment for the Sc. Based on the post-functionalization surface area of the CA-SBA material and the initial 6 mM Al and Sc concentrations for each of these samples, the metal ion coverages were 1.3 and 1.8 μmol/m^2 for Al and Sc, respectively.

6.5 Interactions of Al and Sc with SBA

To understand the behavior of Al(III) and Sc(III) on functionalized SBA-15, the interactions of these metals with the bare SBA-15 surface were first characterized. The silica surface may not be coated in a perfect monolayer of ligand based on the surface coverage compared to literature values. [54] Thus, there are gaps between the ligand molecules in which the metals can interact

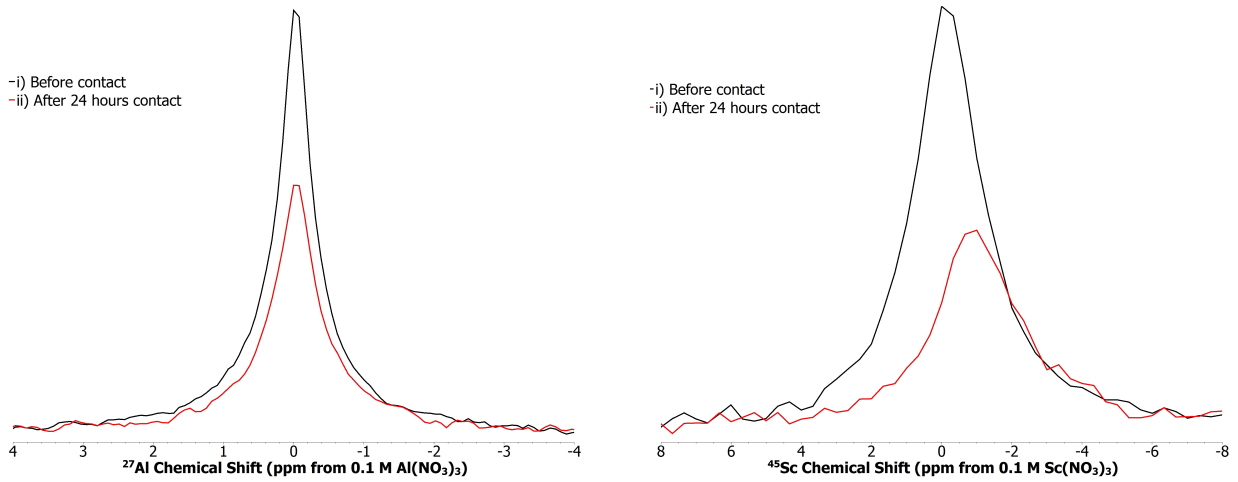

(a) ^{27}Al SP/MAS NMR spectra (b) ^{45}Sc SP/MAS NMR spectra

Figure 6.10: ^{27}Al and ^{45}Sc SP/MAS NMR spectra of solution from Al an Sc sorption to CA functionalized SBA-15 i) before contact with CA-SBA and ii) after contact with CA-SBA for 24 hours

with the silica surface. The ^{29}Si{^{1}H} CP/MAS NMR spectrum (Figure 6.11a) of Al on SBA-15 (Al-SBA) indicated the presence of Q^4, Q^3, and Q^2 surface species. The relative ratios of each of the Q peaks indicate that the Q^3 sites are the most prevalent surface species, which is expected in an unfunctionalized silica material at this pH. The substitution of Al for a Si in the SBA-15 would result in a chemical shift of between δ_{Si} =-97 and δ_{Si} =-107 ppm, [89] and would overlap with the Q^3 peak centered at δ_{Si} =-102 ppm. Based on the small amount of Al on the surface relative to the total number of surface Si sites, it is unlikely that any change in the ^{29}Si{^{1}H} CP/MAS NMR spectrum would be observed from the pre-conditioned sample compared to the Al-contacted sample. [122] Similar reasoning follows for why we would not expect to see a change in the ^{29}Si{^{1}H} CP/MAS NMR spectrum for the Sc sorption on SBA-15 (Sc-SBA). The ^{29}Si{^{1}H} CP/MAS NMR spectrum (Figure 6.11b) of the Sc-SBA also contained Q^4, Q^3, and Q^2 peaks and is similar to that collected for Al-SBA. The Al-SBA and Sc-SBA spectra do not differ significantly from one another or from acid treated silica that has not been contact with a metal, following the expected behavior for low metal coverage.

The ^{27}Al SP/MAS NMR spectrum of Al-SBA (Figure 6.12a) has a broad asymmetric peak with a peak maximum at approximately δ_{Al} = 50 ppm and corresponds to Al in tetrahedral coordination. This result agrees with the literature where Al was found to bind to the silanol groups on the silica surface in bidentate tetrahedral complexes. As noted by Houston, the width of this peak is indicative of a motion-constrained species which supports a bidentate complex to the silica surface. [122] The Al here is binding to the deprotonated silanol groups on the silica surface forming an inner sphere complex. Additionally, a sharp peak near δ_{Al} =0 ppm is indicative of $Al(H_2O)_6^{3+}$ trapped in the pores of the silica. Nevertheless, approximately 88% of the Al bound to the solid had a coordination number of 4 and was bound as an inner sphere complex to the surface.

The ^{45}Sc SP/MAS NMR spectrum (Figure 6.13a) of the Sc-SBA has a single, asymmetric peak with a peak maximum at about δ_{Sc} = 46 ppm and corresponds to that typical for a Sc coordination number of seven. The 7-coordinated Sc observed here is unexpected given the well-ordered surface structure of the SBA-15. In well-ordered environments, Sc typically adopts a coordination

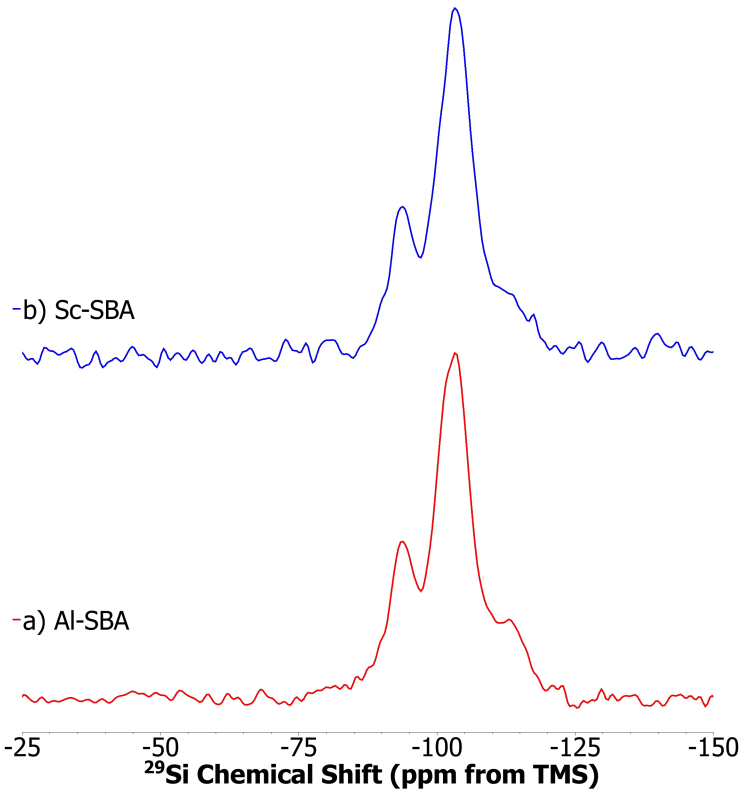

Figure 6.11: ^{29}Si{^{1}H} CP/MAS NMR spectra for solids from a) Al (Al-SBA)and b) Sc (Sc-SBA) sorption to bare SBA-15. The resonance for the bulk silicon atoms are the Q peaks (Q^2, Q^3, and Q^4 have shifts of δ_{Si}= -93, -97, and -107 ppm, respectively).

of 6 or 8, [33–36] but a 7-coordinated Sc is more typical of a disordered local environment. [35–39] Additionally, in aqueous systems at pH 3.5, Sc has been found to be most stable in a 7-coordinate complex. [35] The Sc has been assigned this coordination, however, due to the measured chemical shift which is in the range expected for 7-coordinated species and far from the expected chemical shifts of both the 6 and 8-coordinated species. [38] Unlike the Al-SBA solid spectrum, no peak corresponding to aqueous $Sc(NO_3)_3$ was observed . The cause of retention of the aqueous metal salt in some samples but not others was not identified.

6.6 Interactions of Al and Sc with CA-SBA

The interactions of Al(III) and Sc(III) as model trivalent cations with CA functionalized SBA (CA-SBA) were examined by analyzing the solutions and solids after metal sorption. Initial analysis of these solids by ^{29}Si and ^{13}C NMR indicate that the same mechanism of CA ligand degradation observed for the preconditioned solid occurs in these systems as well (Figures 6.14 and 6.15). Insight into the binding of Al and Sc to the CA-SBA was gained from the direct observation of the local Al and Sc environments using ^{27}Al and ^{45}Sc NMR spectroscopy, respectively.

The ^{27}Al SP/MAS NMR spectrum (Figure 6.12) of aluminum sorbed to the CA-SBA-15 (Al-CA-SBA) contains two distinct peaks with peak maxima at δ_{Al} = 10 ppm and δ_{Al} = 48.5 ppm

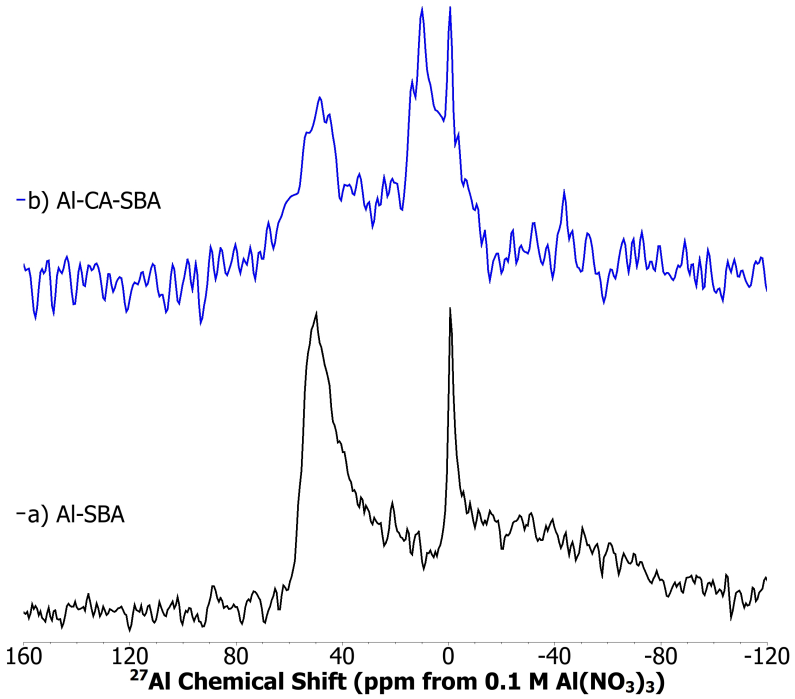

Figure 6.12: ^{27}Al SP/MAS NMR spectra of solids from Al sorption to a) bare SBA-15 (Al-SBA) and b) CA functionalized SBA-15 (Al-CA-SBA)

that correspond to Al in octahedral and tetrahedral coordination, respectively. Additionally, there is a sharp peak at $\delta_{Al} = 0$ ppm that is due to aqueous $Al(H_2O)_6{}^{3+}$ trapped in the pore structure, such as observed in the Al-SBA sample. Based on the Al-SBA results, the tetrahedral Al is again assigned to Al sorbed directly to the silica surface. Given its absence in the Al-SBA sample, the octahedral Al represents complexation with the ligand carbonyls. About 46% of the sorbed Al is 4-coordinate compared to the 88% observed for the Al-SBA sample and 49% is now represented by a 6-coordinate species. The remaining 12% and 5% of Al in the Al-SBA and Al-CA-SBA, respectively, are from the $Al(H_2O)_6{}^{3+}$ species. If the aluminum had precipitated as a hydroxide, the chemical shift would be higher than that assigned to the octahedral peaks. [145] Additionally, the concentration and pH used for these studies limits Al-hydroxide formation. [121] Based on this spectrum and the total amount of sorbed Al, a 1:1 metal ligand coordination for the octahedral Al is likely with the remaining space in the coordination sphere occupied by water molecules.

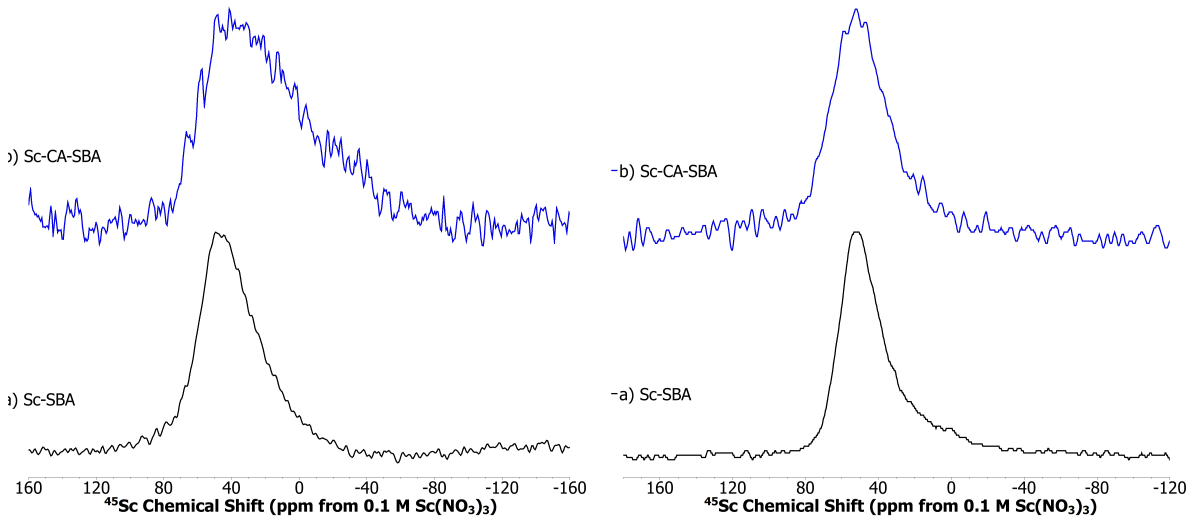

300 MHz 500 MHz

Figure 6.13: ^{45}Sc SP/MAS NMR spectra of solids from a) Sc sorption to bare SBA-15 (Sc-SBA) and b) CA functionactionalized SBA-15 (Sc-CA-SBA) collected on 300 and 500 MHz spectrometers. The chemical shifts for 6, 7, and 8-coordinated Sc occur in the ranges of δ_{Sc}= 100 to 160 ppm, δ_{Sc}= 10 to 70 ppm, and δ_{Sc}= -10 to -50 ppm, respectively.

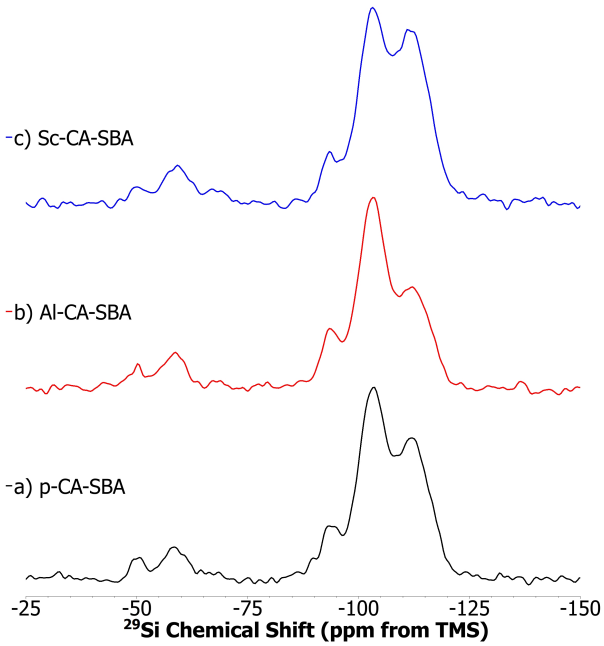

Figure 6.14: ^{29}Si{^{1}H} CP/MAS NMR spectra for solids from a) pre-conditioned CA functionalized SBA-15 (p-CA-SBA), b) Al sorption to CA functionalized SBA-15 (Al-CA-SBA), and c) Sc sorption to CA functionalized SBA-15 (Sc-CA-SBA).

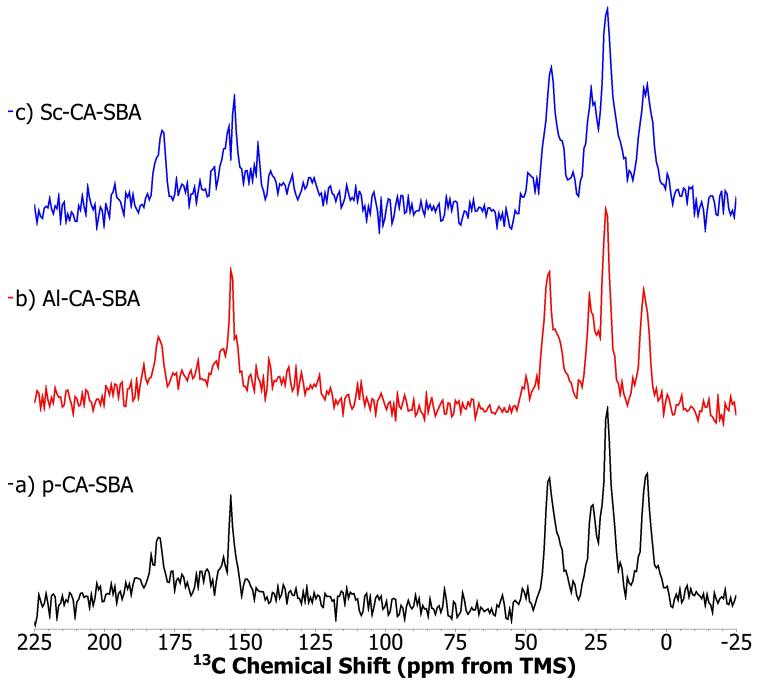

Figure 6.15: $^{13}C\{^{1}H\}$ CP/MAS NMR spectra for solids from a) pre-conditioned CA functionalized SBA-15 (p-CA-SBA), b) Al sorption to CA functionalized SBA-15 (Al-CA-SBA), and c) Sc sorption to CA functionalized SBA-15 (Sc-CA-SBA).

A desorption experiment was performed on the Al-CA-SBA solid to determine the reversibility of the sorption reactions. The ^{27}Al SP/MAS NMR spectrum collected of the desorbed sample (Figure 6.16) indicates a near complete loss of the peaks that had been present prior to water contact to the point where instrument noise overwhelms any ^{27}Al signal. The lack of Al signal in this sample indicates that brief contact (10 min) with water was sufficient to desorb the Al. Based on Al speciation, [121] it is expected that at the pH of Milli Q water, Al precipitates as $Al(OH)_3$ which is subsequently washed off of the surface. This result indicates that the Al sorption is reversible which is necessary for any materials used with chromatographic applications.

The ^{45}Sc SP/MAS NMR spectrum (Figure 6.13b) of the Sc sorbed onto the CA functionalized silica (Sc-CA-SBA) has a single, broad asymmetric peak with the peak maximum located at approximately δ_{Sc} = 36 ppm and again corresponds to that expected for a 7-coordinated Sc species. [38,146] It has been postulated that the Sc could adopt a distorted capped trigonal prism geometry similar to that proposed before for Sc compounds with bidentate oxygen-donor ligands. [37] In the spectrum collected on the 300 MHz spectrometer, the broad peak could encompass a small shoulder centered at δ_{Sc} =-20 ppm, corresponding to 8-coordinated Sc. To determine whether a resonance at δ_{Sc} =-20 ppm was present or whether the broadening of the peak to this range of chemical shifts was due to the impact of the ligands on the electric field gradient, the sample was measured on a 500 MHz spectrometer (Figures 6.13b and 6.17). In this spectrum, it is clear that there is no peak at that chemical shift, and thus the presence of 8-coordinated Sc has been ruled out. Despite Sc having the same coordination number for both the Sc-SBA and the Sc-CA-SBA samples, the spectra were still unique in that the Sc-CA-SBA has a much broader peak indicating a change in local coordination environment for the Sc nuclei in the Sc-CA-SBA sample. As the only

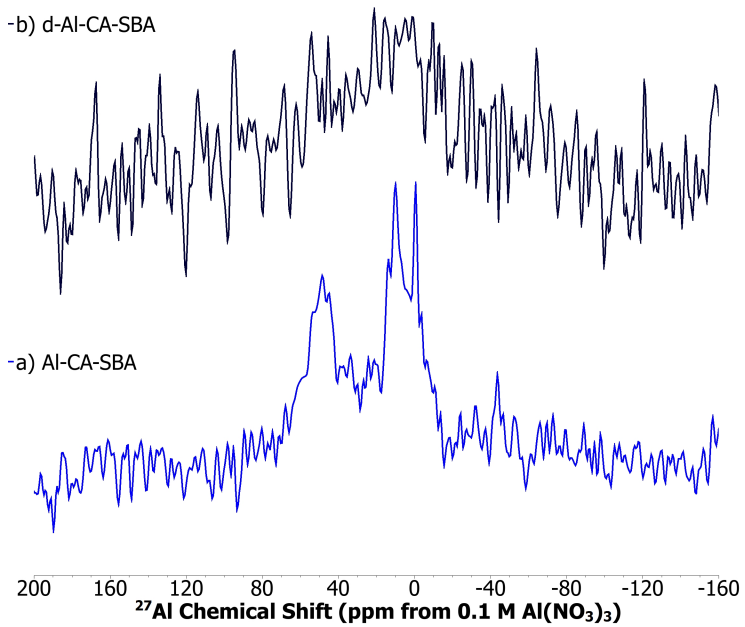

Figure 6.16: ^{27}Al SP/MAS NMR spectra of solids from Al sorption to CA functionalized SBA-15 a) before (Al-CA-SBA) and b) after contact with water for desorption (d-Al-CA-SBA)

difference between these two samples is the presence of the CA ligand in the Sc-CA-SBA sample, this difference in coordination environment was assigned to Sc interacting with the CA ligand.

To further probe the Sc interactions with the CA-SBA material, ^{1}H spectra were collected for both the pre-conditioned (Figure 6.18a) and the Sc-CA-SBA (Figure 6.18b) samples. In comparing these two spectra, a peak unique to the Sc-CA-SBA sample is observed at 4.3 ppm that is attributed to the presence of inner sphere waters on the Sc ion. This water is associated with Sc and not simply relic physisorbed water on the bare surface as evidenced by the lack of a peak at this chemical shift for the preconditioned sample. The 3.9 ppm peak in the preconditioned sample is attributed to isolated silanols on the silica surface, [147] however, an additional contribution to this resonance may be the rapid exchange of water with the silanols. [148] The peak at 4.3 ppm is a new peak that is broader due to overlap with the 3.9 ppm peak present in both samples. As with the preconditioned sample, the additional waters due to hydration of the Sc in the Sc-CA-SBA sample, are also likely in rapid exchange with the surface. [148] The remaining chemical shifts of the Sc-CA-SBA ^{1}H spectrum are assigned based on a ring opened molecule. The resonances of the CH_2 protons adjacent to the nitrogen and farther from the nitrogen are expected to be δ_H = 3-4 ppm and δ_H =0.5-2.5 ppm, respectively. Protons on the surface silanols are expected to have a shift of δ_H = 5-6.5 ppm.

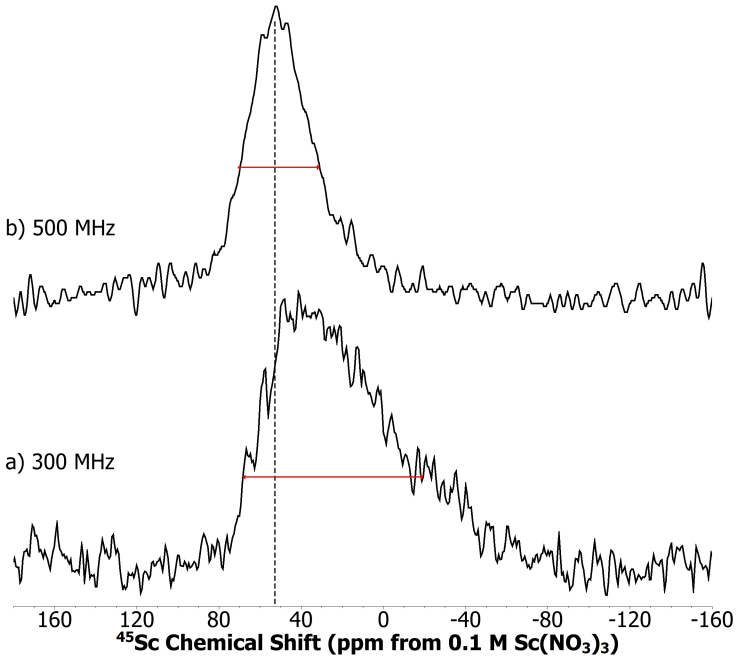

Figure 6.17: ^{45}Sc SP/MAS NMR spectra of solids from Sc sorption to CA functionalized SBA-15 (Sc-CA-SBA) on a) the 300 MHz spectrometer and b) the 500 MHz spectrometer. The chemical shifts for 6, 7, and 8-coordinated Sc occur in the ranges of δ_{Sc}= 100 to 160 ppm, δ_{Sc}= 10 to 70 ppm, and δ_{Sc}= -10 to -50 ppm, respectively

In order to determine the association of the proton species with the sorbed Sc we performed ^{1}H{^{45}Sc} TRAPDOR NMR spectroscopy on the Sc-CA-SBA sample (Figure 6.19). The experiment proceeds by first collecting a ^{1}H spin echo 'control' spectrum (Figure 6.19a) that contains the unmodified intensity of all the ^{1}H species present in the sample. This 'control' spectrum is compared to that of the ^{1}H{^{45}Sc} TRAPDOR experiment (Figure 6.19b) that presents a loss in signal for all ^{1}H species that are coupled to ^{45}Sc in the sample. This comparison allows us to determine which protons in the solid are associated with the Sc. We observe a decrease in the intensity of the proton resonances from δ_H = 4.3-7.5 ppm as well as that at δ_H = 4.0 ppm in the TRAPDOR spectrum compared to the control. This result indicates that the Sc is correlated strongly with the surface silanols and the water molecules on the Sc molecule, further confirming their presence in the inner sphere of the Sc atom. Based on the structure of the ligand, the metal cation can only coordinate to the carbonyl oxygens. In this conformation, the next nearest ligand proton would reside at a minimum of about 3 Å from the Sc, which is too distant for the correlations observed in this TRAPDOR experiment.

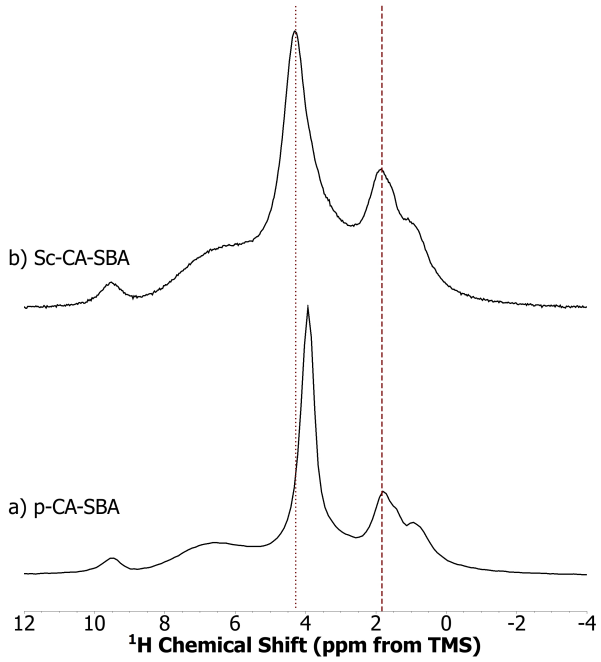

Figure 6.18: ^{1}H SP/MAS NMR spectra of a) pre-conditioned CA functionalized SBA-15 (p-CA-SBA) and b)solids from Sc sorption to CA functionalized SBA-15 (Sc-CA-SBA). The dotted line highlights the H_2O peak present in the Sc-CA-SBA sample and the absent in the p-CA-SBA sample. The dashed line highlights that the -CH_2 groups have not shifted.

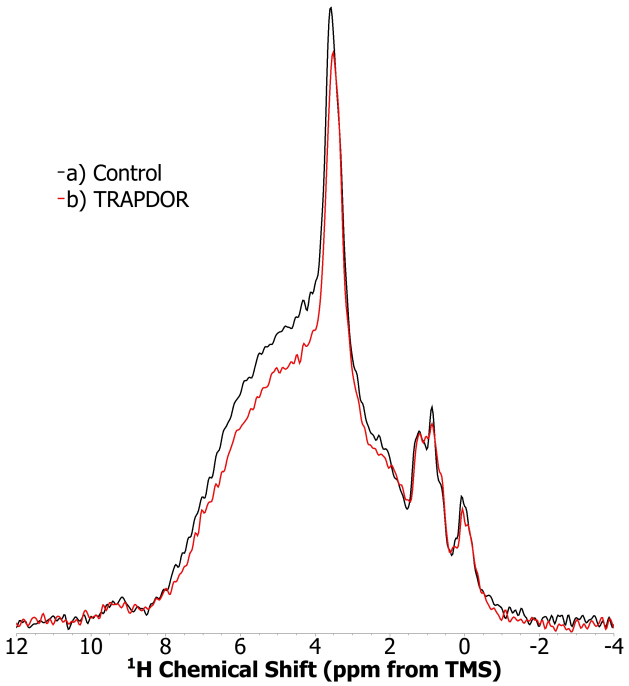

Figure 6.19: ^{1}H{^{45}Sc} NMR spectra of a) control (black) and b) TRAPDOR (red) spectra of solids from Sc sorption to CA functionalized SBA-15.

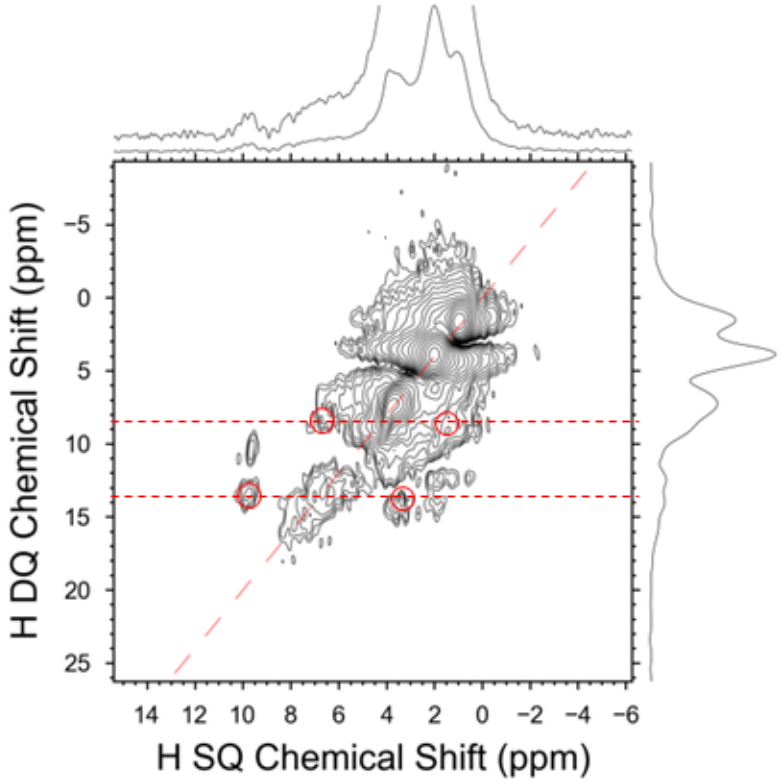

Figure 6.20: ^{1}H DQ correlation spectra of solids from Sc sorption to CA functionalized SBA-15. Positions of the 13.2 and 8.3 ppm DQ cross peaks are highlighted in red circles. ^{1}H chemical shift relative to external standard hydroxylapatite with the hydroxyl resonance at 0.2 ppm. This plot was made by Harris Mason.

The results of the TRAPDOR experiment only provide information that the Sc is interacting with the surface of the CA-SBA, and further experiments utilizing ^{1}H DQ correlation experiments can be used to further constrain the structure of the coordinating ligand and to determine if it interacts with the surface silanol protons. These results produce a map of the through-space correlations between proton species (Figure 6.20). At the short mixing time used, the chemical shifts in the DQ dimension occur at the linear combination of the single quantum chemical shifts, and represent only the closest associations between the two ^{1}H species.

The results clearly show strong associations between the -CH_2 groups on the chains but additional contours in the DQ dimension at 13.2 and 8.3 ppm reveal unique interactions of the amide and silanol functional groups, respectively. The DQ correlation at 13.2 ppm results from a correlation between the amide and its next adjacent proton at $\delta_H = 9.5$ ppm and $\delta_H = 3.7$ ppm, respectively. This result illustrates that for such correlations to occur these protons must be in close association (< 3.5 Å) [149] with one another. The DQ shift of $\delta_H = 8.3$ ppm results from a close association between the protons represented by SQ shifts of of $\delta_H = 6.7$ ppm and $\delta_H = 1.5$ ppm. This correlation is assigned to that between the surface silanols (6.7 ppm) and a ligand CH_2 group $\delta_H = 1.5$ ppm, indicating that the ring opened ligand is bent towards the surface near the silanols, therefore also interacting with the Sc associated with the surface. Similar ligand interactions with

a silica surface were previously observed with molecules terminating in trimethylamine. [148]

Based on the combined results from the SP/MAS, TRAPDOR, and DQ correlation experiment, a mechanism of Sc(III) interaction with the CA-SBA material can be proposed. The Sc(III) appears to be simultaneously coordinating with the silanols on the SBA-15 surface and the carbonyls of the CA ligand . Based on the bidentate CA ligand occupying two sites on the coordination sphere of the Sc, and the silanols occupying two to three additional sites, there are most likely 2-3 waters in the inner coordination sphere of each Sc ion. The width of the ^{45}Sc SP/MAS resonance, the decrease in proton intensity at δ_H = 4.3-7.5 ppm and δ_H = 4 ppm in the TRAPDOR experiment, and the correlation between the silanol protons and the ligand CH_2 protons in the DQ experiment combine to support that Sc(III) is coordinated with the ligand, silanols, and water molecules simultaneously.

A desorption experiment on the Sc-CA-SBA sample analogous to that performed on the Al-CA-SBA sample was carried out. A ^{45}Sc SP/MAS NMR spectrum was collected on the desorbed sample (d-Sc-CA-SBA, Figure 6.21b) and no change was observed relative to that of the Sc-CA-SBA (Figure 6.21a). It is believed that this is because the Sc is already hydrolyzed during the initial sorption to the CA-SBA at pH 3. Above pH 2, hydrolysis of Sc has been observed, and at the concentrations of Sc used in this experiment, precipitation of ScOOH (s) is expected above pH 3.8. [150] However, based on the results of the ^{45}Sc spectrum, it is clear that there is still a substantial amount of Sc if not all of it remaining on the CA-SBA. Based on this result, within the timescale of this desorption experiment, Sc interactions with the ligand and the silanols are favored over precipitation.

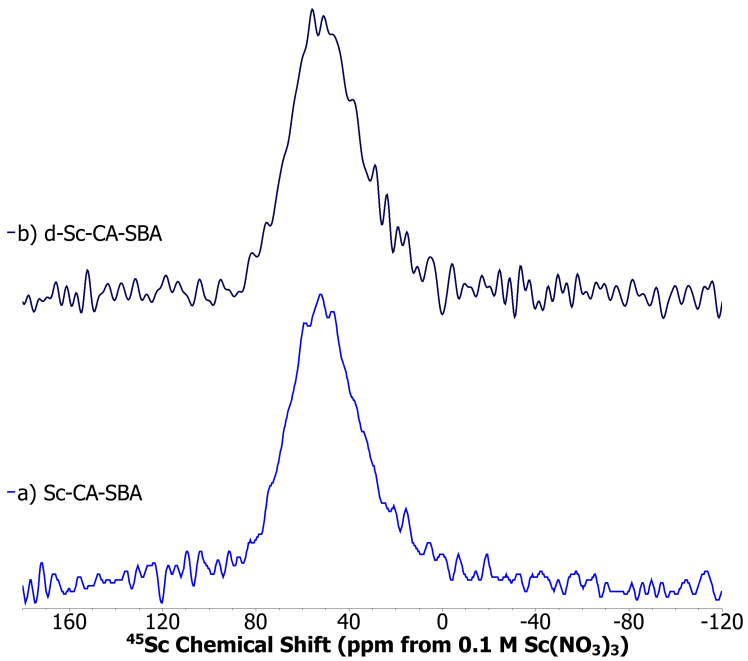

Figure 6.21: ^{45}Sc SP/MAS NMR spectra of solids from Sc sorption to CA functionalized SBA-15 a) before (Sc-CA-SBA) and b) after contact with water for desorption (d-Sc-CA-SBA). Spectra collected on 500 MHz spectrometer.

6.7 Discussion

Acid hydrolysis studies on CA-SBA indicate that CA functionalized SBA-15, is not completely stable in aqueous environments and that even in the presence of dilute (pH 3) nitric acid significant degradation of the ligand occurs. The results from the ^{13}C NMR indicate opening of the seven-membered ring on the ligands that remain attached to the silica. This mechanism allows the ligand to obtain a less sterically-hindered conformation for complexing metals. However, the resulting ligand may then be susceptible to further acid degradation and the rate of diffusion of metals through the pores may decrease if the chain is long enough to clog pores. It was also observed that occasionally complete detachment of the ligand can occur at the silane anchor on the silica surface, as evident by the ^{29}Si spectra. However, this partial retention of the ligand on the surface allows one to postulate the coordination environment of the metal complex. The observed ligand degradation in pH 3 nitric acid suggests that it is important to examine the characteristics of functionalized materials both before and after contact with acid as the actual pre-conditioned surface that contacts the metal may be different than the pristine material.

Batch sorption experiments with Eu(III) indicate that the CA-silica materials have a low affinity for this ion. A variety of conditions including a range of acidities (pH 3 to 1 M HNO_3), high and low ionic strength, and elevated temperature were all examined, however had minimal impact on Eu uptake. While temperature increased sorption by a very small amount, the fact that this did not greatly enhance the complexation indicates that the low uptake was not only a result of poor thermodynamics. While a number of different pore sizes and two types of pore morphologies were studied, no trends were observed as there was little to no Eu uptake. To truly understand the effect of pore diameter, pore shape, and functionalization method, a metal with higher sorption should be used. While Al and Sc both had higher uptake than Eu on the CA-SBA material, it was determined that they were interacting strongly with the surface. Ideally, for a solid-phased extractant destined for use in separations, the metal should only be sorbing to the ligand and not the surface to maintain more controlled behavior.

The behavior of Al and Sc on the CA-SBA and on the bare SBA differed in their coordination. Al(III) showed two different types of coordination when contacted with the CA-SBA, however, only one type of coordination on the bare SBA-15. This is indicative that one of the two sites present on the functionalized material is the Al(III) bound to the silica surface and the other interacted with the ligand. The Sc(III), however, primarily binds with a coordination number of seven both for the bare SBA-15 and the functionalized SBA-15. The functionalized sample, however, has a broader ^{45}Sc peak which is attributed to a more disordered structure caused by Sc coordination with the ligand. It was confirmed that the Sc was complexing with the surface silanols and water molecules using $^{1}H\{^{45}Sc\}$ TRAPDOR NMR spectroscopy supported by a ^{1}H DQ correlation experiment. Through the desorption experiment with Al (III) on CA functionalized SBA-15, it was determined that Al can be easily desorbed from the functionalized silica. The ability to desorb a species is important for any material that will be used as an extraction chromatography material. Unlike Al however, Sc could not be desorbed from CA-SBA under the same conditions. This means that under these conditions, if Al and Sc were both sorbed to CA-SBA, Al could be selectively removed, isolating Al from Sc.

In the absence of detailed characterization, such as the NMR work presented in this chapter, macroscopic batch metal sorption experiments to functionalized solids cannot differentiate between metal sorbed to ligand sites or residual surface sites. The difference between an interaction with the surface versus with the ligand, however, can have major implications for the efficacy of

the materials in either chromatography or catalysis applications. In the case of the CA ligand the metal interacts with the ligand via the carbonyls in a coordination complex. If, however, the cations sorb to the surface, they either form ionic bonds with deprotonated silanols or interact via Van der Waals forces with the lone pairs on the silanol oxygen. The strength of these interactions cannot be postulated based on the results presented here but the difference will likely affect a potential separation or catalyst application. Here it has been shown that these cations can form multiple types of complexes with a material, and it likely that each complex will have different stability constants and, in turn, will behave like multiple distinct species in a single separation. At low pH values, metal-silanol interactions are often assumed to be minimal due to the metal speciation and protonated state of the surface. The results presented here show that these interactions cannot be ignored as they are a predominant mechanism in the system.

Multinuclear solid-state NMR provided unique insights into the interaction of metal nuclei with an organically modified silica surface. Based on these results, however, it was also determined that the CA ligand may not be the most suitable for the desired applications. Beyond the immediately problematic issue of ligand degradation, the observation that the Sc(III) and Al(III) interact with both the silica surface and the ligand is also problematic because this limits the ability to tune the material selectivity via ligand characteristics. Ideally, the organically-modified silica would have a ligand that forms a strong enough complex with the metal ion that the interactions with the silica surface are negligible. Future work towards improving upon this material will incorporate ligands that complex the metal more strongly and are less susceptible to acid hydrolysis.

6.8 Conclusions and Outlook

Al(III) and Sc(III) sorb to N-[5-(trimethoxysilyl)-2-aza-1-oxopentyl]caprolactam functionalized mesoporous silica via interactions with both the surface and the ligand. Eu(III), however, has minimal sorption to the same material. The 7-membered ring opens during the acid preconditioning, making it a less sterically hindered molecule. The acid hydrolysis experiments also indicated that higher order polymerization of the ligand can stabilize the material towards acid. By probing not only the metal nuclei, but also carbon from the ligand, and silicon from the surface, we obtained a better understanding of how metals complex to this functionalized silica. While Al(III) and Sc(III) interact with the surface and the ligand, Al changes coordination number based on whether it is complexing with the ligand, while Sc maintains the same overall coordination number in both cases. Based on the results from this study, the Al(III) and Sc(III) both only utilize one CA ligand and then the participation of the silanols for complexation. As Eu(III) does not interact with the silanols on the silica at pH 3, the same cooperative surface-ligand binding was not possible. Thus, the lack of Eu(III) binding seems to be a combination of the metal size and requirement for additional ligands for complexation as well as the low affinity for a SiO_2 surface in the pH range studied. While understanding the quantity of metals sorbed to these materials is important, it is also necessary to examine the binding mechanisms and fundamental chemistry to most effectively develop new materials. NMR spectroscopy has proved to be a useful tool for studying these mechanisms.

Chapter 7

Interactions of Trivalent Cations with Diglycolamide Functionalized Mesoporous Silica

This chapter presents the studies on diglycolamide-modified mesoporous silica. As with the CA material, SBA-15 type mesoporous silica was used as the solid support. Organically-modified mesoporous silica has been previously synthesized and utilized for lanthanide and actinide sorption utilizing a variety of ligands. [17, 64–66, 79, 132, 151, 152] Diglycolamic acid modified silica substrate have also been studied for lanthanide and actinide uptake. [153,154] Diglycolamide (DGA) ligands have a similar binding site to the neutral diamide extractants that have been shown to bind trivalent lanthanides and actinides effectively from highly acidic matrices, especially when pre-organized. [155, 156] Similar to diamides, diglycolamide ligands are composed of only carbon, hydrogen, oxygen, and nitrogen (CHON), therefore they are completely incinerable at end of use. DGA ligands have been shown to efficiently extract trivalent actinides and lanthanides from highly acidic ($>$ 1 M) nitric acidic feeds in the nuclear fuel cycle using solvent extraction. [157–161] DGA has been found to form aggregates in high concentrations of nitric acid that have a high affinity for the trivalent lanthanides and actinides. [162, 163] As Chavan et al discuss, [164] due to this aggregation, preorganization of the DGA on a solid support would result in a more efficient extraction of Am(III) and Eu(III) than can be achieved with a liquid-liquid system. In the case of diglycolamide-modified mesoporous silica, pre-organization of the ligands is done through ligand polymerization during functionalization. Formation of DGA aggregates after contact with nitric acid, as discussed in liquid-liquid systems, [164, 165] is not expected because of the covalent bond between the ligand and the silica surface. DGA has been made into a resin by coating it on polymer supports, and is now commercially available. [3, 23, 27, 166, 167] Some work has been done immobilizing DGA on solid supports via impregnation. [24–26] Recently DGA ligands were covalently bound to silica supports for actinide and lanthanide sorption. [28, 29] Those materials were found to have lower Kd and capacities values for Eu(III) compared to the SPEs with coated DGA, [3, 27] and the authors attribute this to their low ligand loading compared to the other materials. [28,29] Additionally, their materials have multiple amide linkages that can be susceptible

to protonation and subsequent hydrolysis. In our current work, we use a different variant of the DGA ligand as well as a different anchor both of which minimize sites that can be protonated. We aim to take advantage of the stability of these grafted solid-phase extractants, but improve upon them by utilizing high surface area mesoporous silica and covalently binding the DGA ligands to the surface to achieve higher ligand loading and in turn greater extraction efficiency.

Additionally, the investigation into the complexation of the trivalent lanthanides and Am(III) withe the DGA modified silica was done using a variety of spectroscopic techniques including IR, NMR, XAS, and Eu fluorescence. There were two primary goals of these spectroscopic studies. First, it was important to confirm that the metal was actually interacting with the ligand through the expected binding site of the two carbonyl and the ether oxygens. The second goal was to elucidate the composition of the inner sphere of the metals and determine whether it was the same as observed in liquid-liquid systems and if there was participate from the chloride or nitrate counter-ions.

7.1 DGA Functionalized Mesoporous Silica

7.1.1 Synthesis

The DGA ligand was a 4:1 mixture of N,N-(dipropyl)-N(methyl), N(3-[trimethoxysilyl] propyl)-3-oxapentane diamide (Figure 7.1) and N,N-(dipropyl)-N(methyl), N(3-[monoethoxydimethoxysilyl] propyl)-3-oxapentane diamide (Technocomm). The DGA ligand was grafted to the silica surface using a solution polymerization technique discussed in Section 4.3. The DGA ligand mixture was used as opposed to a single species because of the difficulty in separating these constituents. Significantly greater purification beyond what was obtained would have resulted in too great a loss of the desired product. Additionally, the mixture should not affect synthesis as the methoxy-groups will still more readily attach to the surface so the anchor length will remain constant.

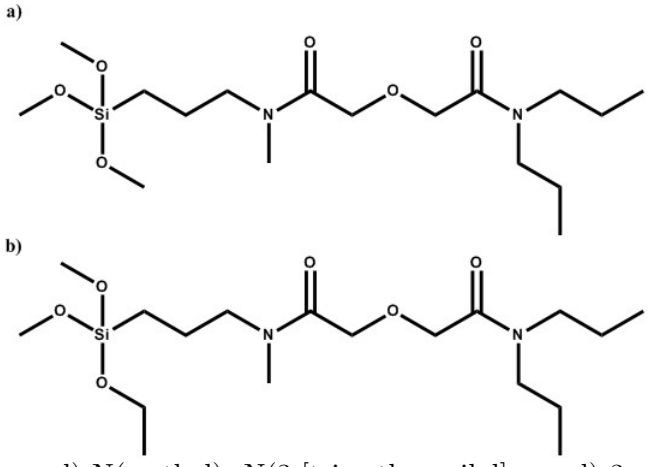

Figure 7.1: a) N,N-(dipropyl)-N(methyl), N(3-[trimethoxysilyl]propyl)-3-oxapentane diamide and b) N,N-(dipropyl)-N(methyl), N(3-[monoethoxydimethoxysilyl] propyl)-3-oxapentane diamide. The DGA mixture used in the synthesis was a 4 to 1 ratio of a to b.

7.1.2 Characterization

The SEM micrograph of the silica particles indicate that their average shape is spherical. Based on the BET analysis of the nitrogen adsorption (Figure 7.2), the SBA-15 mesoporous silica used as the solid support was found to have a surface area of 830 m^2/g. The pore diameter was found to be 7.5 nm. After functionalization, the surface area was found to be 397 m^2/g with a pore diameter of 5.5 nm.

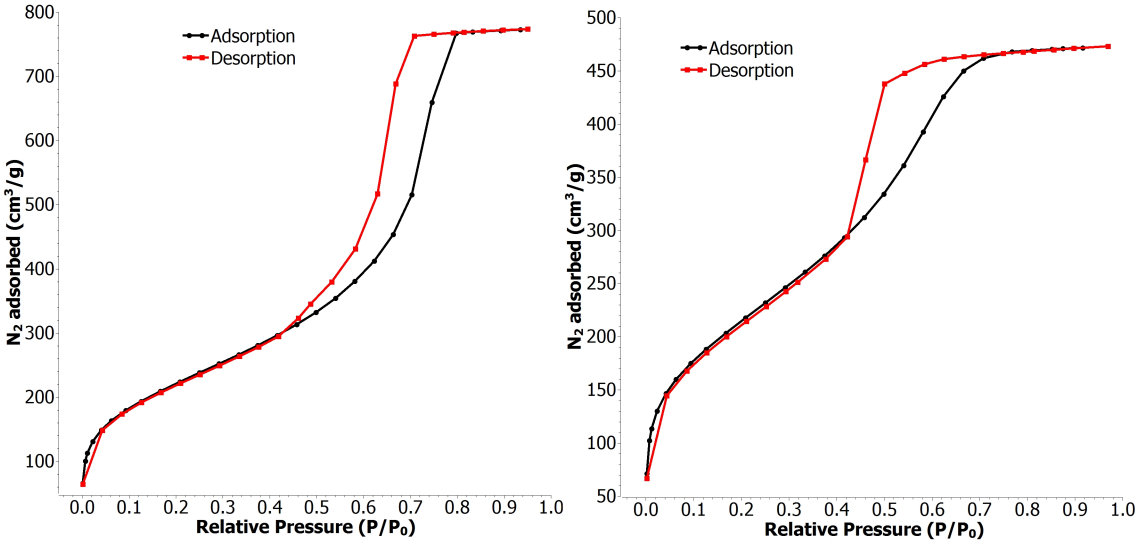

Figure 7.2: Nitrogen adsorption (black)/desorption (red) isotherms of bare SBA-15 (left) and pristine DGA-SBA (right)

Based on the mass loss measured in the TGA (Figure 7.3), the ligand loading per gram of the DGA-SBA was 848 ± 8 μmol g^{-1}. Ligand loading was calculated using a weighted average of the molecular weights of the trimethoxy- and dimethoxymonoethoxysilane attachments on the DGA ligand. The total observed mass loss was 28% of the original mass. The molecular weight of the ligand mixture used for the calculation accounted for the 4:1 mixture of the trimethoxy:dimethoxy,monoethoxy constituents. The ligand density was calculated assuming full combustion of C, H, N, and O components of the ligand, which means that this number is a minimum ligand density.

All of the IR spectra contain the characteristic absorption bands for silica at 1070, 965, 805 cm^{-1} corresponding to the symmetric Si-O-Si stretch, the Si-O stretch of surface silanols, and the anti-symmetric Si-O-Si stretch, respectively. In comparing the pristine DGA-SBA (Figure 7.4b) to the non-functionalized SBA (Figure 7.4a), there is a stretch at 1640 cm^{-1} due to the amide carbonyl stretches of the DGA ligand.

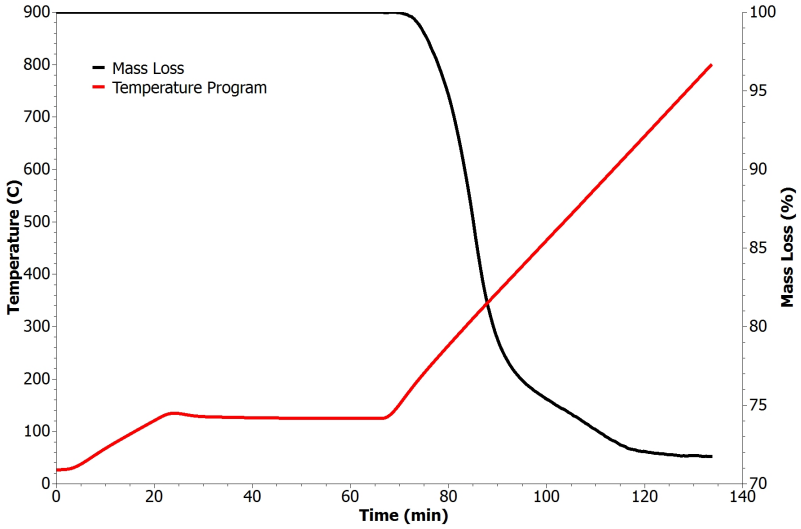

Figure 7.3: Thermogravimetric analysis of pristine DGA-SBA. The temperature program used is plotted against the primary y-axis and the percentage mass loss is presented on the secondary y-axis.

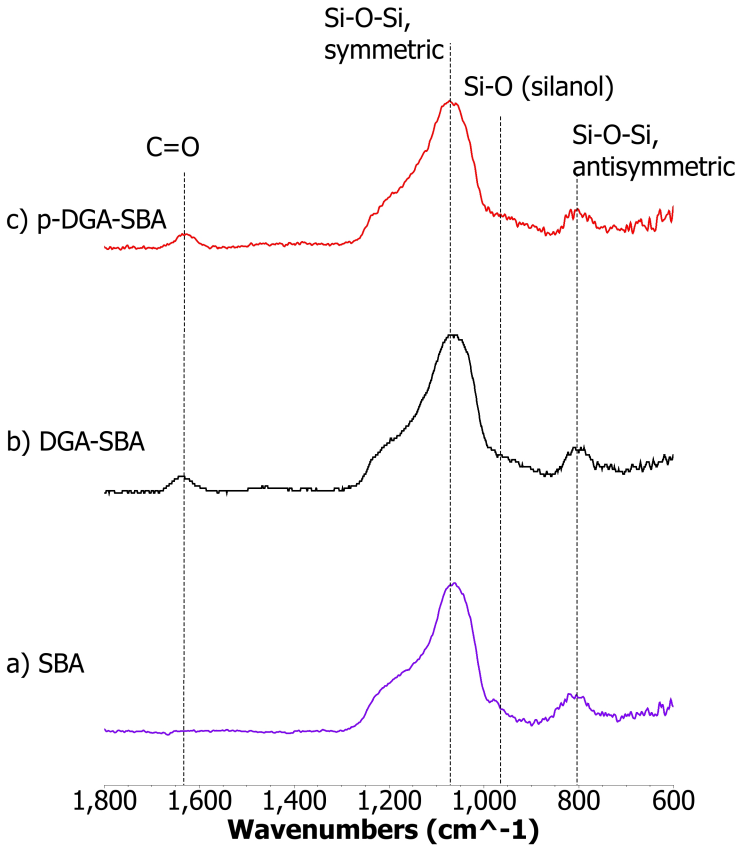

Figure 7.4: Infrared spectra of a)bare SBA-15 type silica, b) DGA modified SBA-15, DGA-SBA, c) 1 M HNO_3 contacted DGA-SBA, p-DGA-SBA, and d) Eu contacted DGA-SBA, Eu-DGA-SBA

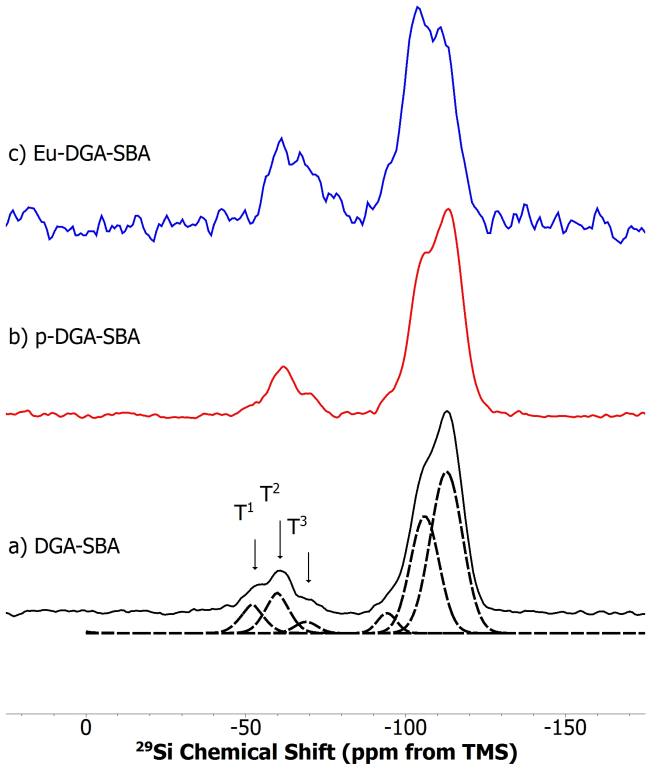

Figure 7.5: $^{29}Si\{^{1}H\}$ CP/MAS NMR spectra of a) pristine DGA modified SBA-15, DGA-SBA, b) 1 M HNO_3 contacted DGA-SBA, p-DGA-SBA, and c) Eu contacted DGA-SBA, Eu-DGA-SBA. Fits of DGA-SBA with pseudo-Voigt functions indicated with dashed lines directly below the DGA-SBA data.

The $^{29}Si\{^{1}H\}$ CP/MAS NMR spectrum of the pristine solid contained six resonances (Figure 7.5a); three were associated with the bulk silica material (Q species, δ_{Si} = -92 to -112 ppm) and three with silicon atoms bound to ligands on the surface (T species, δ_{Si} = 50 to -70 ppm). The Q^n species are defined as $Si(OSi)_n(OH)_{4-n}$ and the T^m species are similarly defined as $SiR(OSi)_m(OH)_{3-m}$. For bare, non-functionalized silica, the $^{29}Si\{^{1}H\}$ CP/MAS spectrum only contains Q peaks, so the presence of T peaks indicates that the ligand was covalently bound to the silica surface. T^1 (δ_{Si} = 51 ppm) peaks are a result of ligand monomers on the surface. T^2 (δ_{Si} = 58 ppm) peaks are from Si atoms bound to terminal ligands in a polymer chain, whereas T^3 (δ_{Si} = 68 ppm) peaks are from the Si atoms bound to central ligands in the polymer chain. From this spectrum, it is clear that all three species are present. Ideally, the material would be primarily composed of T^2 and T^3 species, indicating polymerization of the ligands. Ligand polymerization is important for complexation with the DGA ligand, as 2-3 ligands are necessary to complex the Ln(III) or An(III) depending on the specific metal. The $^{13}C\{^{1}H\}$ CP/MAS NMR spectrum again contains six distinct resonances (Figure 7.6a). The presence of the resonances at δ_C= 167 ppm (C=O), δ_C= 66 ppm (C-O), and δ_C= 7.2 ppm (-CH_3) , are evidence that the ligand did not decompose during functionalization.

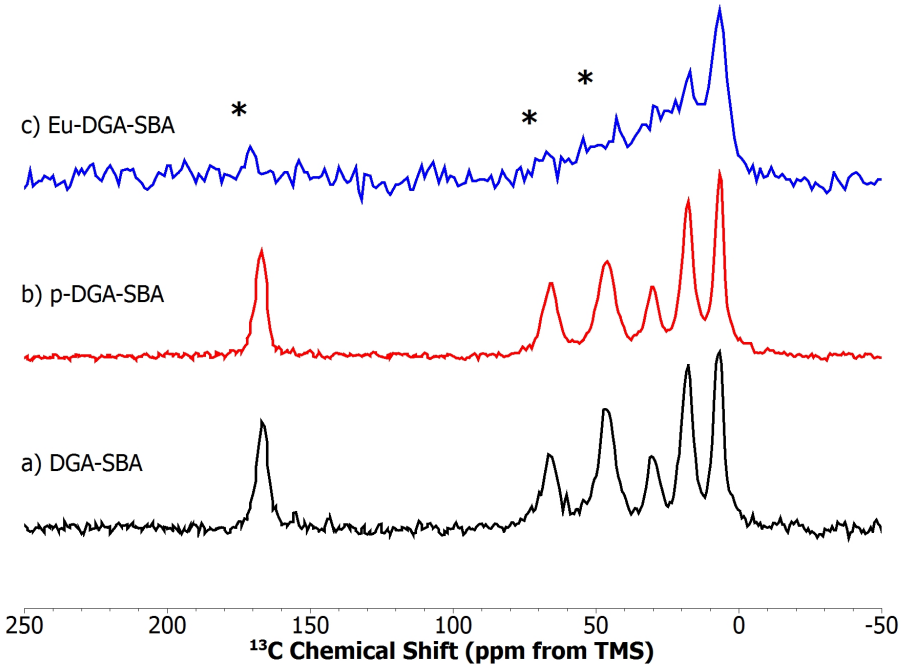

Figure 7.6: $^{13}C\{^{1}H\}$ CP/MAS NMR spectra of a) pristine DGA modified SBA-15, DGA-SBA, b) 1 M HNO_3 contacted DGA-SBA, p-DGA-SBA, and c) Eu contacted DGA-SBA, Eu-DGA-SBA

7.2 Acid Hydrolysis

The stability of DGA-SBA was examined by contacting the solid for one day with 1 M HNO_3 to simulate the conditions used for batch sorption experiments to achieve sorption. A $^{29}Si\{^{1}H\}$ CP/MAS NMR spectrum of the acid-contacted sample (Figure 7.5b) was collected and compared to the pristine material. While CP is inherently not quantitative, peak ratios of the T peaks can still be compared because the spectra were collected under identical conditions. [168] The T peaks were fitted with pseudo-Voigt functions and the ratios of their integrated peak intensities were calculated. The T^1:T^2 ratios decreased from 0.55 to 0.19 for the pristine compared to the acid degraded sample, respectively. The T^3:T^2 ratios for the pristine and acid degraded sample were 0.27 and 0.29, respectively. The proton spin-lattice relaxation time constants ($T_{1\rho,H}$) for the pristine material were compared to those of the acid-contacted sample because increased protons from the acid can alter the $T_{1\rho,H}$, and in turn, the relative peak intensities. As expected for organically-modified silica, the $T_{1\rho,H}$ values for the pristine and acid-contacted samples were similar, averaging 3.1 ms and 3.2 ms, respectively, which are the same within experimental error (Figure 7.7). As the $T_{1\rho,H}$ values were the same, the changes in T^1:T^2 ratios is due solely to cleavage of the ligand from the silica surface. The significant decrease observed in T^1:T^2 ratios and relative stability in T^3:T^2 ratios between pristine and acid-contacted samples indicate that the T^2 and T^3 species are not as highly affected by acid contact as T^1 species. The T^1 species substantially hydrolyzed from the surface. The stability of the T^2 and T^3 species relative to the T^1 species indicates that ligand polymerization may potentially help stabilize the functionalized materials to acid-catalyzed hydrolysis.

A $^{13}C\{^{1}H\}$ CP/MAS NMR spectrum of the acid-contacted sample (Figure 7.6b) was collected and compared to the $^{13}C\{^{1}H\}$ CP/MAS NMR spectrum of the pristine sample. There is no substantial difference between these two spectra, indicating that after one day of contact with 1 M HNO_3, the ligand does not decompose. While the $^{29}Si\{^{1}H\}$ CP/MAS NMR spectra indicate cleavage of the isolated ligands on the surface, the polymerized ligands remained grafted, and based on the $^{13}C\{^{1}H\}$ CP/MAS NMR spectra, it is clear that the ligands remained intact. The IR spectra of the pristine DGA-SBA (Figure 7.4a) and the acid-contacted DGA-SBA (Figure 7.4b) are nearly identical, which agrees with the results from the NMR spectroscopy indicating that the ligand remains intact after acid-contact.

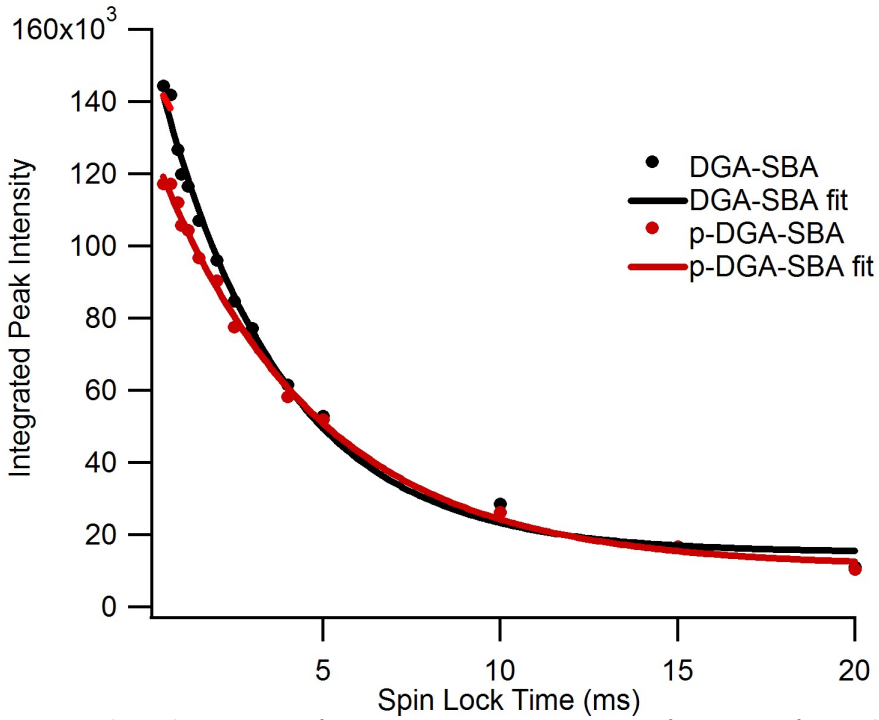

Figure 7.7: Integrated peak intensity for 3.2 ppm resonance as a function of spin lock duration for determination of $T_{1\rho,H}$ for the pristine (DGA-SBA) and acid-contacted DGA-SBA (p-DGA-SBA).

7.3 Batch Sorption Experiments

7.3.1 Eu and Am Sorption in HNO_3 and HCl

Sorption kinetics

The kinetics of Eu and Am sorption to DGA-SBA in 1 M HNO_3 were examined in batch sorption style experiments (Figure 7.8). The results indicate that Am (Figure 7.8a) reaches equilibrium after approximately 42 minutes, whereas Eu (Figure 7.8b) does not reach equilibrium until it has contacted with the solid for almost 2 hours. The Am and Eu data fit nicely to a pseudo-second-order rate model (Figure 7.9) with rate constants presented in Table 7.1.

Cation	k_2q^2 mg $g^{-1}min^{-1}$	k_2 g $mg^{-1}min^{-1}$	q_e mg g^{-1}	R^2
Eu(III)	0.15	0.077	1.4	0.9991
Am(III)	0.43	0.14	1.7	1.000

Table 7.1: Kinetic parameters from pseudo-second-order kinetic fit of Am(III) and Eu(III) sorption on DGA-SBA in 1 M HNO_3. Metal ion concentrations were 8 μM and 10 μM for Am(III) and Eu(III), respectively.

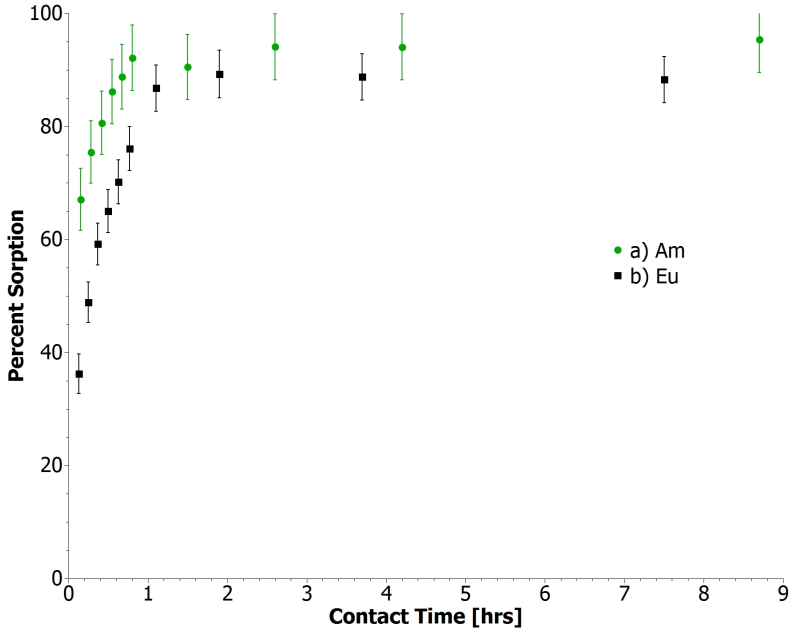

Figure 7.8: Batch uptake kinetics for a) Am(III) and b) Eu(III) on DGA-SBA in 1 M HNO_3. Concentrations of Am and Eu were 8 μM and 10 μM, respectively.

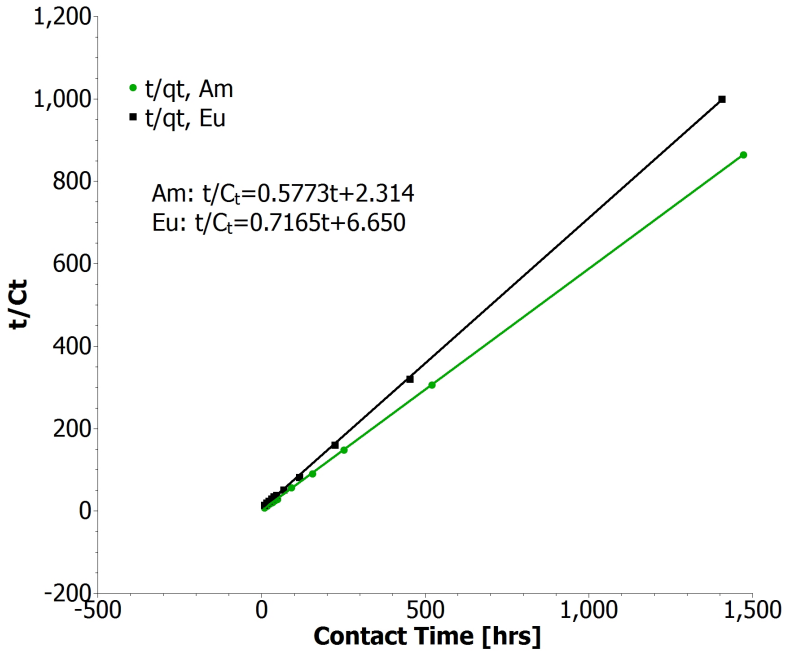

Figure 7.9: Pseudo-second-order rate model fit for batch uptake kinetic data for Am(III) and Eu(III) on DGA-SBA in 1 M HNO_3. Concentrations of Am and Eu were 8 μM and 10 μM, respectively.

Sorption as a function of pH and ionic strength

The equilibrium uptake of Eu(III) and Am(III) by DGA-SBA was studied as a function of nitric and hydrochloric acid concentration. The concentrations of nitric and hydrochloric acids were controlled by molarity for the 3 M and 1 M samples and by pH adjustments for the pH 1-4 samples. Results of these experiments, after approximately 3 hrs of reaction time, are presented in Figure 7.10. Complete uptake of Eu and Am by DGA-SBA was observed in 0.1 M, 1 M, and 3 M HNO_3 solutions. As discussed previously, equilibrium is reached in less than three hours under the conditions where full uptake occurs, so the sorption data at this time point compared to the 24 hour contact data is the same within error. However, at higher pH values, there is not full uptake of either Am or Eu and the samples do not reach equilibrium within 3 hours. Sorption decreases substantially at higher pH with 60% sorption at pH 2 and 3, and only 40% at pH 4 after 24 hours of contact for Eu. After the same contact time, 78%, 51%, and 45% of the Am sorbs to the DGA-SBA at pH 2, 3, and 4, respectively. The corresponding K_d values, however, are still quite high at all nitric acid concentrations tested (Table 7.2). Those for the highest nitric concentrations (for Eu, 3.2 x 10^4 and 1.5 x 10^4 for 1 M and 3 M HNO_3, respectively) agree well with the literature for similar materials.

The Eu exhibits similar equilibrium sorption behavior in HCl compared to that in HNO_3. A difference in sorption behavior, however, can be observed at pH 2 acid concentration where 63% $\pm$ 6% of the Eu sorbed in HCl relative to 35% $\pm$ 4% in HNO_3 at the same concentration. At 0.1 M, 1 M, and 3 M HCl, Eu sorption was identical to in HNO_3, which is nearly complete uptake from a 10 μm Eu solution. Interestingly, Am did not have as high of an uptake in HCl at concentrations of pH 2 and higher as Eu. At the very high acid concentrations tested, Am uptake never reaches 95-100%, as observed in HNO_3. At 0.01 M HCl, Eu has much higher uptake than Am, 63% 6% relative to 24% 6%, respectively. This could be a difference that can be utilized in a chromatographic

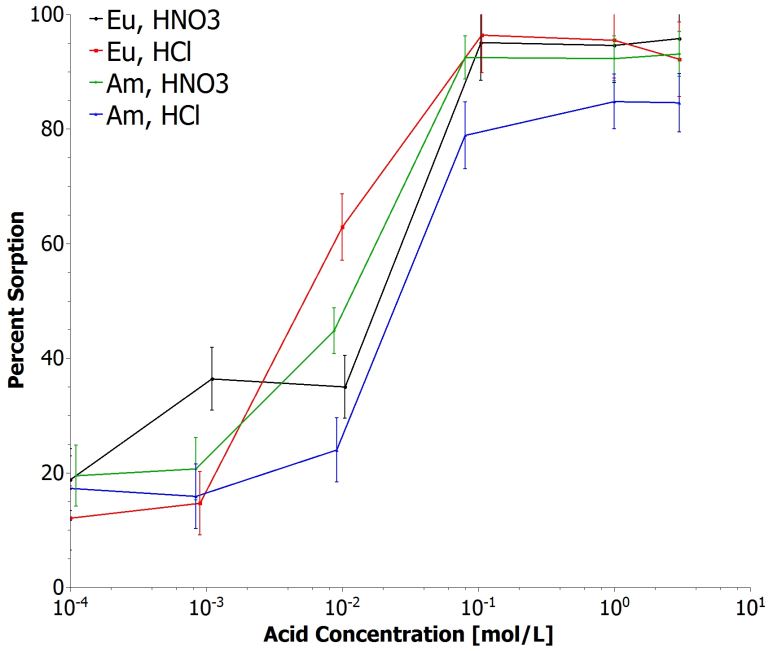

Figure 7.10: Batch uptake percent sorption of Am(III) and Eu(III) by DGA-SBA as a function of concentration of HNO_3 or HCl. Concentrations of Am and Eu were 8 μM and 10 μM, respectively.

separation. In terms of K_d values, that correlates to 2.8 x 10^3 (Eu) and 7.4 x 10^2 (Am) after 24 h of metal-solid contact time, which results in a separation factor of Eu to Am of 3.8. Separation factors at equilibrium derived from batch experiments, however, do not always accurately predict the separations that can be achieved in a chromatographic separation as the solid:liquid ratios and kinetics are significantly different in these two cases and column characteristics must be taken into account. [169] By combining the slightly different behavior in hydrochloric acid, especially at shorter contact times, a chromatographic separation of Am from Eu may be possible using DGA-SBA as a solid-phase. Future work will include testing the chromatographic potential of DGA-SBA.

At high ionic strength, the DGA-SBA sorbed greater than 93% of the Eu(III) at all acid concentrations tested (pH 4 to 3 M). These tests were performed in HNO_3 or HCl balancing the total NO_3^- or Cl^- concentration to 3 M with $NaNO_3$ or NaCl, respectively. There are a few potential explanations for increased sorption with increased ionic strength. First, the nitrate or chloride ions could be participating in the inner coordination sphere of the metal. Second, the high salt chloride or nitrate concentration may be required to form the neutral Eu-chloride or Eu-nitrate complex to be extracted by the DGA. Third, there could be an activity effect in which the high salt concentration in solution is driving the Eu to the area of lowest activity, the surface of the DGA-SBA. In the case of a diglycolamide, the formation of a neutral species is required for complexation, so this is likely the driving effect. The formation of an inner sphere complex was studied via fluorescence and X-ray absorption spectroscopy, which will be discussed in a later section.

Cation	Acid	Acid Concentration	pH	% Sorption	K_d [mL g^{-1}]
Eu(III)	HNO_3	3 M		94.1 ± 4.2	1.52×10^{4}
		1 M		96.3 ± 4.3	3.17×10^{4}
			0.98	99.8 ± 4.3	2.17×10^{5}
			1.98	61.9 ± 3.9	1.52×10^{3}
			2.97	65.6 ± 3.9	1.79×10^{3}
			3.95	41.2 ± 3.8	6.36×10^{2}
	HCl	3 M		93.9 ± 6.6	1.41×10^{4}
		1 M		96.3 ± 6.6	2.45×10^{4}
			0.98	98.6 ± 6.7	8.12×10^{4}
			2.00	75.5 ± 6.1	2.84×10^{3}
			3.04	18.1 ± 5.5	2.13×10^{2}
			4.01	18.2 ± 5.5	2.10×10^{2}
Am(III)	HNO_3	3 M		91.8 ± 4.3	1.19×10^{4}
		1 M		92.8 ± 4.4	1.31×10^{4}
			1.10	94.6 ± 3.8	1.67×10^{4}
			2.06	77.9 ± 3.7	3.41×10^{3}
			3.08	51.4 ± 4.0	1.01×10^{3}
			44.7	41.2 ± 4.7	7.68×10^{2}
	HCl	3 M		88.4 ± 5.0	7.33×10^{3}
		1 M		88.9 ± 4.8	7.74×10^{3}
			1.10	84.6 ± 4.7	5.39×10^{3}
			2.04	43.0 ± 5.7	7.37×10^{2}
			3.08	32.3 ± 5.2	4.64×10^{2}
			3.99	40.2 ± 5.0	5.92×10^{2}

Table 7.2: Batch sorption results of Eu(III) and Am(III) on DGA-SBA after 24 hours of metal contact time in HNO_3 and HCl. Metal ion concentrations were 8 μM and 10 μM for Am(III) and Eu(III), respectively.

Eu capacity

The capacity of DGA-SBA was determined for Eu(III) in 1 M HNO_3 (Figure 7.11). Based on the overall similar chemistry of Eu(III) and Am(III) in 1 M HNO_3, we expect that their uptake capacity will be similar under these conditions, and Eu is much less valuable than the ^{243}Am required for this measurement. For this experiment, stocks of varying Eu concentrations were added to samples of the same DGA-SBA mass and acid volume and concentration. From the concentration of Eu measured in the supernatant after 24 hours of contact, the capacity could be determined. Two different adsorption isotherm models, Langmuir (Figure 7.12) and Freundlich (Figure 7.13), were tested with the sorption data. For each of these, a linear regression was applied, and it was determined that the sorption was best described with a Langmuir isotherm. From the Langmuir fit, the capacity of the DGA-SBA for Eu(III) was found to be 379 μmol/g. As with any model, however, it is important to keep in mind the assumptions and limitations. The Langmuir model assumes a smooth surface and monolayer sorption. The Freundlich model, however, better accounts for a more heterogeneous surface. Based on the surface coverage of the ligand determined by TGA and the presence of T^1 species in the ^{29}Si{^{1}H} CP/MAS NMR spectrum, there is not a complete monolayer of ligand on the surface. The better fit of the Langmuir model compared

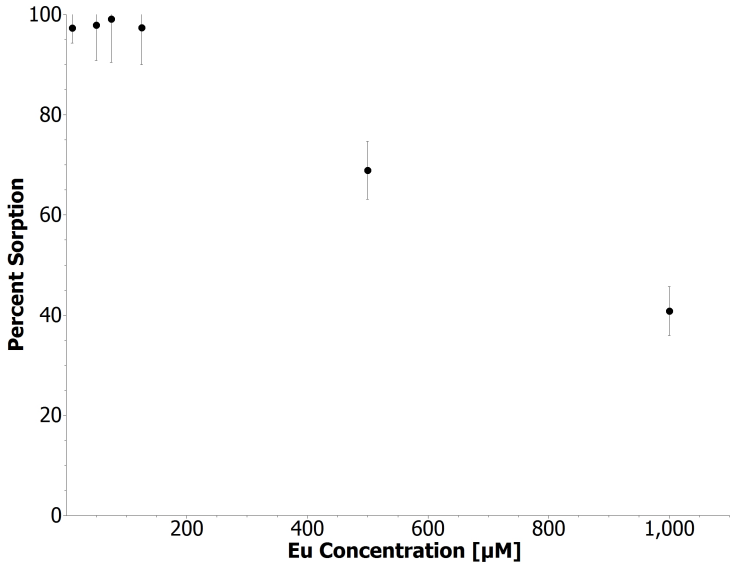

Figure 7.11: Batch uptake sorption capacity of Eu(III) by DGA-SBA in 1 M HNO_3.Eu(III) concentrations were varied from 75 μM to 1000 μM.

to Freundlich may indicate that the Eu is primarily interacting in areas of local, well-ordered monolayer formation. The Eu sorption capacities derived from the Langmuir model allowed for the determination of an approximately 2:1 average ligand:metal ratio based on the ligand coverage on the surface as measured by TGA. This ratio is lower than expected based on the spectroscopy results that will be discussed in later sections, but may be a result of the underestimate of ligand coverage provided by TGA.

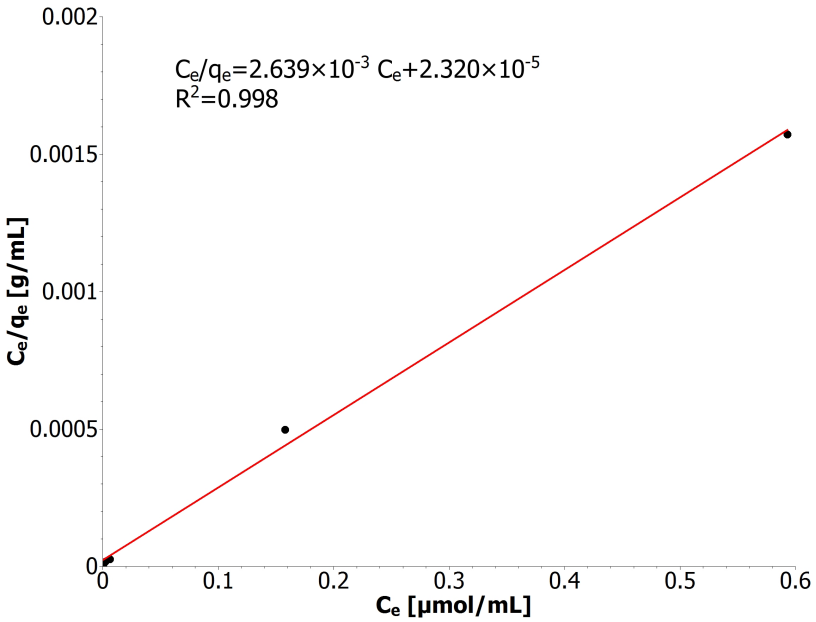

Figure 7.12: Langmuir isotherm for DGA-SBA capacity of Eu(III) by DGA-SBA in 1 M HNO_3. Eu(III) concentrations were varied from 75 μM to 1000 μM.

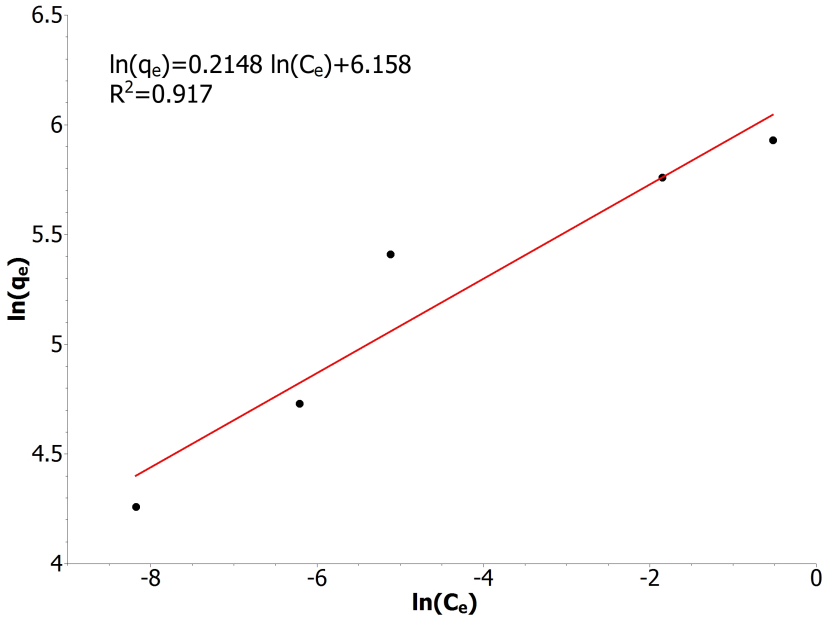

Figure 7.13: Freundlich isotherm for DGA-SBA capacity of Eu(III) by DGA-SBA in 1 M HNO_3. Eu(III) concentrations were varied from 75 μM to 1000 μM.

Eu and Am desorption

The desorption of Eu and Am that was sorbed to DGA-SBA in nitric acid was tested because of its importance in the processing of used nuclear fuel. Eu and Am sorbed to DGA-SBA was expected to effectively desorb in pH 4.5 HCl based on the observed trend in percent sorption as a function of HCl concentration. Due to the remaining 1 M HNO_3 left after decanting the supernatant of the sorption solution, pH 5.5 HCl was used as the rinse solution which resulted in a pH of the third rinse of 4.5. The initially rinse had a pH of approximately 1.5, raised to 3.5 with the second rinse, and finally 4.5 with the third rinse. While a final pH of 4.5 was desired, the pH was not adjusted on earlier rinses as this is a desorption method being tested for chromatographic separations. This desorption method was only moderately effective. For Eu, after two rinses with pH 5.5 HCl and 1 day contact, 31% of the metal was desorbed. Am desorption was similar with 33% Am removal after two rinses. It should be noted, however, that after three rinses, 65% of the Am was desorbed. To determine whether the especially low desorption in the first two rinses was due to the pH or nitrate presence, a comparison experiment was conducted where the pH was adjusted with NaOH to 4.5 with each rinse. The Am desorption was not significantly different from that observed with no pH adjustment, which points to a system dominated by nitrate concentration. While batch desorption with this method was not as effective as necessary for a separation (ideally >90% desorption), we expect that this would be much more successful in a chromatography experiment where the nitrate can be more effectively washed from the solid.

As expected based on the literature, [27, 29] EDTA was effective at completely desorbing Am from the DGA-SBA. While one rinse with 1 mM EDTA only removed 12% of the Am, a second rinse desorbed an additional 82% of the original Am, and the third rinse successfully removed the remaining Am. Similarly, desorption of Eu from the DGA-SBA using 1 mM EDTA was tested. The desorption of Eu with EDTA was not quite as successful as it was for Am, with a maximum of 80% of the Eu being removed after three rinses. The first and second rinses desorbed less than

10% and 75%, respectively. The lower overall desorption of Eu compared to Am may be indicative of a stronger Eu-DGA complex relative to the Am-DGA complex and agrees with the higher K_d observed for Eu compared to Am in 1 M HNO_3 (Table 7.2).

7.4 M-DGA-SBA Complexes

7.4.1 IR Spectroscopy

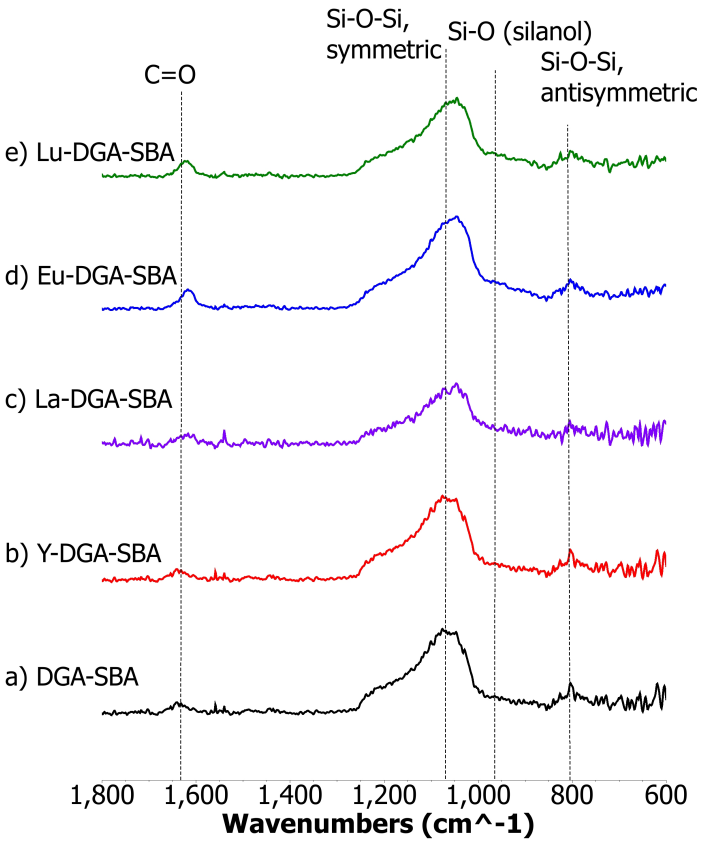

Figure 7.14: Infrared spectra of a) DGA-SBA, b) Y contacted DGA-SBA, Y-DGA-SBA, c) La contacted DGA-SBA, La-DGA-SBA, d) Eu contacted DGA-SBA, Eu-DGA-SBA, and e) Lu contacted DGA-SBA, Lu-DGA-SBA

IR spectroscopy was used to measure Ln-DGA-SBA complexes to determine 1) if the ligand decomposed due to metal contact, and 2) if the metal was complexing through the carbonyl oxygens. If the ligand decomposed, it would not be expected that the carbonyl oxygen stretch would still be present. However, if the carbonyls were complexing to the lanthanides, the stretch should still be present but shifted to a lower wavenumber indicative of lanthanide binding. In addition to La, Eu, and Lu bound to DGA-SBA, a Y sample was also measured as a rare earth lanthanide analogue.

The results of the IR measurement of the lanthanide and Y-DGA complexes indicate that the carbonyl stretch is still present, but shifted to lower wavenumber as anticipated (Figure 7.14). Recall that in the pristine and acid-treated DGA-SBA (Figure 7.4), the carbonyl stretch was at

1640cm^{-1}. For Y-DGA-SBA (Figure 7.14b) and Lu-DGA-SBA (Figure 7.14e), the carbonyl stretch shifted to about 1625 cm^{-1} compared to 1620 cm^{-1} for the La-DGA-SBA (Figure 7.14c) and Eu-DGA-SBA (Figure 7.14d). This shift indicates that the ligand is still present and intact, and that the Y, La, Eu, and Lu are coordinating through the carbonyls, as expected. [170] Additionally, the intensity of the symmetric Si-O-Si stretch at 1070 cm^{-1} decreased significantly in the Eu-DGA-SBA sample. This decrease may be indicative of a change in the linearity of the bulk silica. [171] One could imagine that prior to complexation the ligands on the surface can rotate and bend freely. However, upon two or more ligands complexing to a single M(III) atom, they lose much of their original rotational and bending freedom. Restraining the ligands through complexation could result in overall rigidification of the surface layers of the bulk silica.

7.4.2 NMR Spectroscopy

The complexation of Eu to the DGA-SBA was explored using ^{29}Si{^{1}H} and ^{13}C{^{1}H} CP/MAS NMR experiments (Figures 7.5c and 7.6c), respectively). Eu exhibits van Vleck paramagnetism, so in the ^{29}Si{^{1}H} and ^{13}C{^{1}H} CP/MAS NMR spectra, Si and C nuclei that are near enough to the Eu center to experience the influence of its paramagnetism will exhibit a change in their chemical shift and relaxation behavior. [172, 173] The Eu-DGA-SBA sample was pre-conditioned with 1 M HNO_3 prior to Eu addition and subsequent sorption for a 24 hour time period. The filtered, washed, and dried sample was then studied with NMR spectroscopy. In the ^{13}C{^{1}H} CP/MAS NMR spectra of Eu-DGA-SBA compared to p-DGA-SBA (Figures 7.6c and 7.6b, respectively), it is clear that the resonances at δ_C= 167, 66, and 46 ppm (marked by asterisks on Figure 7.6c) have decreased substantially with the addition of Eu. This is not just evidence of the ligand decomposing due to acid, as that would have resulted in these peaks also decreasing in the p-DGA-SBA. The carbons directly bound to the oxygen atoms are most affected as these are the closest to the binding site (carbonyl and ether oxygens). However, even carbons that were more distant from the binding site were impacted by the Eu, indicating that the paramagnetic influence could be extending beyond just a couple of angstroms. The remaining, most intense resonance at δ_C= 6.7 ppm, attributed to -CH_3 carbons, indicate that these carbons are distance from the Eu.

The ^{13}C NMR spectrum clearly confirms that the Eu is binding directly to the ligand. To determine if the Eu is also interacting strongly with the silica surface, a ^{29}Si{^{1}H} CP/MAS NMR spectrum was collected on the Eu-DGA-SBA (Figure 7.5c). The ^{29}Si NMR spectrum for the Eu-DGA-SBA still contains both T and Q peaks, and the T peak ratios are quite similar to those observed in the p-DGA-SBA. However, the Q^3:Q^4 ratio changed, which could be a result of Eu altering the CP kinetics of these peaks.

In similar aim to the IR spectroscopy studies, a Y-DGA-SBA sample was measured using ^{13}C{^{1}H} CP/MAS NMR spectroscopy (Figure 7.15) to verify that metal catalyzed ligand cleavage was not occurring. As ^{89}Y is diamagnetic, it should not have a substantial influence on the ^{13}C{^{1}H} CP/MAS NMR spectrum. It should be noted prior to discussion of the spectra in Figure 7.15 that the pristine DGA-SBA spectrum appears different than the one presented in Figure 7.6 because of changes that were made to the probe after it broke between the measurement time of these samples. Multiple samples were remeasured after probe repairs to verify that the changes were in fact just a reflection of the changes in the probe as opposed to changes in the materials. In comparing the Y-DGA-SBA sample to the DGA-SBA (Figures 7.15b and 7.15a, respectively), there is not a major difference in the resonances in each. Had the decrease in peak intensities observed in the Eu-DGA-SBA samples been due to metal catalyzed ligand cleavage, the Y-DGA-SBA sample should have shown similar decrease in the same higher chemical shift resonances.

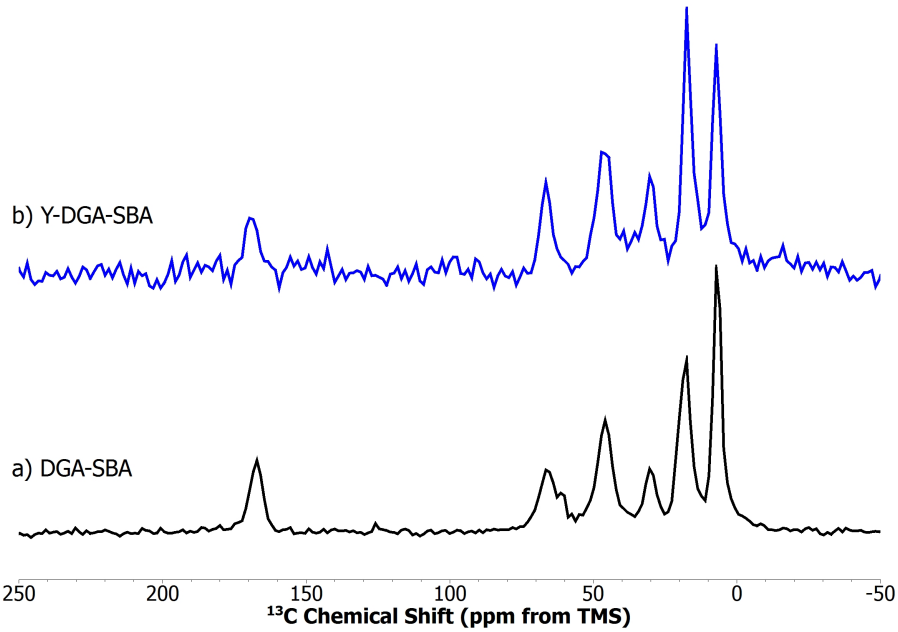

Figure 7.15: $^{13}C\{^{1}H\}$ CP/MAS NMR spectra of a) pristine DGA modified SBA-15, DGA-SBA, and b) Y contacted DGA-SBA, Y-DGA-SBA.

7.4.3 Fluorescence Spectroscopy

Fluorescence spectroscopy of DGA-SBA samples with sorbed Eu(III) was performed as detailed in Chapter 4.9. The goal of this was to better understand the inner sphere coordination of the Eu(III) ion. While the DGA ligand is a neutral extractant and thus will only complex neutral species, it was important to determine whether the ligands would displace the charge-balancing counter-ions to the outer sphere of the metal.

First, emission spectra of the Eu-DGA-SBA samples were recorded. As discussed in Section 4.9, the $^{5}D_0 \rightarrow {}^{7}F_2$ transition is hypersensitive to ligand complexation while the $^{5}D_0 \rightarrow {}^{7}F_1$ one is not. Thus, spectra were normalized to the $^{5}D_0 \rightarrow {}^{7}F_1$ peak (Figure 7.16). This also helps account for the fact that each sample presents a slightly different surface to the beam because of the how the particles aggregated. Interestingly, the trend goes as decreasing intensity in the $^{5}D_0 \rightarrow {}^{7}F_2$ peak (612 nm) as a function of increasing acid concentration. This is actually the opposite behavior of what is expected for an increase in ligand field. [174,175] As a metal is complexed by ligands in the inner sphere, the intensity of the $^{5}D_0 \rightarrow {}^{7}F_2$ transition should decrease. However, this could be a sign of the samples all being in equilibrium with fairly similar amounts of metal sorbed and the differences in intensity being of function of the changing nitrate. The fluorescence lifetime decays for the chloride series and nitrate series are presented in Figures 7.17 and 7.18. All of the lifetime decays fit best to bi-exponential decays with an offset (equation 7.1):

$$y = y_0 + A_1 \exp\left(\frac{-(t - t_0)}{\tau_1}\right) + A_2 \exp\left(\frac{-(t - t_0)}{\tau_2}\right) \tag{7.1}$$

where y_0 and y are the initial intensity and intensity at time t, respectively, τ_1 and τ_2 are the lifetimes for the two components of the double exponential, and A_1 and A_2 are the relative

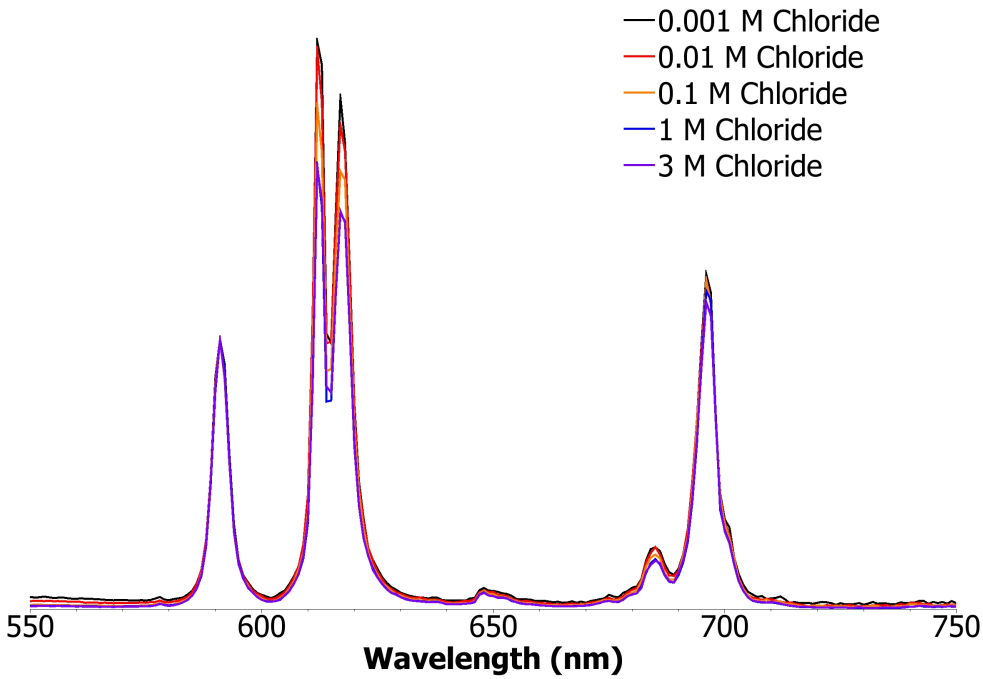

Figure 7.16: Fluorescence emission spectra for Eu-DGA-SBA samples sorbed in pH 3 HCl with varying ionic strengths controlled with NaCl.

contributions of these two decays. This fit was compared to single and bi-exponential decays with no offset, and single exponential with offset. Based on the χ^2 test and residual analysis, the bi-exponential with offset was determined to describe the data the best. Before going into what those fit results indicated, the choice of using an offset or not is worth discussing. The raw fluorescence lifetime data has a gap between the time in which it starts recording and the time the fluorescence hits the detector. Then there is a sharp edge and the signal decays down from there. When fitting the decay, bounds are set and while the left bound can be set after the initial gap, the time delay associated with the onset of fluorescence can still affect the final fit results. Thus, so as not to incorporate that time in the lifetime calculation, the offset is set to the time length associated with the detection gap. The choice of where to set that left bound is also important. In addition to fluorescence of the metal, other species that could have short decay times and confound the results are the ligands. Thus a fluorescence lifetime measurement of the DGA-SBA material with no metal was recorded and the fluorescence lifetime (290 μs) considered when selection the left bound to avoid influence from that decay (Figure 7.19). If the left bound is set too far to the left, effects of the ligand and other species with very short decays can affect the fit, however, if the left bound is set too far to the right, shorter-lived Eu(III) species can also be missed.

The two species determined from the fit results for each of the curves were a shorter lived complex and a longer lived complex. The results are presented in Table 7.3. $EuCl_3$ and $Eu(NO_3)_3$ salts were also measured and their lifetimes were each fit to mono-exponential decays, included in Table 7.3. The more ligands are complexed on the inner sphere of the Eu, the longer the lifetimes become as a result of fewer de-excitation pathways. [116] The shorter lived species may actually be a result of the bare DGA-SBA lifetime or uncomplexed Eu on the surface, which were found to be of

the same order of magnitude (121-290 μs). The longer lived species, however, does indicate that the inner sphere of the metal is fully complexed by the ligands which supports a 3:1 DGA:Eu complex. Long lifetimes that correspond to no waters in the inner sphere agree with what has been observed in the literature for Eu-DGA complexes, despite variations in the lifetimes themselves. [176, 177] The variations in lifetimes may be due to the use of DGA molecules with different R groups, the solvent environments, or the fact that the measurements presented here were done on solid samples while the literature values are from aqueous or organic solutions.

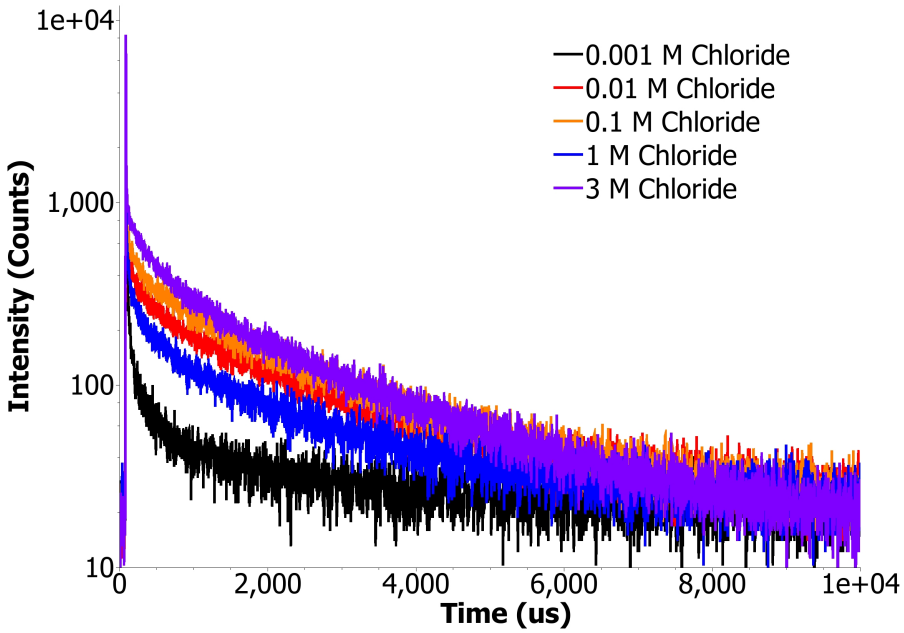

Figure 7.17: Fluorescence lifetime decays for Eu-DGA-SBA samples sorbed in pH 3 HCl with varying ionic strengths controlled with NaCl.

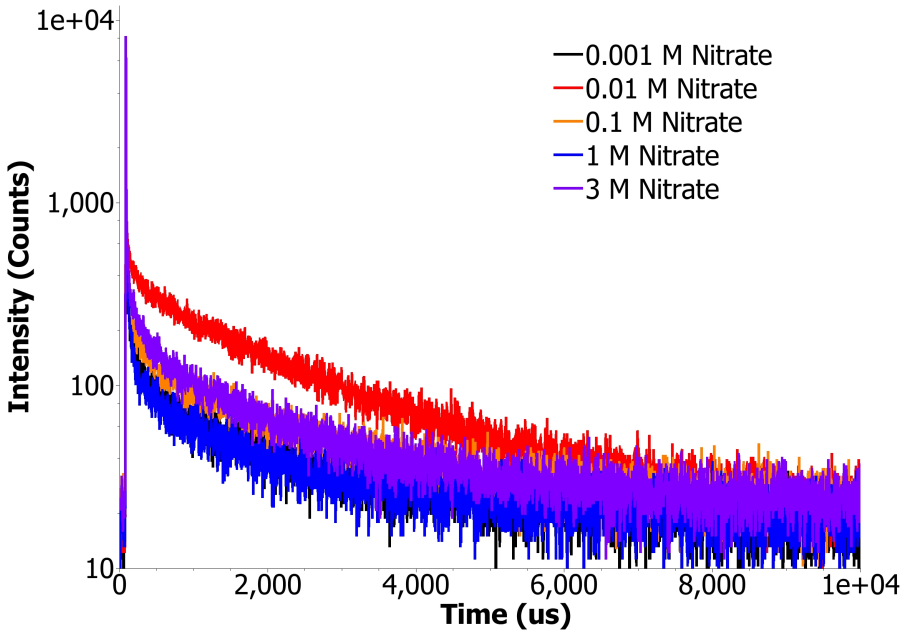

Figure 7.18: Fluorescence lifetime decays for Eu-DGA-SBA samples sorbed in pH 3 HNO_3 with varying ionic strengths controlled with $NaNO_3$.

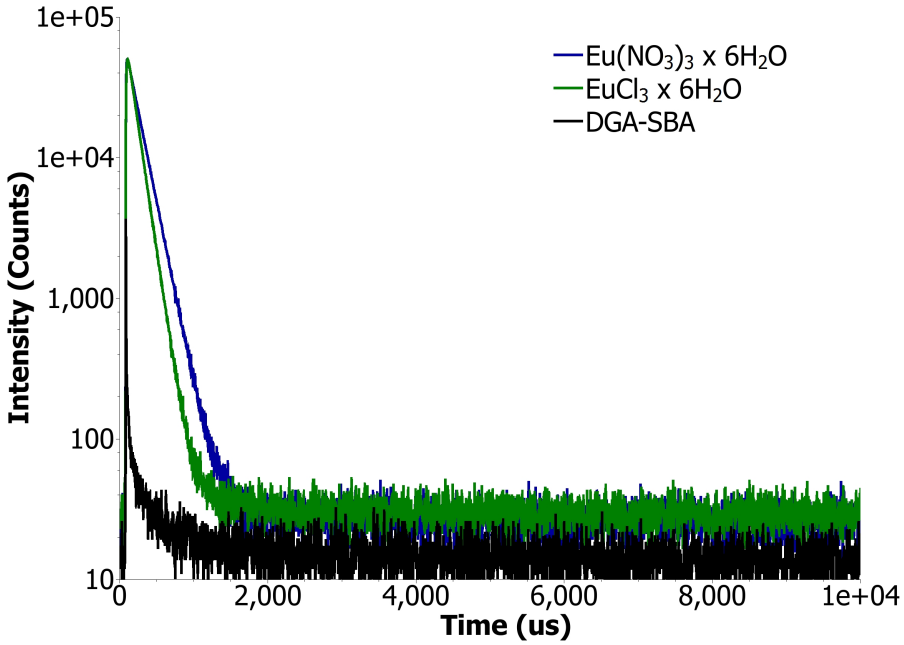

Figure 7.19: Fluorescence lifetime decays for $EuCl_3xH_2O$, $Eu(NO_3)_3xH_2O$, and DGA-SBA samples

Table 7.3: Results of fluorescence lifetime analysis for Eu-DGA-SBA samples

Matrix	y_0 (counts)	A_1 (a.u)	τ_1 (ms)	$N_{H_2O,1}$	A_2 (a.u)	τ_2 (ms)	$N_{H_2O,2}$
0.001 M HCl	22.0 ± 0.5	122.7 ± 5.8	0.172 ± 0.011	5.68 ± 0.05	35.0 ± 1.6	1.820 ± 0.137	0.14 ± 0.40
0.01 M HCl	25.6 ± 1.0	187.3 ± 5.4	0.258 ± 0.014	3.63 ± 0.21	233.8 ± 3.3	2.080 ± 0.048	0.07 ± 0.43
0.1 M HCl	26.8 ± 1.0	231.0 ± 6.8	0.242 ± 0.013	3.90 ± 0.21	324.7 ± 3.9	1.986 ± 0.037	0.09 ± 0.43
1 M HCl	24.8 ± 0.7	184.1 ± 5.2	0.235 ± 0.012	4.03 ± 0.21	146.9 ± 3.0	1.877 ± 0.056	0.12 ± 0.42
3 M HCl	21.5 ± 1.2	446.8 ± 6.2	0.292 ± 0.008	3.15 ± 0.34	387.6 ± 5.2	1.975 ± 0.037	0.09 ± 0.43
0.001 M HNO_3	19.2 ± 0.5	118.6 ± 6.2	0.172 ± 0.012	5.68 ± 0.01	73.6 ± 1.7	1.828 ± 0.070	0.13 ± 0.42
0.01 M HNO_3	23.6 ± 1.0	139.5 ± 6.4	0.244 ± 0.020	3.87 ± 0.08	307.4 ± 3.5	2.038 ± 0.039	0.08 ± 0.43
0.1 M HNO_3	25.7 ± 0.5	130.3 ± 7.3	0.169 ± 0.012	5.79 ± 0.02	111.0 ± 2.0	1.750 ± 0.050	0.16 ± 0.42
1 M HNO_3	21.5 ± 0.3	109.6 ± 9.6	0.133 ± 0.013	7.45 ± 0.33	72.1 ± 2.0	1.365 ± 0.049	0.33 ± 0.41
3 M HNO_3	25.8 ± 0.5	201.5 ± 7.4	0.176 ± 0.009	5.51 ± 0.13	133.1 ± 2.6	1.614 ± 0.043	0.21 ± 0.42
$Eu(NO_3)_3 \times 6H_2O$	26.6 ± 0.9	49237 ± 23.1	0.167 ± 0.001	5.86 ± 0.44			
$EuCl_3 \times 6H_2O$	31.3 ± 0.6	55525 ± 27.3	0.121 ± 0.001	8.27 ± 0.44			
DGA−SBA	15.0 ± 0.1	58.6 ± 2.1	0.290 ± 0.012				

7.4.4 X-ray Absorption Spectroscopy

Micro-XAS Mapping

μ-XRF mapping was done on DGA-SBA with sorbed La, Eu, or Lu at 3 M or 0.01 M total chloride concentration. For each Ln-DGA-SBA sample, both the Ln of interest and the Cl were mapped such that their correlation could be examined. The results for each of the samples is presented in Figures 7.20-7.24.

The clusters in each of the samples that contain high concentrations of lanthanide are areas on the sample where the particles are clustered. The very high concentration spots of chloride are most likely NaCl crystals as they do not have associated lanthanide. Based on these maps, it does not appear that the chloride ions are highly correlated to the lanthanide, but rather that there is a slightly higher concentration compared to the average sample in the areas with lanthanides. This could be indicative of an outer-sphere interaction. An inner-sphere interaction would likely result in a much brighter chloride signal in the areas with high lanthanide concentration. It should be noted that due to its lower energy, the range of the chlorine fluorescence is lower than that of the lanthanides in silicon. Thus, while fluorescence from the lanthanides could be from a number of particles below the surface, the chloride signal is from the surface or just below the first layer of particles.

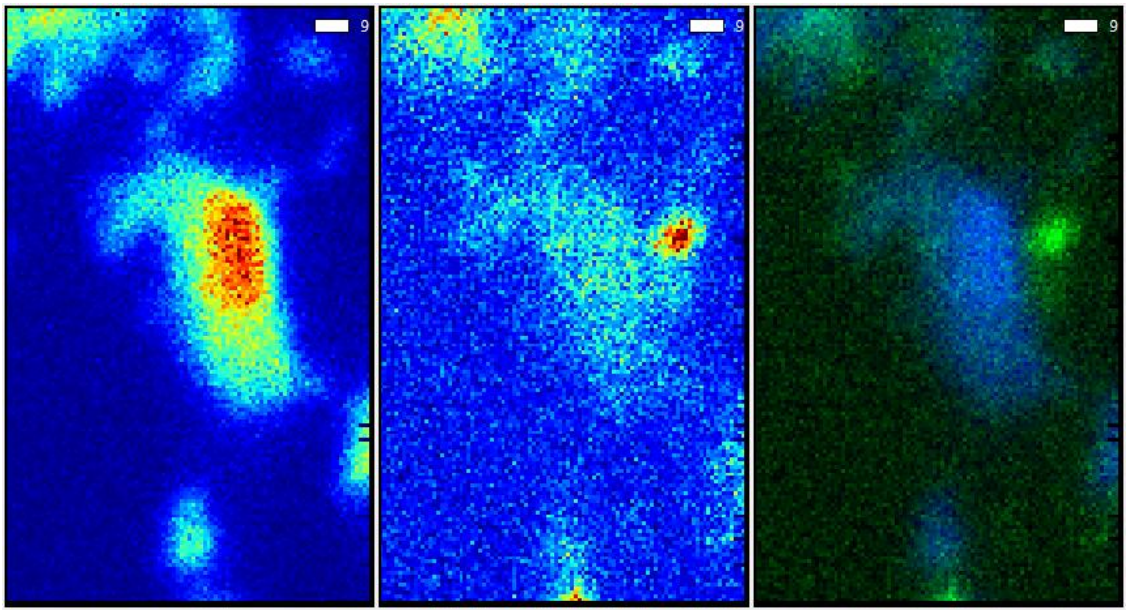

(a) La map (b) Cl map (c) La and Cl

Figure 7.20: X-Ray fluorescence maps for the La-DGA-SBA sample prepared in pH 2 HCl with 3 M total Cl^-. On the single element intensity maps for a) La and b) Cl, blue is low La or Cl concentration and red is high La or Cl concentration. The c) La and Cl bi-color plot uses blue for La and green for Cl where brighter colors are higher concentrations. Scale bars mark 9 μm in length.

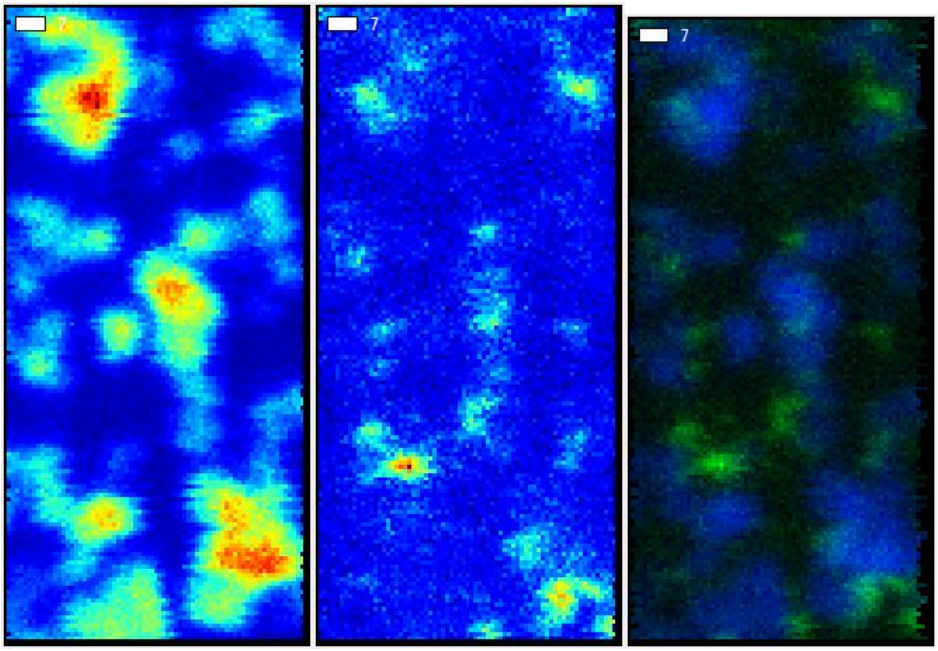

(a) Eu map (b) Cl map (c) Eu and Cl

Figure 7.21: X-Ray fluorescence maps for the Eu-DGA-SBA sample prepared in pH 2 HCl with 3 M total Cl^-. On the single element intensity maps for a) Eu and b) Cl, blue is low Eu or Cl concentration and red is high Eu or Cl concentration. The c) Eu and Cl bi-color plot uses blue for Eu and green for Cl where brighter colors are higher concentrations. Scale bars mark 7 μm in length.

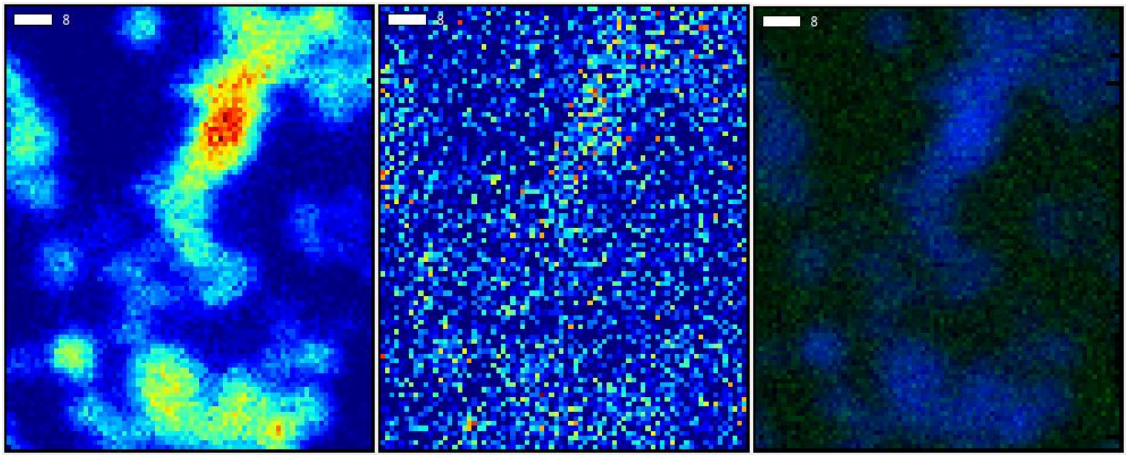

(a) Eu map (b) Cl map (c) Eu and Cl

Figure 7.22: X-Ray fluorescence maps for the Eu-DGA-SBA sample prepared in pH 2 HCl with no added salt. On the single element intensity maps for a) Eu and b) Cl, blue is low Eu or Cl concentration and red is high Eu or Cl concentration. The c) Eu and Cl bi-color plot uses blue for Eu and green for Cl where brighter colors are higher concentrations. Scale bars mark 8 μm in length.

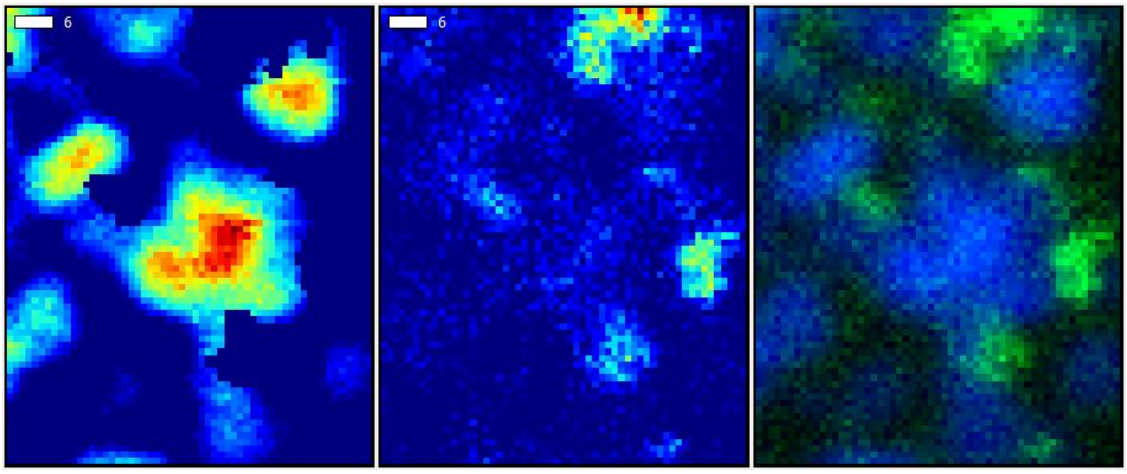

(a) Lu map (b) Cl map (c) Lu and Cl

Figure 7.23: X-Ray fluorescence maps for the Lu-DGA-SBA sample prepared in pH 2 HCl with 3 M total Cl^-. On the single element intensity maps for a) Lu and b) Cl, blue is low Lu or Cl concentration and red is high Lu or Cl concentration. The c) Lu and Cl bi-color plot uses blue for Lu and green for Cl where brighter colors are higher concentrations. Scale bars mark 6 μm in length.

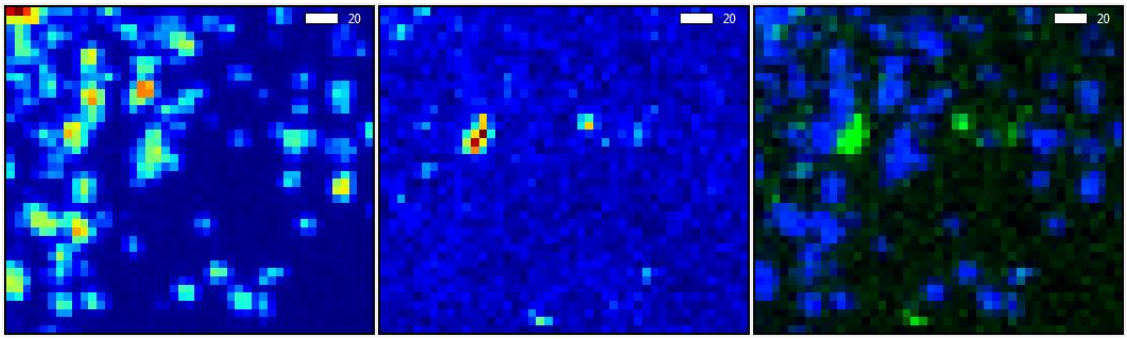

(a) Lu map (b) Cl map (c) Lu and Cl

Figure 7.24: X-Ray fluorescence maps for the Lu-DGA-SBA sample prepared in pH 2 HCl with no added salt. On the single element intensity maps for a) Lu and b) Cl, blue is low Lu or Cl concentration and red is high Lu or Cl concentration. The c) Lu and Cl bi-color plot uses blue for Lu and green for Cl where brighter colors are higher concentrations. Scale bars mark 6 μm in length.

EXAFS

The EXAFS region of the X-ray absorption spectra provide information about the nearest neighbors and the distances between them and the metal. This is particularly useful for determining the inner sphere composition for a particular complex. In the metal-DGA-SBA system, it is clear from the batch sorption results that ionic strength plays an important role in sorption. Ionic strength can affect sorption, however, for a number of reasons including inner-sphere complexation or formation of complexes between the metal and the counter-ion. If the increased ionic strength impacts the EXAFS spectrum, it can be deduced that the counter-ions are playing a role in the inner sphere of the metal. Thus, a variety of Ln(III) and Am(III) samples were prepared on DGA-SBA in different sorption matrices.

Am(III) samples prepared in either pH 2 HCl or pH 2 HNO_3 at high or low ionic strength were found to have nearly identical XAS spectra. While full EXAFS fitting has not yet been performed, fitting of the Am-O path indicated that each of these samples had similar numbers of oxygen atoms within error surrounding the Am and they had an average distance of 2.44-2.45 $\AA$ from the Am (Table 7.4). This means that for Am, based on the similarity between spectra at high and low ionic strength and in both nitrate and chloride, the counter-ions do not impact the inner sphere of the Am ions.

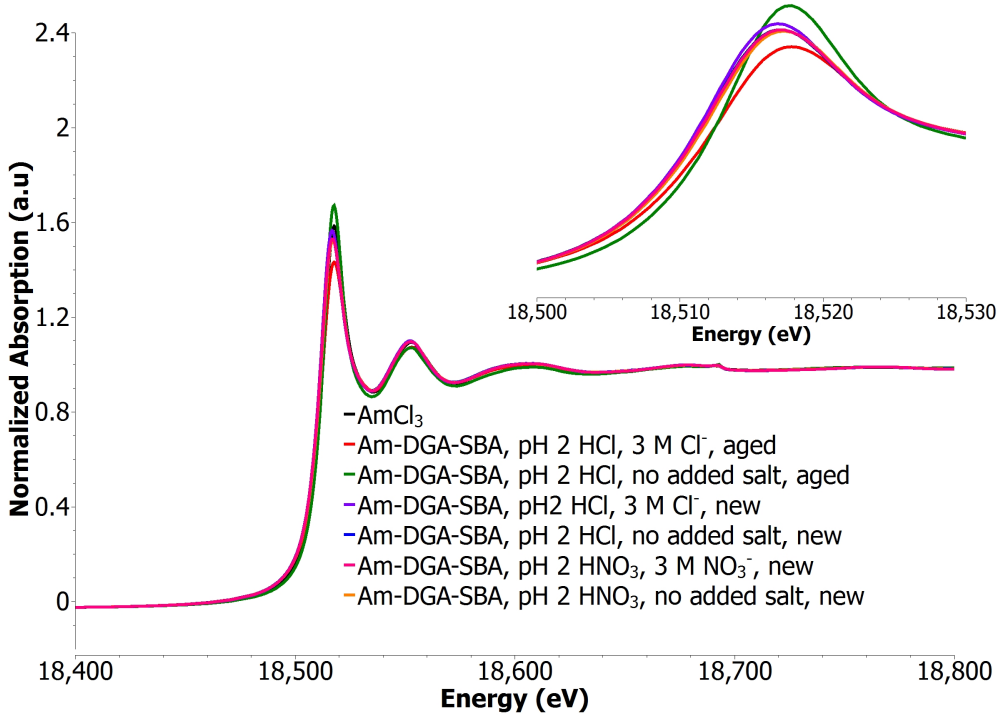

Figure 7.25: Normalized energy XAS spectra for Am samples. Inset is magnified view of white line to better show the slight shift of the aged samples compared to the new samples.

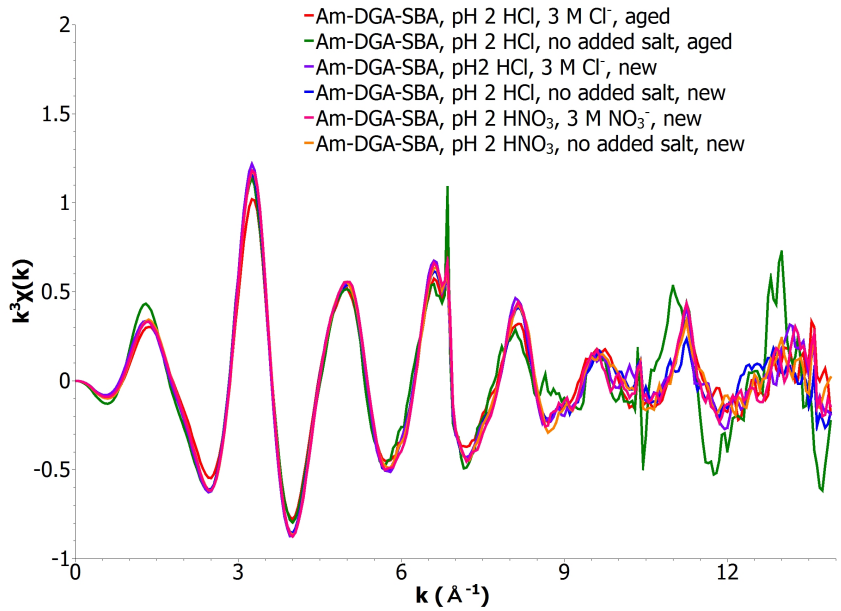

Figure 7.26: $k^2\chi(k)$ Am EXAFS spectra of the Am-DGA-SBA samples in which Am was sorbed at pH 2 either HNO_3 or HCl with either no added salt or balanced to 3 M in NO_3^- or Cl^-, respectively, with the sodium salt. The chloride samples were measured both after being freshly prepared (new) and after sitting in the XAS packaging for 3 months (aged).

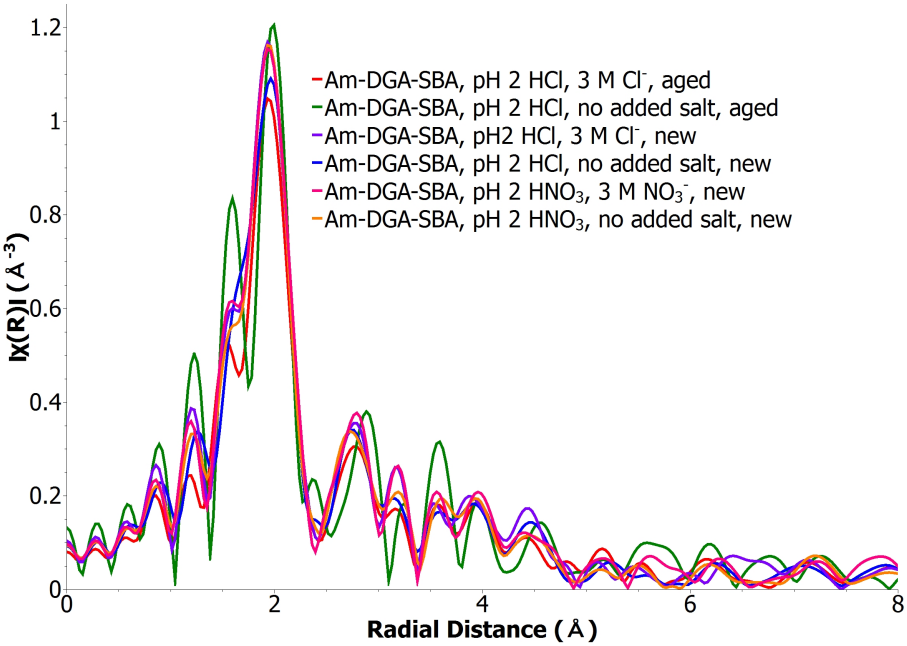

Figure 7.27: R-space plot of XAS spectra for Am-DGA-SBA samples in which Am was sorbed at pH 2 either HNO_3 or HCl with either no added salt or balanced to 3 M in NO_3^- or Cl^-, respectively, with the sodium salt. The chloride samples were measured both after being freshly prepared (new) and after sitting in the XAS packaging for 3 months (aged).

In developing a solid-phase extractant for use with Ln(III) and An(III), it is important to consider the impact of radiolysis on the material. While we could not get access to a gamma irradiation chamber to study the affects of gamma ray dose on the material, we did examine samples that had been in contact with ^{243}Am for an extended period of time. The Am-DGA-SBA samples analyzed by XAS at BL 11-2 at 30 K were prepared in pH 2 HCl with either no added salt or 3 M total Cl^- balanced with NaCl. The high ionic strength samples had approximately 17 μCi of ^{243}Am loaded on 10 mg of DGA-SBA. The low ionic strength samples had approximately 12 μCi of ^{243}Am loaded on 10 mg of DGA-SBA. One set of these samples was measured immediately after preparation. Another identical set of these samples, already dry and packaged for measurement, was allowed to age for just over 3 months (aged samples). As discussed earlier, ^{243}Am emits both alpha particles as well as gamma rays as it decays. After alpha decay, the ^{239}Np daughter is expected to desorb from the DGA-SBA. The DGA-SBA material can experience damage from gamma rays or alpha decays from neighboring Am atoms. In the alpha decay, the alpha particle as well as the recoil nucleus (in this case,^{239}Np) deposit energy in the material. The alpha particle will carry most of the energy of the decay, relative to the recoil nucleus. The recoil nucleus, however, is much more massive. Thus, the recoil can cause damage as a result of its size, but the alpha particles can deposit more energy. [178] As a result of both the alpha particles and the recoil nuclei, alpha decay can be the most destructive form of radiation to a solid because the molecular structure can be broken apart. By comparing the Am-O paths between aged and new samples, it can be determined whether the Am decays have affected nearby Am-DGA-SBA complexes. In looking at the white line in the energy spectra (Figure 7.25) of the new samples compared to the aged samples, there is a shift of 0.5-1 eV to higher energy for the ages samples. The Am-O distance in the aged samples is also slightly higher, however, within error this is not significant. The shift in energy may indicate a slight change in the oxygen coordination environment around the Am and would require further investigation to verify.

Sample	Matrix	Number of Atoms	Distance (Å)	EXAFS Debye-Waller Factor $(Å)^2$	Shift in E_0 (eV)
$AmCl_3$	8 M HCl	8.19 ± 1.37	2.455 ± 0.016	0.0078 ± 0.0025	5.297 ± 1.517
Am-DGA-SBA (aged)	pH 2 3 M Cl^-	6.98 ± 0.85	2.454 ± 0.011	0.0055 ± 0.0015	5.541 ± 1.161
Am-DGA-SBA (aged)	pH 2 HCl	8.28 ± 1.14	2.457 ± 0.012	0.0067 ± 0.0018	5.362 ± 1.228
Am-DGA-SBA (new)	pH 2 HCl 3 M Cl^-	7.84 ± 1.12	2.446 ± 0.013	0.0053 ± 0.0018	4.815 ± 1.371
Am-DGA-SBA (new)	pH 2 HCl	8.12 ± 0.88	2.446 ± 0.010	0.0064 ± 0.0014	4.749 ± 1.011
Am-DGA-SBA (new)	pH 2 HNO_3 3 M NO_3^-	7.77 ± 1.16	2.445 ± 0.015	0.0052 ± 0.0020	5.173 ± 1.650
Am-DGA-SBA (new)	pH 2 HNO_3	7.79 ± 0.64	2.445 ± 0.007	0.0055 ± 0.0010	5.106 ± 0.757

Table 7.4: Summary of EXAFS fitting for americium samples. Only an Am-O single scattering path was considered for these fits. The amplitude reduction factor was set to 0.8. Uncertainties are from the inversion of the covariance matrix as reported by Artemis. Systematic errors have not been included.

The Ln(III) ionic strength samples were measured on SSRL BL 2-3. For each of La, Eu, and Lu, no significant difference between the samples with no added salt and 3 M Cl^- concentration was observed in the XAS spectra (Figure 7.28). This again supports the outer-sphere complexation from the chloride ions. What is evident from these spectra in looking at the data in R-space (Figure 7.29) is the effect of the lanthanide contraction on the oxygen scattering distance. Going across the lanthanide series the ionic radii of the trivalent species decreases, but the Z is increasing. Thus, the overall charge density of the ions increases. Because of this, the complexing oxygen atoms should be pulled closer to the nucleus for lanthanide elements later in the series. This agrees with the XAS data which shows that the Ln-O scattering distance decreases from La to Eu and from Eu to Lu.

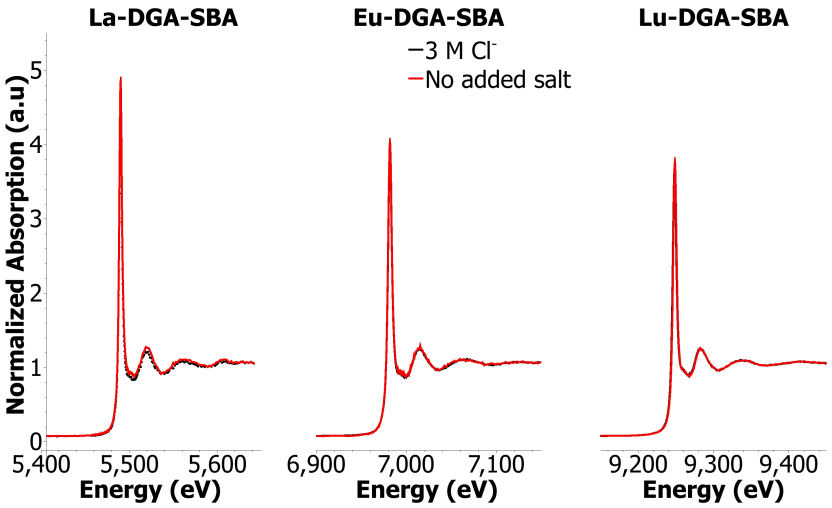

Figure 7.28: Normalized energy XAS spectra for La, Eu, and Lu sorbed to DGA-SBA. Metals were sorbed in pH 2 HCl with either no added salt (red), or 3 M Cl^- balanced with NaCl (black)

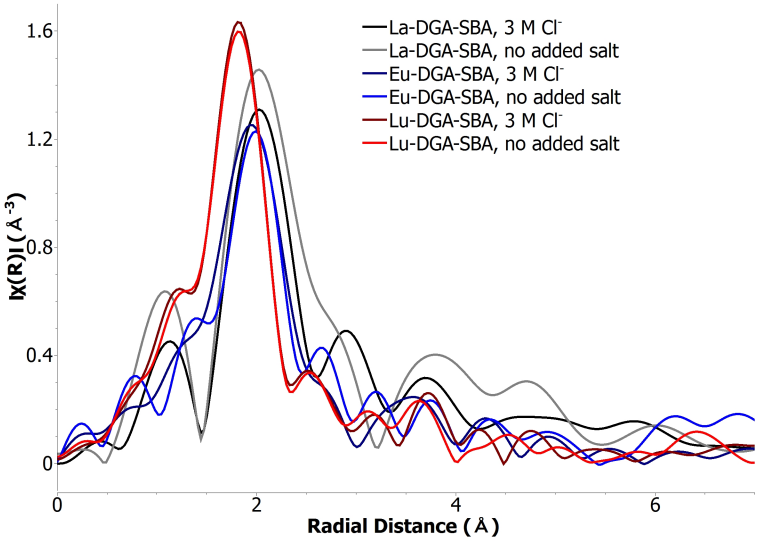

Figure 7.29: R-space plot of XAS spectra for La, Eu, and Lu sorbed to DGA-SBA. Metals were sorbed in pH 2 HCl with either no added salt or 3 M Cl^- balanced with NaCl

As part of the motivation behind the selection of DGA in making the DGA-SBA was the desire to improve DGA solid-phase extractants compared to the Eichrom DGA resin, it was interesting to compare their complexation with Eu in a selection of acids. Eu(III) was sorbed to either DGA-SBA or the Eichrom DGA resin in 1 M HNO_3, $HClO_4$, or HCl after 14-17 hour preconditioning of the materials in the acid of interest. Various acids were tested to verify that a non-complexing acid, $HClO_4$, would behave the same as HCl and HNO_3, further supporting their outer sphere behavior. The Eichrom DGA resin was quite difficult to condition, especially in $HClO_4$ and HCl. These samples, even after pre-conditioning and metal contact followed by 30 minutes of centrifugation, exhibited fractionation of the resin between the bottom and the surface of the solution. Conversely, the DGA-SBA samples were all successfully wetted and could be centrifuged completely to the bottom of the solution. This is likely because the DGA resin is substantially more hydrophobic from the tetraoctyl sidearms on the DGA ligand and the fact that the ligand forms a full coating around the solid support. The DGA-SBA, however, does not form a full monolayer, and silica is hydrophilic. The solution was removed and the dried samples were analyzed at SSRL BL 11-2 at room temperature. The resin that did not wet was difficult to collect and tended to get stuck to the vials and pipette tips when the supernatant was removed. Thus, the bulk of the material analyzed at the beamline from these poorly conditioned samples was the small amount of solid that was successfully wet and centrifuged down.

The results from the XAS study on the Eu sorbed to DGA-SBA compared to Eichrom DGA resin were quite similar (Table 7.5). The normalized energy spectra are presented in Figure 7.30, in which the main difference is the intensity of the white line between samples. The R-space data (Figure 7.31) is again very similar. The first shell fit of the Am-O path points to approximately 9 oxygens around each Eu center. This agrees with the expected three tridentate DGA ligand coordination. The Am-O bond distance is approximately 2.41 $\AA$ for each species which agrees well with the literature bond distance for a Eu-TODGA complex. [179] The similarity between matrices again supports the outer-sphere coordination of the chloride, nitrate and perchlorate ions. Based on the comparison between the commercial DGA resin and the DGA-SBA, the complexation is similar, however the resin wetting for the commercial resin was very difficult especially compared to the DGA-SBA which readily wets in aqueous solution.

Sample	Matrix	Number of Atoms	Distance (Å)	EXAFS Debye-Waller Factor $(Å)^2$	Shift in E_0 (eV)
Eu-DGA-SBA	1 M HNO_3	8.53 ± 0.80	2.416 ± 0.009	0.0077 ± 0.0014	1.829 ± 0.921
Eu-DGA-SBA	1 M HCl	9.64 ± 1.27	2.410 ± 0.013	0.0089 ± 0.0020	1.268 ± 1.203
Eu-DGA	1 M $HClO_4$	9.15 ± 0.96	2.410 ± 0.010	0.0087 ± 0.0016	1.173 ± 1.028
Eu-DGA	1 M HNO_3	9.99 ± 1.12	2.413 ± 0.012	0.0090 ± 0.0017	1.514 ± 1.145
Eu-DGA	1 M HCl	8.68 ± 0.88	2.415 ± 0.010	0.0076 ± 0.0014	1.889 ± 1.001

Table 7.5: Summary of EXAFS fitting for europium samples. Samples were measured on BL 11-2 at SSRL. Samples denoted DGA-SBA were sorbed on the synthesized DGA-SBA material, and those denoted DGA only were sorbed on the Eichrom DGA resin. Only a Eu-O single scattering path was considered for these fits. The amplitude reduction factor was set to 0.8. The uncertainties presented are from the inversion of the covariance matrix as reported by Artemis. Systematic errors have not been included.

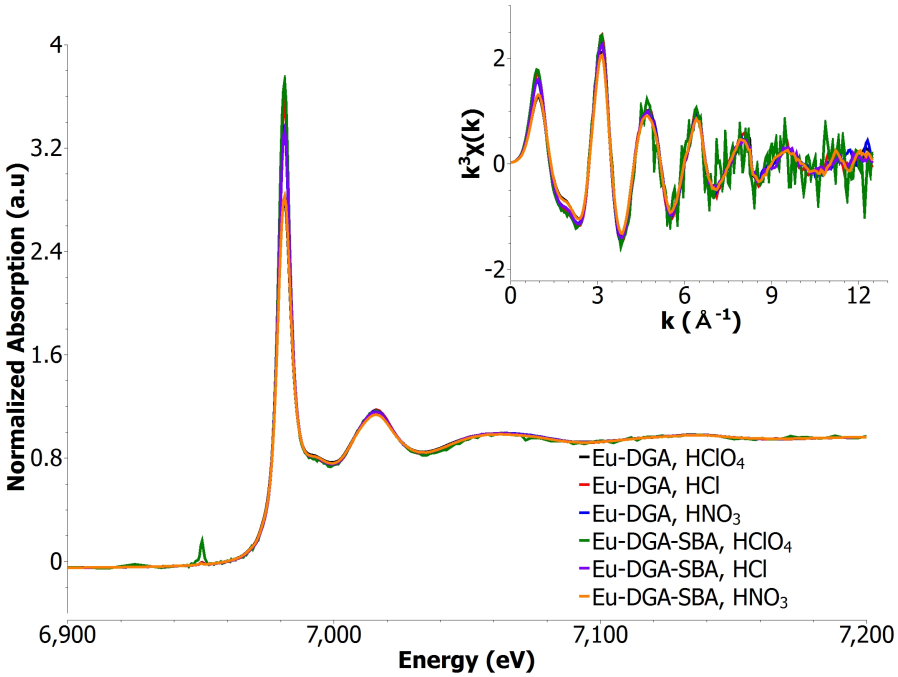

Figure 7.30: Normalized energy XAS spectra for Eu sorbed to diglycolamide solid-phase extractants in various acid matrices. Inset is the $k^2\chi(k)$ Eu EXAFS spectra of the same Eu samples. Eu-DGA denotes Eu sorbed to the Eichrom DGA resin, whereas Eu-DGA-SBA represents Eu sorbed to the DGA-SBA material. All acid concentrations for sorption were 1 M.

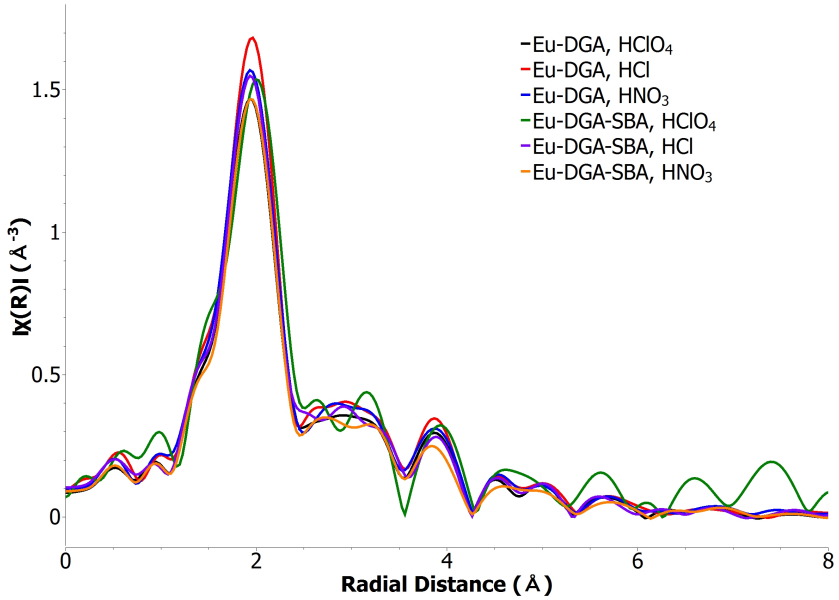

Figure 7.31: R-space plot of XAS spectra for Eu sorbed to diglycolamide solid-phase extractants in various acid matrices. Eu-DGA denotes Eu sorbed to the Eichrom DGA resin, whereas Eu-DGA-SBA represents Eu sorbed to the DGA-SBA material. All acid concentrations for sorption were 1 M.

7.5 Chromatography

To verify that DGA-SBA could be used as a stationary phase for a column, a couple of proof-of-principle experiments were done using Eu(III). A Pt-tipped glass column was packed with a DGA-SBA slurry, capping the resin bed on either end with glass wool. The column volume (CV) was approximately 170 μL, with a resin height of 2 cm. The flow rate was about 12 drops per minute (120 μL min^{-1}).

In the first experiment, the resin was conditioned with 15 CVs of 1 M HNO_3 prior to loading 75 μL of 1.2 mM Eu(III), which was added as $Eu(NO_3)_3$ with a ^{152}Eu tracer in 1 M HNO_3. The column was washed with 5.5 CVs of 1 M HNO_3 then eluted with 17 CVs of pH 5.5 HCl. Throughout the wash stage, no Eu was eluted from the column, which means that the resin is not bleeding and that Eu is strongly retained. During the pH 5.5 HCl elution, very little Eu was eluted from the column. It eluted slowly with less than 1 % of the total Eu in each of the fractions.

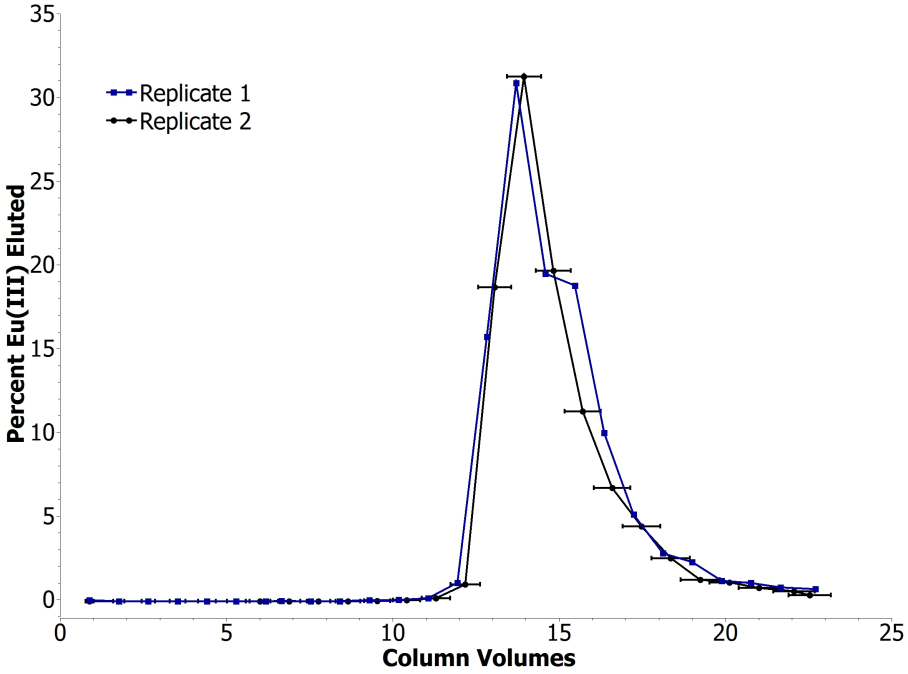

Figure 7.32: Loading and elution curve for Eu(III) on a column containing DGA-SBA as the stationary phase. Conditioning, loading, and washing were all done with 1 M HNO3. Eu(III) was eluted in 1 mM EDTA. Vertical error bars represent counting error and are too small to be visible on the scale of this figure. Connecting lines added to guide the eye.

In the second experiment, the resin was conditioned with 15 CVs of 1 M HNO_3 prior to loading 75 μL of 1.2 mM Eu(III), which was added as $Eu(NO_3)_3$ with a ^{152}Eu tracer in 1 M HNO_3. The column was washed with 5.5 CVs of 1 M HNO_3 then eluted with 17 CVs of 1 mM EDTA. The resulting elution curve is presented in Figure X. As evident in Figure 7.32, there was again no Eu eluted during the 1 M HNO_3 wash phase, but in this column all of the Eu was successfully eluted using 1 mM EDTA. The Eu elution peak does exhibit tailing, and this may be due to the diffusion through the mesoporous, however further studies are required to make any conclusive remarks regarding the tailing. To potentially minimize tailing, the flow rate can be adjusted.

7.6 Discussion

Previous studies have immobilized diglycolamide ligands on silica, [27–29] but this is the first time these ligands have been covalently bound to mesoporous silica, a much higher surface area substrate. The result of using mesoporous silica is that the material has a higher surface area (397 m^2g^{-1}) and in turn a higher metal ion capacity compared to an analogous DGA resin that was not on a mesoporous substrate (substrate surface area: 180 m^2g^{-1}) [27]. The Eu(III) sorption capacity determined for the DGA-SBA presented here was 379 μmol g^{-1} (57 mg g^{-1}) which is four times higher than the higher capacity analogous resin (14 mg g^{-1}) presented by Ansari, et al. [27] In comparing Eu sorption from 3 M HNO_3 for the DGA-SBA to the same analogous resins, the DGA-SBA has a much higher K_d at 2.4 x 10^4 relative to 2.7 x 10^3 and 5.7 x 10^3 for the two resins made by Verboom et al. The same trend is observed for Am; however, these results are not directly comparable as the metal ion concentrations were significantly higher in this work compared to those in the literature. The higher K_d values are likely due to the higher surface area and in turn, higher ligand loading, of the DGA-SBA material.

The ligand loading for the commercially available DGA resin [3] material is lower at approximately 688 μmol g^{-1} ligands nm^{-2}, but it has a higher ligand density of 0.83 silanes per nm^2 (based on 500 m^2g^{-1} surface area [180] of Amberchrom-CG71) which is likely due to a thicker ligand layer in the coated material than is possible with a covalently bound material. Eu sorption capacity for the DGA-SBA is again higher compared to the commercially available resin (379 μmol g^{-1} vs. 203 μmol g^{-1}). The higher capacity for DGA-SBA despite the lower ligand density supports the hypothesis that the coated solid-phase extractants leave many ligands inaccessible to the metal, whereas covalently bound ligands are more accessible. DGA-SBA has the highest Eu(III) capacity of all diglycolamide solid-phase extractants thus reported. [3, 27]

DGA-SBA sorbed Eu and Am effectively in acid concentrations between 0.1 M and 3 M. The nearly complete sorption of both Am(III) and Eu(III) from nitric and hydrochloric acid at these concentrations is promising for sequestration of these metals with DGA-SBA from dissolved used nuclear fuel or legacy waste. Additionally, the stability of the ligand in the presence of acid indicates that the DGA-SBA could be reused, resulting in less waste production per extraction. EDTA was effective in completely desorbing the metals from the DGA-SBA. While it is not ideal to use an organic complexing agent to desorb, especially when trying to eliminate hazardous organic waste production, the overall volume and concentration of EDTA is low relative to a liquid-liquid extraction. The efficacy of EDTA at desorbing Eu(III) was demonstrated in a column experiment in which, Eu(III) was completely eluted from the column using a small volume of EDTA. Future work can explore other inorganic eluents that can desorb Eu(III) and Am(III).

Am was found to have faster sorption kinetics relative to Eu that follow a pseudo-second order rate law. Additionally, over twice the relative amount of Eu sorbed to the DGA-SBA compared to Am in 0.01 M HCl. The difference in sorption behavior for Am and Eu at 0.01 M HCl could potentially be utilized for a separation, especially if coupled with the difference in sorption kinetics; however, this would require detailed further study. If Am and Eu could be separated using DGA-SBA, then it would not only be an efficient bulk sequestration agent for trivalent actinides and lanthanides but could also potentially be used to isolate Am from the lanthanide fission products.

The metal-DGA-SBA complex formation was probed using a variety of spectroscopic techniques which complemented each other well and ultimately point towards the formation of three DGA ligands binding to the inner sphere of the metal. Based upon spectroscopic evidence,

the counter-ions, nitrate or chloride, are not part of the inner sphere of the complex but must still be associated to balance the charge of the ML_3^{3+} complex, where L is the DGA ligand. Thus, it is concluded that the counter-ions are present in the outer sphere for the trivalent lanthanides and actinides. As DGA is a neutral extractant, it required neutral species to complex. In light of this, the mechanism required for metal complexation by DGA-SBA is such that the metal first forms the neutral $M(NO_3)_3$ or MCl_3 complex prior to the DGA ligands displacing the inner sphere of the metal and fully coordinating the Ln(III) or An(III). Based on the high ionic strength batch experiments, it is clear that increased counter-ion concentration leads to increased metal sorption. This is likely due to the abundance of counter-ions available to form the $M(NO_3)_3$ or MCl_3 complex, required by the first step of the mechanism.

7.7 Conclusion and Outlook

As DGA-SBA has proven to be a promising material for sequestration of trivalent actinides and lanthanides, there are a number of future studies that can and should be conducted with this material. The DGA ligand was resistant to acid hydrolysis under the 1 day of 1 M HNO_3 tested, however there was cleavage of isolated ligands on the surface. Further acid degradation studies should include high concentrations of acid, longer contact times, and tests of reusability in addition to the NMR experiments. Total carbon, hydrogen, nitrogen analysis after acid contact could also be an informative means of quantifying the degradation of the DGA-SBA material. While the effect of radiation was touched on with the aged Am-DGA-SBA XAS studies, there is still much more to look at here. Continued analysis of those aged Am-DGA-SBA samples over the course of a long time (months or even years) would be an interesting long-term material stability study. Additionally, the affects of gamma dose using a ^{60}Co or ^{137}Cs gamma irradiator on the DGA-SBA would provide insight into the effects of the dose given off by high activity starting materials to which the resin may be exposed. Last, an alpha bombardment study done in aqueous solution would provide a better model of the actual system. This could be done by doping the solution with a non-chemically reactive species that could undergo an (n,α) reaction when in a neutron source such as a reactor.

DGA-SBA was found to be a highly efficient sorbent material for trivalent actinides and lanthanides from nitric and hydrochloric acid matrices. The DGA-SBA was an effective solid-phase extractant both in batch contact studies and in column experiments confirming the potential for its use as a chromatographic stationary phase. Future work in with the DGA-SBA and the trivalent lanthanides and actinides mainly involves chromatography experiments testing the separation of these species from one another. This will include tuning the flow rate, eluent matrix, column length, among a number of other parameters. The competitive desorption of Am and Eu in EDTA will be an especially interesting set of experiments to conduct. Further examination of the kinetic differences between Eu(III) and Am(III) will be an interesting avenue of study especially focusing on competition reactions and kinetic based separations. Dynamic studies varying the competing ion concentrations can inform the strength of the complexes and their rate of formation.

The behavior of a greater number of lanthanides will have to be thoroughly characterized as well as that of Cm(III), and potentially even Pu(III), Bk(III), and Cf(III). Beyond the trivalent species, the interactions of actinide elements in other oxidation states such as Np(V), Pu(IV), Pu(VI), U(VI), etc, with DGA-SBA are needed to thoroughly characterize DGA-SBA as a solid-phase extractant.

Chapter 8

Conclusions and Future Work

8.1 Conclusions

While the commercially available DGA resin (Chapter 5), did not provide particularly promising results, it helped motivate the work presented in Chapters 6 and 7. Based on the suspected degradation of the commercial DGA resin, the need for solid-phase extractants that are more stable in the presence of acid became clear. While previous work on organically-modified mesoporous silica materials in the Nitsche group was pioneered by Tashi Parsons-Moss, [181] the current work has a different focus. The work presented in Chapters 6 and 7 was aimed at the interactions of new materials with trivalent actinides and lanthanides, and the effects of acid on these materials.

Acid hydrolysis studies for both the CA and DGA-SBA materials indicated that isolated ligands on the surface were more prone to cleavage at the silane anchor than polymerized ligands after acid contact. The 7-membered ring of the CA ligand opened after acid contact, but the resulting ligand conformation was likely better able to bind with metals than the unopened ring species. The DGA ligand was found to be resistant to acid hydrolysis after 1 day of contact with 1 M HNO_3. X-ray absorption spectroscopy of aged and new Am-DGA-SBA support the hypothesis that alpha particles from the ^{243}Am alpha decay may strike nearby ligands and cause them to break apart. The Am-O path in the XAS spectra for the aged and new Am-DGA-SBA samples point to both an edge shift of approximately 0.5 eV and different numbers of nearby oxygen atoms based on the sample age. While a structure of the resulting ligand after alpha irradiation cannot be deduced from the data fitting presented here and without additional information, it can be concluded that the aging does affect the number of oxygen atoms in the inner coordination sphere of the Am.

The CA-SBA material was found to be ineffective at sorbing Eu(III), although, it bound both Al(III) and Sc(III). Al and Sc were each found to complex through both the ligand and the silanols on the silica surface. This cooperative mechanism emphasizes the importance of conducting molecular level studies when designing new solid-phase extractants. Multiple complexation pathways can result in more than one stability constant for a single material with a single metal under identical conditions. Multiple stability constants can affect separations as the metal will have different pathways of interaction with the stationary phase and thus can elute at various points in a separation.

The DGA-SBA material was effective at binding both Eu(III) and Am(III) from highly acidic matrices. Increasing ionic strength of the solution also enhanced the metal uptake on the DGA-SBA. While other DGA based solid-phase extractants have been reported in the literature the

DGA-SBA presented in Chapter 7 has the highest reported capacity thus far. The implication of this is the smaller amount of solid required to either run a chromatographic column or to bulk sequester the same quantity of Eu(III). The various spectroscopic techniques used to probe the M(III)-DGA-SBA species agreed well with one another. From IR spectroscopy and $^{13}C\{^{1}H\}$ CP/MAS NMR spectroscopy, Eu complexation to the the ligand through the carbonyl and ether oxygens of the DGA binding site was confirmed. Fluorescence spectroscopy and XAS both support three DGA ligands coordinating to each trivalent metal center. Examination of the impact of ionic strength and the inner sphere composition for the various metals supports outer sphere coordination of the nitrate and chloride ions with the DGA ligands occupying the full inner sphere of metal. Thus, the importance of high nitrate or chloride concentration for high metal uptake can be attributed to the necessity of forming a neutral $M(NO_3)_3$ or MCl_3 complex as DGA is a neutral extractant.

The potential for using OMMS materials as chromatographic resins not only depends upon the metal interactions with the extractant ligands, but also the particle shape and size, and pore shape and size. As discussed in Chapter 3, spherical particles are necessary for reproducible chromatogrpahy, and the mesoporous silica could be produced with this particle shape. A concern with mesoporous silica is whether the metal containing solution and eluent can diffuse through the pores effectively and also the rate associated with this diffusion relative to flow around the particles. Based on the proof-of-concept column experiments presented in Chapter 7, the ability of solution to flow through a column with DGA-SBA as a stationary phase was confirmed. The tailing present in the Eu elution peak may be because of different diffusion rates through the mesopores compared to around the particles, but this needs to be investigated further.

Overall, the work presented in this dissertation emphasizes the importance of using complementary macroscopic and molecular level studies to understand materials that can be used as sequestration and separation agents. The DGA-SBA material proved to be particularly promising and future work optimizing it for chromatographic applications should be conducted. While liquid-liquid separations are the standard for large-scale lanthanide and actinide separations, the implementation of solid-liquid separations should also be considered.

8.2 Future Work

As discussed in Chapter 7, there is a great deal of future work needed with the DGA-SBA material. Beyond the materials discussed in this work, there are an infinite number of organically-modified mesoporous silica materials that can be synthesized. One material of interest, but that is not synthetically feasible via current grafting methods, is a dithiophosphinic acid modified mesoporous silica. Dithiophosphic acids have been used for Am(III)/Cm(III) separations. [6, 182] However, the binding site of this class of ligands is highly reactive and a methoxysilane group could not be added without compromising the binding site. To make a dithiophosphinic acid modified mesoporous silica, a potential synthetic pathway may involve building the ligand up from the surface as opposed to attachment of the whole ligand in a single step. Additionally, it may be possible to covalently bind this ligand to a polymer surface instead. Another group of ligands that have been of interest in the nuclear fuel cycle are the BTBP ligands mentioned in Chapter 1. BTBP ligands are bulky and thus may inhibit diffusion through the mesopores; however, only one or two are required to bind trivalent lanthanides and actinides.

While mesoporous silica offers a number of advantages over other substrates, mesoporous carbon and polymers can also compensate for some of the weaknesses in the silica. Mesoporous carbon is particularly interesting because of its potential use an electrode material. The dissertation

work of Tashi Parsons-Moss focuses on the mesoporous carbon materials in their unoxidized and oxidized forms. [181, 183] Building on that work and the work presented here could allow for development of organically-modified mesoporous carbons such as a DGA modified carbon. [184] Organic polymers may offer a substrate that can form more stable anchors for monomers on the surface if C-C bonds are used. Another study on stability that will inform synthetic methods is testing the effect of ligand polymerization on degradation in the presence of acid. The results from Chapters 6 and 7 both support polymerized ligands being more resistant to acid catalyzed hydrolysis than isolated ligands on the silica surface. Thus a rigorous study varying degree of polymerization and subsequent degradation will be a strong avenue for future work.

Future work with OMMS materials should involve testing interfering ions expected in samples of interest. Potential species that may be present in PUREX raffinate include Ca, Cs, and Ba all of which may bind to the solid-phase extractant. A simulant of PUREX raffinate should also be studied to test the efficacy of the OMMS materials in a more realistic matrix than the lab solutions examined thus far.

Beyond testing new ligands and additional metals, optimizing the implementation of the OMMS materials is necessary for eventual application. While preliminary chromatographic studies are discussed in this dissertation, there is still optimization regarding the chromographic parameters required. The OMMS materials should be packed into a liquid chromatography column and tested with pump pressure for the potential end use in a high pressure system for rapid separations. Automated systems will allow higher activity samples to be analyzed such as irradiated target materials. Other possible geometries of the OMMS besides a column may provide ideal surfaces for processing large volumes of solution. Possible configurations include flat sheets and coated dipsticks that could be dragged through large volumes of solution. In addition to testing these different physical forms of the OMMS materials, computational diffusion modeling will help inform design. The computational modeling will also help with optimizing particle size and shape, pore size and shape, and solution flow rate.

While there has been a substantial amount of work already done examining organically-modified mesoporous materials, there is still room for major advancements. Future work on these materials could transition them from lab use only to industrial application for lanthanide and actinide sequestration and separation.

Bibliography

[1] Peter Klobes, Klaus Meyer, and Ronald G Munro. Porosity and Specific Surface Area Measurements for Solid Materials. *NIST Recommended Practice Guide*, 960(17), 2006.

[2] K. S. W. Sing, D. H. Everett, R. a. W. Haul, L. Moscou, R. a. Pierotti, J. Rouquérol, and T. Siemieniewska. Reporting Physisorption Data for Gas/Solid Systems with Special Reference to the Determination of Surface Area and Porosity. *Pure & Appl. Chem.*, 57(4):603–619, 1985.

[3] E. P. Horwitz, D. R. McAlister, A. H. Bond, and R. E. Barrans Jr. Novel Extraction of Chromatographic Resins Based on Tetraalkyldiglycolamides: Characterization and Potential Applications. *Solvent Extraction and Ion Exchange*, 23(3):319–344, May 2005.

[4] Nuclear Energy Agency. Physics and Safety of Transmutation Systems. Technical Report 6090, Organisation for Economic Co-operation and Development, 2006.

[5] Henk H. Dam, David N. Reinhoudt, and Willem Verboom. Multicoordinate ligands for actinide/lanthanide separations. *Chemical Society reviews*, 36(2):367–77, March 2007.

[6] Frank Lewis, Michael Hudson, and Laurence Harwood. Development of Highly Selective Ligands for Separations of Actinides from Lanthanides in the Nuclear Fuel Cycle. *Synlett*, 2011(18):2609–2632, October 2011.

[7] Mikael Nilsson and Kenneth L. Nash. Review Article: A Review of the Development and Operational Characteristics of the TALSPEAK Process. *Solvent Extraction and Ion Exchange*, 25(6):665–701, 2007.

[8] Kenneth L. Nash. The Chemistry of TALSPEAK: A Review of the Science. *Solvent Extr. Ion Exch.*, 33(1):1–55, 2015.

[9] P. Baron, X. Heres, M. Lecomte, and M. Masson. Separation of the Minor Actinides : the DIAMEX-SANEX Concept. In *Proceedings of GLOBAL 2001*, 2001.

[10] Andreas Wilden, Christian Schreinemachers, Michal Sypula, and Giuseppe Modolo. Direct Selective Extraction of Actinides (III) from PUREX Raffinate using a Mixture of CyMe 4 BTBP and TODGA as 1- cycle SANEX Solvent. *Solvent Extraction and Ion Exchange*, 29(May 2012):190–212, 2011.

[11] Christine Rostaing, Christophe Poinssot, Dominique Warin, Pascal Baron, and Brigitte Lorraina. Development and Validation of the EXAm Separation Process for Single Am Recycling. *Procedia Chemistry*, 7:367–373, 2012.

[12] Emma Aneheim, Christian Ekberg, Anna Fermvik, Mark R. St. J. Foreman, Teodora Retegan, and Gunnar Skarnemark. A TBP/BTBP-based GANEX Separation Process. Part 1: Feasibility. *Solvent Extraction and Ion Exchange*, 28(4):437–458, 2010.

[13] Emma Aneheim, Christian Ekberg, Anna Fermvik, Mark R. St J. Foreman, Bohumír Grner, Zuzana Hájková, and Magda Kvičalová. A TBP/BTBP-based GANEX Separation Process-Part 2: Ageing, Hydrolytic, and Radiolytic Stability. *Solvent Extraction and Ion Exchange*, 29(2):157–175, 2011.

[14] Gregory R. Choppin and Robert J. Silva. Separation of the Lanthanides by Ion Exchange with Alpha-hydroxy Isobutyric Acid. *Journal of Inorganic and Nuclear Chemistry*, 3(2):153–154, 1956.

[15] Helen L. Smith and Darleane C. Hoffman. Ion-exchange separations of the lanthanides and actinides by elution with ammonium alpha-hydroxy-isobutyrate. *Journal of Inorganic and Nuclear Chemistry*, 3(3-4):243–247, October 1956.

[16] Yuezhou Wei, Mikio Kumagai, Yoichi Takashima, Giuseppe Modolo, and Reinhard Odoj. Studies on the Separation of Minor Actinides from High-Level Wastes by Extraction Chromatography using Novel Silica-Based Extraction Resins. *Nuclear Technology*, 132:413–423, 2000.

[17] Stéphane Bourg, Jean-Charles Broudic, Olivier Conocar, Joël J. E. Moreau, Daniel Meyer, and Michel Wong Chi Man. Tailoring of Organically Modified Silicas for the SolidLiquid Extraction of Actinides. *Chemistry of Materials*, 13(2):491–499, February 2001.

[18] H. Hoshi, Y.-Z. Wei, M. Kumagai, T. Asakura, and Y. Morita. Separation of trivalent actinides from lanthanides by using R-BTP resins and stability of R-BTP resin. *Journal of Alloys and Compounds*, 408-412:1274–1277, February 2006.

[19] Yoshito Usuda, Shigekazu, Liu, Ruiqin, Wei, Yuezhou, Xu, Yuanlai, Yamazaki, Hiromichi, and Wakui. Evaluation Study on Properties of a BTP Extraction Resin Novel RBTP Extraction Resin-From a Viewpoint of Simple Separation of Minor Actinides. *Journal of Ion Exchange*, 21(1):35–40, 2010.

[20] Ruiqin Liu, Yuezhou Wei, Yuanlai Xu, Shigekazu Usuda, Seongyun Kim, Hiromichi Yamazaki, and Keizo Ishii. Evaluation study on properties of isohexyl-BTP/SiO2-P resin for direct separation of trivalent minor actinides from HLLW. *Journal of Radioanalytical and Nuclear Chemistry*, 292(2):537–544, January 2012.

[21] Ruiqin Liu, Xinpeng Wang, Yuezhou Wei, Weiqun Shi, and Zhifang Chai. Evaluation study on a macroporous silica-based isohexyl-BTP adsorbent for minor actinides separation from nitric acid medium. *Radiochimica Acta*, 102(1-2):93–100, January 2014.

[22] S. A. Ansari, P. K. Mohapatra, D. R. Prabhu, and V. K. Manchanda. Transport of Americium(III) through a supported liquid membrane containing N,N,N,N-tetraoctyl-3-oxapentane diamide (TODGA) in n-dodecane as the carrier. *Journal of Membrane Science*, 282(1-2):133–141, October 2006.

[23] M. Husain, S. A. Ansari, P. K. Mohapatra, R. K. Gupta, V. S. Parmar, and V. K. Manchanda. Extraction chromatography of lanthanides using N,N,N,N-tetraoctyl diglycolamide (TODGA) as the stationary phase. *Desalination*, 229(1-3):294–301, September 2008.

[24] G. Modolo, H. Asp, C. Schreinemachers, and H. Vijgen. Recovery of actinides and lanthanides from high-level liquid waste by extraction chromatography using TODGA+TBP impregnated resins. *Radiochimica Acta*, 95(7):391–397, July 2007.

[25] Anyun Zhang, Yuezhou Wei, and Mikio Kumagai. Separation of Minor Actinides and Rare Earths from a Simulated High Activity Liquid Waste by Two Macroporous Silicabased Polymeric Composites. *Separation Science and Technology*, 42(10):2235–2253, July 2007.

[26] K. Van Hecke and G. Modolo. Separation of actinides from Low Level Liquid Wastes (LLLW) by extraction chromatography using novel DMDOHEMA and TODGA impregnated resins. *Journal of Radioanalytical and Nuclear Chemistry*, 261(2):269–275, 2004.

[27] Seraj A Ansari, Prasanta K Mohapatra, Mudassir Iqbal, Jurriaan Huskens, and Willem Verboom. Two novel extraction chromatography resins containing multiple diglycolamide-functionalized ligands: Preparation, characterization and actinide uptake properties. *Journal of chromatography. A*, 1334:79–86, March 2014.

[28] Prasanta K. Mohapatra, Seraj A. Ansari, Mudassir Iqbal, Jurriaan Huskens, and Willem Verboom. First example of diglycolamide-grafted resins: synthesis, characterization, and actinide uptake studies. *RSC Advances*, 4(20):10412–10419, 2014.

[29] Seraj A. Ansari, Prasanta K. Mohapatra, Mudassir Iqbal, Jurriaan Huskens, and Willem Verboom. Sorption of americium(III) and europium(III) from nitric acid solutions by a novel diglycolamide-grafted silica-based resins: Part 2. Sorption isotherms, column and radiolytic stability studies. *Radiochimica Acta*, 102(10):903–910, January 2014.

[30] J.K Marsh, D. Sc., and F.R.I.C. The Separation of the Lanthanons (Rare-Earth Elements). *Quarterly Reviews of the Chemical Society*, 1(2):126–143, 1947.

[31] Simon Cotton. *Lanthanide and Actinide Chemistry*. 2006.

[32] J.A. Marinsky, L.E. Glendenin, and C.D. Coryell. The Chemical Identification of Radioisotopes of Neodymium and of Element 61. *Journal of the American Chemical Society*, 69(11):2781–2785, 1947.

[33] Aaron J. Rossini and Robert W. Schurko. Experimental and theoretical studies of 45Sc NMR interactions in solids. *Journal of the American Chemical Society*, 128(32):10391–402, August 2006.

[34] S. A. Cotton. The Co-Ordination Number of Sc 3+ (Aq). *Comments on Inorganic Chemistry*, 21(1-3):165–173, April 1999.

[35] Patric Lindqvist-Reis, Ingmar Persson, and Magnus Sandström. The hydration of the scandium(III) ion in aqueous solution and crystalline hydrates studied by XAFS spectroscopy, large-angle X-ray scattering and crystallography. *Dalton transactions (Cambridge, England : 2003)*, (32):3868–78, August 2006.

[36] Marina Katkova, Tatyana Balashova, Anatoly P Pushkarev, Igor Yu Ilyin, Georgy K. Fukin, Evgeny V. Baranov, Sergey Yu. Ketkov, and Mikhail N. Bochkarev. Anhydrous mono- and dinuclear tris(quinolinolate) complexes of scandium: the missing structures of rare earth metal 8-quinolinolates. *Dalton*, 40:7713–7717, 2011.

[37] Carina Merkens, Oliver Pecher, Friedrich Steuber, Sascha Eisenhut, Arno Görne, Frank Haarmann, and Ulli Englert. Crystal-to-Crystal Transformations in a Seven-Coordinated Scandium Complex. *Zeitschrift für anorganische und allgemeine Chemie*, 639(2):340–346, February 2013.

[38] Namjun Kim, Cheng-Han Hsieh, and Jonathan F. Stebbins. Scandium Coordination in Solid Oxides and Stabilized Zirconia: 45 Sc NMR. *Chemistry of Materials*, 18(16):3855–3859, August 2006.

[39] Jerzy Narbutt, Marian Czerwinski, and Jadwiga Krejzler. Seven-Coordinate d 0 and d 10 Ions-Computational and Experimental Studies on Tris (tropolonato)metal (III)-TOPO Adducts. *European Journal of Inorganic Chemistry*, pages 3187–3197, 2001.

[40] Mathew J. Willans, Kirk W. Feindel, Kristopher J. Ooms, and Roderick E. Wasylishen. An investigation of lanthanum coordination compounds by using solid-state 139La NMR spectroscopy and relativistic density functional theory. *Chemistry - A European Journal*, 12(1):159–168, 2006.

[41] Glenn T. Seaborg, Ralph A. James, and Albert Ghiorso. The New Element Curium (Atomic Number 96). Technical report, 1948.

[42] Glenn T. Seaborg, Ralph A. James, and Leon O. Morgan. The new element americium (atomic number 95). Technical report, 1948.

[43] Robert J. Silva, Giovanni Bidoglio, Malcolm H. Rand, Piotr B. Robouch, Hans Wanner, and Ignasi Puigdomenech. Chemical Thermodynamics of Americium. In *Chemical Thermodynamics*. 1995.

[44] Wolfgang H. Runde and Bruce J. Mincher. Higher oxidation states of americium: Preparation, characterization and use for separations. *Chemical Reviews*, 111(9):5723–5741, 2011.

[45] Thomas K. Keenan. First Observation of Aqueous Tetravalent Curium. *Journal of the American Chemical Society*, 83:3719–3720, 1961.

[46] Wolfgang H. Runde and Wallace W. Schulz. Americium. In *The Chemistry of the Actinide and Transactinide Elements*. 2006.

[47] Yin Jiang, Huatang Zhang, Qun He, Zheng Hu, and Xijun Chang. Selective solid-phase extraction of trace mercury(II) using a silica gel modified with diethylenetriamine and thiourea. *Microchimica Acta*, 178(3-4):421–428, 2012.

[48] Ronald E. Majors. High Speed Liquid Chromatography of Antioxidants and Plasticizers Using Solid Core Supports. *Journal of Chromatographic Science*, 8, 1970.

[49] David C. Locke. Chemically bonded stationary phases for liquid chromatography. *Journal of Chromatographic Science*, 11, 1973.

[50] J. Jernström, J. Lehto, and M. Betti. On-line separation of Pu(III) and Am(III) using extraction and ion chromatography. *Journal of Radioanalytical and Nuclear Chemistry*, 274(1):95–102, October 2008.

[51] Zhifeng Tu, Zheng Hu, Xijun Chang, Lijun Zhang, Qun He, Jianping Shi, and Ru Gao. Silica gel modified with 1-(2-aminoethyl)-3-phenylurea for selective solid-phase extraction and preconcentration of Sc(III) from environmental samples. *Talanta*, 80(3):1205–9, January 2010.

[52] O. B. Mokhodoeva, G. V. Myasoedova, and E. a. Zakharchenko. Solid-phase extractants for radionuclide preconcentration and separation. New possibilities. *Radiochemistry*, 53(1):35–43, 2011.

[53] Mathieu Etienne and Alain Walcarius. Analytical investigation of the chemical reactivity and stability of aminopropyl-grafted silica in aqueous medium. *Talanta*, 59:1173–88, May 2003.

[54] K.M. Feng, X., Fryxell, G.E., Wang, L.-Q., Kim, A.Y., Liu, J., Kemner. Functionalized Monolayers on Ordered Mesoporous Supports. *Science*, 276:923–926, May 1997.

[55] Jun Liu, Xiangdong Feng, Glen E. Fryxell, Li-Qiong Wang, Anthony Y. Kim, and Meiling Gong. Hybrid Mesoporous Materials with Functionalized Monolayers. *Advanced Materials*, 10(2):161–165, 1998.

[56] J.L Cortina, R Arad-Yellin, N Miralles, a.M Sastre, and a Warshawsky. Kinetics studies on heavy metal ions extraction by Amberlite XAD2 impregnated resins containing a bifunctional organophosphorous extractant. *Reactive and Functional Polymers*, 38(2-3):269–278, 1998.

[57] C. W. Huck and G. K. Bonn. Recent developments in polymer-based sorbents for solid-phase extraction. *Journal of Chromatography A*, 885:51–72, 2000.

[58] Colin F. Poole. New trends in solid-phase extraction. *Trends in Analytical Chemistry*, 22(6):362–373, 2003.

[59] J. S. Beck, J. C. Vartuli, W. J. Roth, M. E. Leonowicz, C. T. Kresge, K. D. Schmitt, C. T-W Chu, D. H. Olson, E.W. Sheppard, S.B. McCullen, J. B. Higgins, and J .L. Schlenker. A New Family of Mesoporous Molecular Sieves Prepared with Liquid Crystal Templates. *Journal of the American Chemical Society*, 114:10834–10843, 1992.

[60] C. T. Kresge, M. E. Leonowicz, W. J. Roth, J. C. Vartuli, and J. S. Beck. Ordered mesoporous molecular sieves synthesized by a liquid-crystal template mechanism. *Nature*, 359:710–712, 1992.

[61] G.D. Zhao, D., Feng, J., Huo, Q., Melosh, N., Fredrickson, G.H., Chmelka, B.F., Stucky. Triblock Copolymer Syntheses of Mesoporous Silica with Periodic 50 to 300 Angstrom Pores. *Science*, 279(5350):548–552, January 1998.

[62] Patrick Schmidt-Winkel, Wayne W. Lukens, Dongyuan Zhao, Peidong Yang, Bradley F. Chmelka, and Galen D. Stucky. Mesocellular Siliceous Foams with Uniformly Sized Cells and Windows. *Journal of the American Chemical Society*, 121:254–255, 1999.

[63] Patrick Schmidt-Winkel, Lukens Wayne W., Peidong Yang, David I. Margolese, John S. Lettow, Jackie Y. Ying, and Galen D. Stucky. Microemulsion Templating of Siliceous Mesostructured Cellular Foams with Well-Defined Ultralarge Mesopores. *Chemistry of Materials*, 12(3):686–696, 2000.

[64] Glen E. Fryxell, Shas V. Mattigod, Yuehe Lin, Hong Wu, Sandy Fiskum, Kent Parker, Feng Zheng, Wassana Yantasee, Tom S. Zemanian, R. Shane Addleman, Jun Liu, Ken Kemner, Shelly Kelly, and Xiangdong Feng. Design and synthesis of self-assembled monolayers on mesoporous supports (SAMMS): The importance of ligand posture in functional nanomaterials. *Journal of Materials Chemistry*, 17(28):2863–2874, 2007.

[65] Glen E. Fryxell, Yuehe Lin, Sandy Fiskum, Jerome C. Birnbaum, Hong Wu, Ken Kemner, and Shelley Kelly. Actinide Sequestration Using Self-Assembled Monolayers on Mesoporous Supports. *Environmental Science & Technology*, 39(5):1324–1331, March 2005.

[66] Glen E. Fryxell, Wilaiwan Chouyyok, and Ryan D. Rutledge. Design and synthesis of chelating diamide sorbents for the separation of lanthanides. *Inorganic Chemistry Communications*, 14(6):971–974, 2011.

[67] Joseph D. Davidson, Robert J. Wiacek, Sarah Burton, Xiaohong S. Li, Glen E. Fryxell, R. Shane Addleman, Wassana Yantasee, Thanapon Sangvanich, and Kanda Pattamakomsan. Improved deposition and deprotection of silane tethered 3,4 hydroxypyridinone (HOPO) ligands on functionalized nanoporous silica. *Inorganic Chemistry Communications*, 18(2012):92–96, 2012.

[68] Glen E. Fryxell, Wilaiwan Chouyyok, and Ryan D. Rutledge. Design and synthesis of chelating diamide sorbents for the separation of lanthanides. *Inorganic Chemistry Communications*, 14(6):971–974, 2011.

[69] Glen E. Fryxell and Jun Liu. Designing Surface Chemistry in Mesoporous Silica. In Eugene Papirer, editor, *Adsorption on Silica Surfaces*, pages 665–687. 2000.

[70] Thomas S Zemanian, Glen E Fryxell, Jun Liu, Shas Mattigod, James A Franz, and Zimin Nie. Deposition of Self-Assembled Monolayers in Mesoporous Silica from Supercritical Fluids. *Langmuir*, 17:8172–8177, 2001.

[71] John C. Linehan, Cory M. Stiff, and Glen E. Fryxell. A simple determination of alkylsilane monolayer population density. *Inorganic Chemistry Communications*, 9(2):239–241, February 2006.

[72] Wassana Yantasee, Yuehe Lin, GlenE. Fryxell, and Zheming Wang. Carbon Paste Electrode Modified with Carbamoylphosphonic Acid Functionalized Mesoporous Silica: A New Mercury-Free Sensor for Uranium Detection. *Electroanalysis*, 16(10):870–873, May 2004.

[73] Yung-Jin Hu. *Reaction of Plutonium(VI) with the Manganese-Substituted Iron Oxide Mineral Goethite*. PhD thesis, 2011.

[74] R. A. Penneman and T. K. Keenan. The Radiochemistry of Americium and Curium. In *Nuclear Science Series*. National Academy of Sciences- National Research Council, 1960.

[75] Sherrod L. Maxwell, Brian K. Culligan, and Gary W. Noyes. Rapid separation method for actinides in emergency soil samples. *Radiochimica Acta*, 98(12):793–800, December 2010.

[76] Amit Katiyar, Santosh Yadav, Panagiotis G. Smirniotis, and Neville G. Pinto. Synthesis of ordered large pore SBA-15 spherical particles for adsorption of biomolecules. *Journal of Chromatography A*, 1122(1):13–20, 2006.

[77] Nando Gartmann, Christina Schütze, Hanna Ritter, and Dominik Brühwiler. The effect of water on the functionalization of mesoporous silica with 3-aminopropyltriethoxysilane. *Journal of Physical Chemistry Letters*, 1(1):379–382, 2010.

[78] Serban C. Moldoveanu and Victor David. *Essentials in Modern HPLC Separations*. Elsevier Inc., 2013.

[79] Glen E. Fryxell, Hong Wu, Yuehe Lin, Wendy J. Shaw, Jerome C. Birnbaum, John C. Linehan, Zimin Nie, Ken Kemner, and Shelly Kelly. Lanthanide selective sorbents: self-assembled monolayers on mesoporous supports (SAMMS). *Journal of Materials Chemistry*, 14(22):3356–3363, November 2004.

[80] Steffen Onclin, Bart Jan Ravoo, and David N. Reinhoudt. Engineering silicon oxide surfaces using self-assembled monolayers. *Angewandte Chemie - International Edition*, 44(39):6282–6304, 2005.

[81] Peter J. Goodhew, John Humphreys, and Richard Beanland. *Electron Microscopy and Analysis*. CRC Press, third edit edition, 2000.

[82] Douglas A. Skoog, F. James Holler, and R. Crouch, Stanley. *Principles of Instrumental Analysis; 6th Edition*. 2007.

[83] Stephen Brunauer, P. H. Emmett, and Edward Teller. Adsorption of Gases in Multimolecular Layers. *Journal of the American Chemical Society*, 60:309–319, 1938.

[84] J. H de Boer. The BET Method. In D. H. Everett and R. H. Ottewill, editors, *Surface Area Determination*. International Union of Pure and Applied Chemistry, 1969.

[85] Elliott P. Barrett, Leslie G. Joyner, and Paul P. Halenda. The Determination of Pore Volume and Area Distributions in Porous Substances. I. Computations from Nitrogen Isotherms. *Journal of the American Chemical Society*, 73:373–380, 1951.

[86] Johan C. Groen, Louk a a Peffer, and Javier Pérez-Ramírez. Pore size determination in modified micro- and mesoporous materials. Pitfalls and limitations in gas adsorption data analysis. *Microporous and Mesoporous Materials*, 60:1–17, 2003.

[87] H. Levitt, Malcolm. *Spin Dynamics: Basics of Nuclear Magnetic Resonance*. Wiley-Interscience, second edi edition, 2008.

[88] Melinda J. Duer. *Introduction to Solid-State NMR Spectroscopy*. Wiley-Blackwell, 2005.

[89] K.J.D. MacKenzie and M.E. Smith. *Multinuclear Solid-State NMR of Inorganic Materials*. Pergamon, New York, 2002.

[90] E.R. Andrew, a. Bradbury, and R.G. Eades. Nuclear magnetic resonance spectra from a crystal rotated at high speed, 1958.

[91] I. J. Lowe. Free induction decays of rotating solids. *Physical Review Letters*, 2(7):285–287, 1959.

[92] M. Matti Maricq and J. S. Waugh. NMR in rotating solids. *The Journal of Chemical Physics*, 70(7):3300–3316, 1979.

[93] Ségolène Laage, Joseph R. Sachleben, Stefan Steuernagel, Roberta Pierattelli, Guido Pintacuda, and Lyndon Emsley. Fast acquisition of multi-dimensional spectra in solid-state NMR enabled by ultra-fast MAS. *Journal of Magnetic Resonance*, 196(2):133–141, 2009.

[94] S. Hafner and H. W. Spiess. Advanced solid-state NMR spectroscopy of strongly dipolar coupled spins under fast magic angle spinning. *Concepts in Magnetic Resonance*, 10(1):99–128, 1998.

[95] Claudiu Filip, Siegfried Hafner, Ingo Schnell, Dan E Demco, and Hans W Spiess. Solid-state nuclear magnetic resonance spectra of dipolar-coupled multi-spin systems under fast magic angle spinning. *Chemical Physics*, 110(1):423–440, 1999.

[96] A. Pines, M. H. Gibby, and J. S. Waugh. Proton-Enhanced Nuclear Induction Spectroscopy. A Method for High-Resolution NMR of Dilute Spins in Solids. *J. Chem. Phys.*, 56(4):1776–1777, 1973.

[97] Waclaw Kolodziejski and Jacek Klinowski. Kinetics of cross-polarization in solid-state NMR: A guide for chemists. *Chemical Reviews*, 102(3):613–628, 2002.

[98] Hans Wolfgang Spiess. Spectroscopy of Dipolar Coupled Spins Under Fast Magic Angle Spinning. *eMagRes*, 1:109–126, 2012.

[99] W. Sommer, J. Gottwald, D.E. Demco, and H.W. Spiess. Dipolar Heteronuclear Multiple-Quantum NMR Spectroscopy in Rotating Solids. *Journal of Magnetic Resonance*, 113:131–134, 1995.

[100] D. E. Demco, S. Hafner, and H. W. Spiess. Rotation-Synchronized Homonuclear Dipolar Decoupling. *Journal of Magnetic Resonance, Series A*, 116:36–45, 1995.

[101] Gary Drobny, Alexander Pines, Steven Sinton, Daniel P. Weitekamp, and David Wemmer. Fourier Transform Multiple Quantum Nuclear Magnetic Resonance. *Faraday Symposia of the Chemical Society*, 13:49–55, 1978.

[102] Clare P. Grey, Astrid P. A. M. Eijkelenboom, and Wiebren S. Veeman. 14N population transfers in two-dimensional 13C-14N-1H triple-resonance magic-angle spinning nuclear magnetic resonance spectroscopy. *Solid state nuclear magnetic resonance*, 4(2):113–120, 1995.

[103] Clare P. Grey and Alexander J. Vega. Determination of the Quadrupole Coupling-Constant of the Invisible Aluminum Spins in Zeolite Hy With H-1/Al-27 Trapdor NMR. *Journal of the American Chemical Society*, 117(31):8232–8242, 1995.

[104] Glenn F. Knoll. *Radiation Detection and Measurement*. Wiley, fourth edi edition, 2010.

[105] Laina Salonen. Measurement of low levels of 222Rn in water with different commercial liquid scintillation counters and pulse-shape analysis. In *Liquid Scintillation Spectrometry*, pages 361–372. 1992.

[106] Norbert Roessler, Robert J Valenta, and Stat van Cauter. Time-Resolved Liquid Scintillation Counting. In *Liquid Scintillation Counting and Organic Scintillators*, pages 501–511. Lewis Publishers, Inc, 1991.

[107] Ivan K. Kressin. Electrodeposition of plutonium and americium for high resolution alpha spectrometry. *Analytical Chemistry*, 49(6):842–846, 1977.

[108] Junko Yano and Vittal K. Yachandra. X-ray absorption spectroscopy. *Photosynthesis Research*, 102(2):241–254, 2009.

[109] P. A. Lee, P. H. Citrin, P. Eisenberger, and B. M. Kincaid. Extended x-ray absorption fine structure - ˜ citations as a structural tool. *Reviews of Modern Physics*, 53(4):769–806, 1981.

[110] Sam M. Webb. SIXPACK: Sam's Interface for XAS Package, 2014.

[111] Bruce Ravel and M Newville. ATHENA, ARTEMIS, HEPHAESTUS data analysis for X-ray absorption spectroscopy using IFEFFIT. *Journal of Synchrotron Radiation*, 12:537–541, 2005.

[112] J. J. Rehr, J. J. Kas, F. D. Vila, M. P. Prange, and K. Jorissen. Parameter-free calculations of x-ray spectra with FEFF9. *Physical Chemistry Chemical Physics*, 12:5503–5513, 2010.

[113] J. J. Rehr, J. J. Kas, M. P. Prange, A. P. Sorini, Y. Takimoto, and F. D. Vila. Ab initio theory and calculations of X-ray spectra. *Comptes Rendus Physique*, 10(6):548–559, 2009.

[114] J. J. Rehr and R. C. Albers. Theoretical approaches to X-ray absorption fine structure. *Reviews of Modern Physics*, 72:621, 2000.

[115] Sam M. Webb. SMAK: Sam's Microprobe Analysis Kit, 2014.

[116] Joseph R. Lakowicz. *Principles of Fluorescence Spectroscopy.* Kluwer Academic/ Plenum Publishers, second edi edition, 1999.

[117] William DeW. Horrocks Jr. and Daniel R. Sudnick. Lanthanide ion probes of structure in biology. Laser-induced luminescence decay constants provide a direct measure of the number of metal-coordinated water molecules. *Journal of the American Chemical Society*, 101(2):334–340, January 1979.

[118] Yuehe Lin, Sandra K Fiskum, Wassana Yantasee, Hong Wu, Shas V Mattigod, Erich Vorpagel, Glen E Fryxell, Kenneth N Raymond, and Jide Xu. Incorporation of hydroxypyridinone ligands into self-assembled monolayers on mesoporous supports for selective actinide sequestration. *Environmental science & technology*, 39(5):1332–7, March 2005.

[119] Timothy G. Carter, Wassana Yantasee, Thanapon Sangvanich, Glen E. Fryxell, Darren W. Johnson, and R. Shane Addleman. New functional materials for heavy metal sorption: "supramolecular" attachment of thiols to mesoporous silica substrates. *Chemical communications (Cambridge, England)*, (43):5583–5, November 2008.

[120] Robert I. Nooney, Mohan Kalyanaraman, Gordon Kennedy, and Edward J. Maginn. Heavy Metal Remediation Using Functionalized Mesoporous Silicas with Controlled Macrostructure. *Langmuir*, 17(2):528–533, January 2001.

[121] Harris E. Mason, Paolo Montagna, Laura Kubista, Marco Taviani, Malcolm McCulloch, and Brian L. Phillips. Phosphate defects and apatite inclusions in coral skeletal aragonite revealed by solid-state NMR spectroscopy. *Geochimica et Cosmochimica Acta*, 75(23):7446–7457, December 2011.

[122] J.R. Houston, J.L. Herberg, R.S. Maxwell, and S.A. Carroll. Association of dissolved aluminum with silica: Connecting molecular structure to surface reactivity using NMR. *Geochimica et Cosmochimica Acta*, 72(14):3326–3337, 2008.

[123] S. Sen and J. F. Stebbins. Structural role of Nd 3+ and A13+ cations in SiO2 glass : a 29Si MAS-NMR spin-lattice relaxation, 27Al NMR and EPR study. *Journal of Non-Crystalline Solids*, 188:54–62, 1995.

[124] Dieter Rehder and Kirsten Hink. The interaction of Sc(OH)2+aq with serine and small peptides investigated by 45Sc NMR spectroscopy. *Inorganica Chimica Acta*, 158(2):265–271, April 1989.

[125] Jovita Moreno, Jose Iglesias, Juan A. Melero, and David C. Sherrington. Synthesis and characterisation of (hydroxypropyl)-2-aminomethyl pyridine containing hybrid polymersilica SBA-15 materials supporting Mo(vi) centres and their use as heterogeneous catalysts for oct-1-ene epoxidation. *Journal of Materials Chemistry*, 21(18):6725, April 2011.

[126] Susmita Bhunia and Subratanath Koner. Functionalization of oxo-vanadium(IV) acetylacetonate over modified MCM-41: an efficient reusable catalyst for epoxidation reaction. *Journal of Porous Materials*, 18(4):399–407, May 2010.

[127] Muhammad Usman Azmat, Yong Guo, Yun Guo, Yanqin Wang, and Guanzhong Lu. An easy and effective approach towards heterogeneous Pt/SiO2-cinchonidine catalyst system for enantioselective hydrogenation of ethyl pyruvate. *Journal of Molecular Catalysis A: Chemical*, 336(1):42–50, 2011.

[128] Satoka Tanaka, Mizuki Tada, and Yasuhiro Iwasawa. Enantioselectivity promotion by achiral surface functionalization on SiO2-supported Cu-bis(oxazoline) catalysts for asymmetric DielsAlder reactions. *Journal of Catalysis*, 245(1):173–183, 2007.

[129] Jennifer L. Rapp, Yulin Huang, Michael Natella, Yang Cai, Victor S.-Y. Lin, and Marek Pruski. A solid-state NMR investigation of the structure of mesoporous silica nanoparticle supported rhodium catalysts. *Solid State Nuclear Magnetic Resonance*, 35(2):82–86, 2009.

[130] Anna Grünberg, Xu Yeping, Hergen Breitzke, and Gerd Buntkowsky. Solid-state NMR characterization of Wilkinson's catalyst immobilized in mesoporous SBA-3 silica. *Chemistry (Weinheim an der Bergstrasse, Germany)*, 16(23):6993–8, June 2010.

[131] Jennifer A. Shusterman, Harris E. Mason, Anthony Bruchet, Mavrik Zavarin, Annie B. Kersting, and Heino Nitsche. Analysis of Trivalent Cation Complexation to Functionalized Mesoporous Silica using Solid-State NMR Spectroscopy. *Dalton Transactions*, 43(44):16649–58, October 2014.

[132] Philippe Trens, Mark L Russell, Lena Spjuth, Michael J Hudson, and Jan-Olov Liljenzin. Preparation of Malonamide-MCM-41 Materials for the Heterogeneous Extraction of Radionuclides. *Ind. Eng. Chem. Res.*, 41:5220–5225, 2002.

[133] Yuji Sasaki, Yumi Sugo, Shinichi Suzuki, and Takaumi Kimura. A method for the determination of extraction capacity and its application to N,N,N,N-tetraalkylderivatives of diglycolamide-monoamide/n-dodecane media. *Analytica Chimica Acta*, 543(1-2):31–37, July 2005.

[134] Debasis Das, S. A. Ansari, P. K. Mohapatra, G. Mary, K. Radhakrishnan, S. C. Tripathi, and V. K. Manchnada. Separation and Determination of Components of High Level Waste using IC and Dynamically Modified Reversed-Phase HPLC in Actinide Partitioning Studies using Synthetic Waste Solution. *Journal of Radioanalytical and Nuclear Chemistry*, 287:293–298, July 2011.

[135] Marta Maria Reinoso Garcia. *Chelating Agents for Actinide/Lanthanide Separation.* PhD thesis, Universiteit Twente, 2004.

[136] Benoît Gannaz, Mark R Antonio, Renato Chiarizia, Clément Hill, and Gérard Cote. Structural study of trivalent lanthanide and actinide complexes formed upon solvent extraction. *Dalton transactions (Cambridge, England : 2003)*, (38):4553–62, October 2006.

[137] A. Sengupta, S. K. Thulasidas, V. C. Adya, P. K. Mohapatra, S. V. Godbole, and V. K. Manchanda. Purification of americium from assorted analytical waste in hydrochloric acid medium. *Journal of Radioanalytical and Nuclear Chemistry*, 292(3):1017–1023, November 2011.

[138] Jean-charles Broudic, Olivier Conocar, J J E Moreau, Daniel Meyer, and Michel Wong Chi Man. New hybrid silica based materials for the solid-liquid extraction of actinides. pages 2283–2285, 1999.

[139] R. D. Shannon. Revised Effective Ionic Radii and Systematic Studies of Interatomic Distances in Halides and Chaleogenides. *Acta Crystallography*, A32:751–767, 1976.

[140] Nicolas Bibent, Thibault Charpentier, Sabine Devautour-Vinot, Ahmad Mehdi, Philippe Gaveau, François Henn, and Gilles Silly. Solid-State NMR Spectroscopic Studies of Propylphosphonic Acid Functionalized SBA-15 Mesoporous Silica: Characterization of Hydrogen-Bonding Interactions. *European Journal of Inorganic Chemistry*, 2013(13):2350–2361, May 2013.

[141] Gabriel Y. S. Chan, Michael G. B. Drew, Michael J. Hudson, Peter B. Iveson, Jan-Olov Liljenzin, Mats Skå lberg, Lena Spjuth, and Charles Madic. Solvent extraction of metal ions from nitric acid solution using N, N'-substituted malonamides. Experimental and crystallographic evidence for two mechanisms of extraction, metal complexation and ion-pair formation. *Journal of the Chemical Society, Dalton Transactions*, (4):649–660, 1997.

[142] Gregg J. Lumetta, Brian M. Rapko, Priscilla a. Garza, Benjamin P. Hay, Robert D. Gilbertson, Timothy J. R. Weakley, and James E. Hutchison. Deliberate design of ligand architecture yields dramatic enhancement of metal ion affinity. *Journal of the American Chemical Society*, 124(20):5644–5645, 2002.

[143] E. A. Mowafy and H. F. Aly. Extraction Behaviors of Trivalent Lanthanides from Nitrate Medium by Selected Substituted Malonamides. *Solvent Extraction and Ion Exchange*, 24(5):677–692, 2006.

[144] Bruce K. McNamara, Gregg J. Lumetta, and Brian M. Rapko. Extraction of Europium(Iii) Ion With Tetrahexylmalonamides. *Solvent Extraction and Ion Exchange*, 17(6):1403–1421, 1999.

[145] J. D. Kubicki, D. Sykes, and S. E. Apitz. Ab Initio Calculation of Aqueous Aluminum and AluminumCarboxylate Complex Energetics and 27 Al NMR Chemical Shifts. *The Journal of Physical Chemistry A*, 103(7):903–915, February 1999.

[146] Pragati Jain, Hugo J. Avila-Paredes, Christine Gapuz, Sabyasachi Sen, and Sangtae Kim. High-Resolution 89 Y and 45 Sc NMR Spectroscopic Study of Short-Range Structural Order in Nanocrystalline Y- and Sc-doped CeO 2 and ZrO 2. *The Journal of Physical Chemistry C*, 113(16):6553–6560, April 2009.

[147] Changhua C. Liu and Gary E. Maciel. The Fumed Silica Surface : A Study by NMR. 118:5103–5119, 1996.

[148] Julien Trébosc, Jerzy W Wiench, Seong Huh, Victor S.-Y. Lin, and Marek Pruski. Solid-state NMR study of MCM-41-type mesoporous silica nanoparticles. *Journal of the American Chemical Society*, 127(9):3057–68, March 2005.

[149] Shane Pawsey, Mark McCormick, Susan De Paul, Robert Graf, Y S Lee, Linda Reven, and Hans W Spiess. 1H fast MAS NMR studies of hydrogen-bonding interactions in self-assembled monolayers. *Journal of the American Chemical Society*, 125:4174–84, April 2003.

[150] Scott A. Wood and Iain M. Samson. The Aqueous Geochemistry of Gallium, Germanium, Indium, and Scandium. *Ore Geology Reviews*, 28:57–102, 2006.

[151] Wen Zhang, Xihong He, Gang Ye, Rong Yi, and Jing Chen. Americium(III) Capture Using Phosphonic Acid-Functionalized Silicas with Different Mesoporous Morphologies: Adsorption Behavior Study and Mechanism Investigation by EXAFS/XPS. *Environmental science & technology*, 48:6874–6881, 2014.

[152] Li Yong Yuan, Zhi Qiang Bai, Ran Zhao, Ya Lan Liu, Zi Jie Li, Sheng Qi Chu, Li Rong Zheng, Jing Zhang, Yu Liang Zhao, Zhi Fang Chai, and Wei Qun Shi. Introduction of bifunctional groups into mesoporous silica for enhancing uptake of thorium(IV) from aqueous solution. *ACS Applied Materials and Interfaces*, 6(7):4786–4796, 2014.

[153] Ilya A. Shkrob, Angela R. Tisch, Timothy W. Marin, John V. Muntean, Michael D. Kaminski, and A. Jeremy Kropf. Surface modified, collapsible controlled pore glass materials for sequestration and immobilization of trivalent metal ions. *Industrial and Engineering Chemistry Research*, 50(8):4686–4696, 2011.

[154] A.S. Suneesh, K.V. Syamala, K.A. Venkatesan, M.P. Antony, and P.R. Vasudeva Rao. Diglycolamic acid modified silica gel for the separation of hazardous trivalent metal ions from aqueous solution. *Journal of Colloid and Interface Science*, 438(2015):55–60, 2015.

[155] Gregg Lumetta, Brian Rapko, Benjamin Hay, Priscilla Garza, Robert Gilbertson, and James Hutchison. A Novel Bicyclic Diamide with High Binding Affinity for Trivalent fBlock Elements. *Solvent Extraction and Ion Exchange*, 21(1):29–39, January 2003.

[156] L. Spjuth, J. O. Liljenzin, M. J. Hudson, M. G B Drew, P. B. Iveson, and C. Madic. Comparison of extraction behaviour and basicity of some substituted malonamides. *Solvent Extraction and Ion Exchange*, 18(1):1–23, 2000.

[157] S. Sasaki, Y., Tachimori. Extraction of Actinides(III), (IV), (V), (VI), and Lanthanides(III) by Structurally Tailored Diamides. *Solvent Extraction and Ion Exchange*, 20(1):21–34, 2002.

[158] By H Suzuki, Y Sasaki, Y Sugo, A Apichaibukol, and T Kimura. Extraction and separation of Am (III) and Sr (II) by N , N , N , N -tetraoctyl-3-oxapentanediamide (TODGA). *Radiochimica Acta*, 92:463–466, 2004.

[159] Yuji Sasaki, Yumi Sugo, Shinichi Suzuki, and Shoichi Tachimori. The Novel Extractants, Diglycolamides, for the Extraction of Lanthanides and Actinides in HNO3-n-Dodecane System. *Solvent Extraction and Ion Exchange*, 19(1):91–103, 2001.

[160] Takaumi Kimura and Gregory R. Choppin. Luminescence study on determination of the hydration number of Cm(III). *Journal of Alloys and Compounds*, 213-214:313–317, October 1994.

[161] Artem V. Gelis and Gregg J. Lumetta. Actinide Lanthanide Separation ProcessALSEP. *Industrial & Engineering Chemistry Research*, 53(4):1624–1631, January 2014.

[162] Mark P. Jensen, Tsuyoshi Yaita, and Renato Chiarizia. Reverse-micelle formation in the partitioning of trivalent F-element cations by biphasic systems containing a tetraalkyldiglycolamide. *Langmuir : the ACS journal of surfaces and colloids*, 23(9):4765–74, April 2007.

[163] T. Yaita, A. W. Herlinger, P. Thiyagarajan, and M. P. Jensen. Influence of Extractant Aggregation on the Extraction of Trivalent f-Element Cations by a Tetraalkyldiglycolamide. *Solvent Extraction and Ion Exchange*, 22(4):553–571, December 2004.

[164] Vivek Chavan, Vasudevan Thekkethil, Ashok K Pandey, Mudassir Iqbal, Jurriaan Huskens, Sher Singh, Asok Goswami, and Willem Verboom. Assembled diglycolamide for f-element ions sequestration at high acidity. *Reactive and Functional Polymers*, 74:52–57, 2014.

[165] Vivek Chavan, Sabyasachi Patra, Ashok K. Pandey, Vasudevan Thekkethil, Mudassir Iqbal, Jurriaan Huskens, Debasis Sen, S. Mazumder, Asok Goswami, and Willem Verboom. Understanding Nitric Acid-Induced Changes in the Arrangement of Monomeric and Polymeric Methacryloyl Diglycolamides on Their Affinity toward f-Element Ions. *The Journal of Physical Chemistry B*, 119(1):212–218, 2015.

[166] S a Ansari, P N Pathak, M Husain, a K Prasad, V S Parmar, and V K Manchanda. Extraction chromatographic studies of metal ions using N,N,N',N'-tetraoctyl diglycolamide as the stationary phase. *Talanta*, 68(4):1273–80, February 2006.

[167] Narek Gharibyan, Ashlee Dailey, Derek R. McLain, Evelyn M. Bond, Walter a. Moody, Steffen Happel, and Ralf Sudowe. Extraction Behavior of Americium and Curium on Selected Extraction Chromatography Resins from Pure Acidic Matrices. *Solvent Extraction and Ion Exchange*, 32(4):391–407, May 2014.

[168] Dean W. Sindorf and Gary E. Maciel. 29Si CP/MAS NMR studies of methylchlorosilane reactions on silica gel. *Journal of the American Chemical Society*, 103(14):4263–4265, 1981.

[169] Narek Gharibyan. *Intragroup separation of trivalent lanthanides and actinides for neutron capture experiments in stockpile stewardship sciences.* PhD thesis, University of Nevada, Las Vegas, 2011.

[170] Yu-Liang Zhang, Wei-Sheng Liu, Wei Dou, and Wen-Wu Qin. Synthesis and infrared and fluorescence spectra of new europium and terbium polynuclear complexes with an amide-based 1,10-phenanthroline derivative. *Spectrochimica acta. Part A*, 60(8-9):1707–11, July 2004.

[171] Tomoji Ohishi. Preparation and Properties of SiO2 Thin Films by the Sol-Gel Method Using Photoirradiation and Its Application to Surface Coating for Display. In *Chemical Processing of Ceramics*, pages 425–428. 2005.

[172] Shanrong Zhang, Patrick Winter, Kuangcong Wu, and A. Dean Sherry. A Novel Europium(III)-Based MRI Contrast Agent. *Journal of the American Chemical Society*, 123:1517–1518, 2001.

[173] S. Ganapathy, V. P. Chacko, R. G. Bryant, and M. C. Etter. Carbon CP-MASS NMR and X-ray crystal structure of paramagnetic lanthanide acetates. *Journal of the American Chemical Society*, 108(12):3159–3165, 1986.

[174] Linfeng Rao, PierLuigi Zanonato, Plinio Di Bernardo, and Arturo Bismondo. Calorimetric and spectroscopic studies of Eu(III) complexation with tetramethylmalonamide and tetramethylsuccinamide in acetonitrile and dimethylsulfoxide. *Inorganica Chimica Acta*, 306(1):49–64, 2000.

[175] Silvia Stumpf, Isabelle Billard, Petra J Panak, and Soufiane Mekki. Differences of Eu(III) and Cm(III) chemistry in ionic liquids: investigations by TRLFS. *Dalton transactions (Cambridge, England : 2003)*, 1(2):240–8, January 2007.

[176] P. N. Pathak, S. A. Ansari, S. V. Godbole, A. R. Dhobale, and V. K. Manchanda. Interaction of Eu3+ with N,N,N',N'-tetraoctyl diglycolamide: a time resolved luminescence spectroscopy study. *Spectrochimica acta. Part A, Molecular and biomolecular spectroscopy*, 73(2):348–52, July 2009.

[177] Makoto Arisaka and Takaumi Kimura. Thermodynamic and Spectroscopic Studies on Am (III) and Eu (III) in the Extraction System of N , N , N ', N ' - Diamide in n-Dodecane / Nitric Acid. *Society*, 29(May 2012):72–85, 2011.

[178] R. C. Ewing, W. J. Weber, and F. W. Clinard, Jr. Radiation effects in nuclear waste forms for high-level radioactive waste. *Progress in Nuclear Energy*, 29(2):63–127, 1995.

[179] Mark R. Antonio, Daniel R. McAlister, and E. Philip Horwitz. An europium(iii) diglycolamide complex: insights into the coordination chemistry of lanthanides in solvent extraction. *Dalton transactions (Cambridge, England : 2003)*, 44:515–521, October 2015.

[180] Rohm and Haas. AMBERCHROM Chromatographic Resins. Technical report, 2005.

[181] Tashi Parsons-Moss. *Interactions of Plutonium and Lanthanides with Ordered Mesoporous Materials*. PhD thesis, Department of Chemistry, University of California, Berkeley, 2014.

[182] Giuseppe Modolo and Sherif Nabet. Thermodynamic Study on the Synergistic Mixture of Bis (chlorophenyl) dithiophosphinic Acid and Tris (2- ethylhexyl) phosphate for Separation of Actinides (III) from Lanthanides (III). *Solvent Extraction and Ion Exchange*, 23:359–373, 2005.

[183] Tashi Parsons-Moss, Jinxiu Wang, Stephen Jones, Erin May, Daniel Olive, Zurong Dai, Mavrik Zavarin, Annie B. Kersting, Dongyuan Zhao, and Heino Nitsche. Sorption interactions of plutonium and europium with ordered mesoporous carbon. *Journal of Materials Chemistry A*, 2:11209, 2014.

[184] Ashish Kumar Singha Deb, P. Ilaiyaraja, D. Ponraju, and B. Venkatraman. Diglycolamide functionalized multi-walled carbon nanotubes for removal of uranium from aqueous solution by adsorption. *Journal of Radioanalytical and Nuclear Chemistry*, 291(3):877–883, August 2011.